University of California
Los Angeles

Measurement of Transverse Single Spin Asymmetries for π^0 and Jets at Large x_F in $\sqrt{s} = 500$ GeV Polarized Proton Collisions at STAR

A dissertation submitted in partial satisfaction
of the requirements for the degree
Doctor of Philosophy in Physics

by

Yuxi Pan

2015

Abstract of the Dissertation

Measurement of Transverse Single Spin Asymmetries for π^0 and Jets at Large x_F in $\sqrt{s} = 500$ GeV Polarized Proton Collisions at STAR

by

Yuxi Pan

Doctor of Philosophy in Physics

University of California, Los Angeles, 2015

Professor Huan Z. Huang, Chair

Asymmetries in the production of final state particles from collider or fixed-target experiments with polarized beams or target could provide valuable information on the spin structure of the nucleon. Transverse and longitudinal spin asymmetry measurements are complementary approaches for probing the nucleon spin structure functions and understanding the QCD dynamics for such phenomena, due to the non-commutative nature of boosts and rotations in relativistic regime.

The research presented in this thesis focuses on characterizing the Transverse Single Spin Asymmetries (TSSA) of inclusive π^0 and jet productions in polarized proton collisions at large Feynman-x (x_F) region. Theoretically these observables are explained by means of collinear twist-3 multi-parton correlations. In this picture the asymmetries originate from initial-state twist-3 parton distributions in the polarized proton and/or through the coupling between proton's initial-state transversity distribution and the final-state twist-3 fragmentation functions. The measurement of SSA for forward inclusive π^0 produced in pp collisions up to high transverse momentum helps examine the validity and interplay of these initial- and final-state models. These models can be further explored by investigating the dependence of the TSSA on event topologies. This thesis presents the STAR measurement of TSSA for forward inclusive π^0 at $2.8 < \eta < 4.0$ in $\sqrt{s} = 500$ GeV pp collisions taken in

2011 with integrated luminosity of 22 pb^{-1} as well as the dependence of π^0 TSSA on event topologies. In addition we show results of the analyses of Sivers and Collins asymmetries for forward jet-like events. The physics implications of these measurements will also be discussed.

The dissertation of Yuxi Pan is approved.

An Yin

George Igo

Graciela Gelmini

Huan Z. Huang, Committee Chair

University of California, Los Angeles

2015

To my parents

Table of Contents

List of Figures

List of Tables

Acknowledgments

First of all I would like to thank my parents for their unconditional support through out the years I have been away from home, for their encouragement for me to do the things I like and for their patience in cultivating my interest in science when I was little. My mother, who teaches physics labs in college, used to bring me to her class when I was a kid. I still remember me messing around with an old oscilloscope excitedly, and thought I was controlling a radar detector.

I would like to thank my advisor Prof. Huanzhong Huang for his scientific insights and open-mindedness. He is the reason my past six years at UCLA has been such a fruitful and enjoyable experience. My gratitude also goes to Prof. Charles Whitten who had been extremely supportive in helping me settle down and start my research when I just joined the group. His sudden departure was a great loss to us. Prof. George Igo has offered me a lot of opportunities from research-related discussions to being a teaching assistant for his nuclear physics class.

This thesis would have absolutely been not possible without Dr. Stephen Trentalange, who brought me onboard to the great adventures of operating the detectors, analyzing the online data and even my first visit to the New York City. Those sleepless nights I spent with Stephen working in the STAR control room will be my invaluable memories. Stephen has been a great source of ideas and a great mentor guiding me through the difficulties in my research.

I would like to thank many STAR collaborators who have generously helped me in various stages of the physics analysis. Prof. Steven Heppelmann has pioneered both the experimental and theoretical studies of the transverse spin effects. I thank him for his patience in getting me started with the software related to the data analysis and simulations, for offering his valuable insights to the ins and outs of transverse spin phenomena and for his hospitality during my visit to Penn State University. I thank Prof. Carl Gagliardi who has helped me in almost every details in my analysis work. My gratitude also goes to Elke-Caroline Aschenauer, Renee Fatemi, Jim Drachenberg, Anselm Vossen, Ernst Sichtermann, Akio

Ogawa, Mriganka Mondal and Chris Dilks, and to Dr. Zhongbo Kang who has taught me lot on the theories behind my analysis. I'd like to thank many of my Chinese fellow friends at Brookhaven National Lab for inviting me to dinners and Sunday grocery shoppings, especially when food was so hard to come by if one stays onsite for months without a car.

Within our local group at UCLA I'd like to thank Oleg Tsai, Gang Wang, Wenqin Xu, Jay Dunkelberger, Keith Landry, Jingguo Ma, Neha Shah, Xiaohua Liu, Feng Zhao, Brian Zhu, Liwen Wen, Roli Esha and Md. Nasim, with whom I have enjoyed so much about daily research and studies, as well as a little bit of the California sunshine.

Vita

2009	B.Sc. Physics, University of Science & Technology of China.
2009-2011	Teaching Assistant Department of Physics and Astronomy, UCLA.
2011-2015	Graduate Student Researcher Department of Physics and Astronomy, UCLA.

CHAPTER 1

Introduction

1.1 Overview

Science is based on the fact that the Nature is governed by fundamental principles, that concise theories can be built upon these principles and can be falsified by observation. Scientists rely on carefully designed experiments to observe, understand and describe the world so that knowledges can be passed on to the next generation. This thesis work is about the experiment to further our understanding of the fundamental building blocks of matter –quarks and gluons, and how they come together to form one of the simplest composite systems –the proton.

The knowledge we have accumulated so far on the basic constituents of matter and the interactions between them can be summarized by the Standard Model, which states that quarks and leptons are the fundamental ingredients of matter and their interactions are mediated by gauge bosons. There exists four types of fundamental interactions, categorized by their respective force carriers and strength: gravity, electromagnetic force, weak interactions and strong interactions. To date with the exception of gravity all the other three interactions can be described by quantum field theory built upon different representations, e.g. electromagnetic interaction is initially described by Quantum Electrodynamics (QED) with U(1) group and later it was discovered that a unified theory of electromagnetism and the weak interaction can be formulated at a higher energy scale with a different representation SU(2), called electroweak theory. On the other hand strong interaction is described by Quantum Chromodynamics (QCD) with SU(3) group. The strong interaction is responsible for binding quarks together via the exchange of gluons and making the dominant contribution to the

mass of baryonic matter.

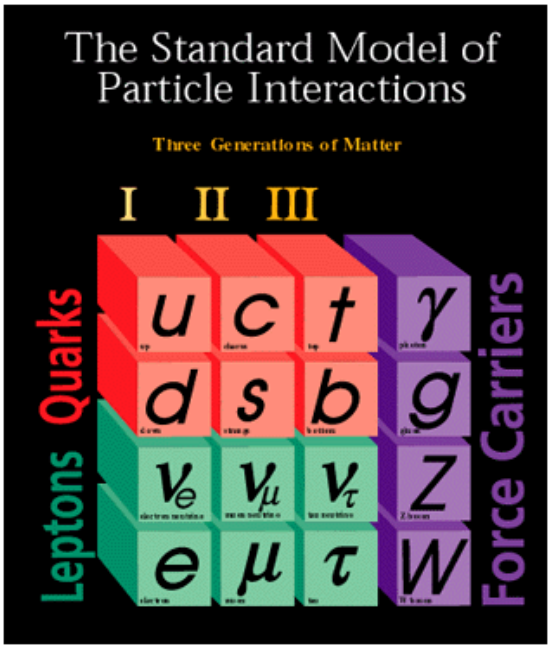

Figure 1.1: The Standard Model

1.2 Quantum Chromodynamics and its experimental implication

Quantum Chromodynamics (QCD) is the theory of strong interaction. Similar to QED, quarks carry 'color' charges in QCD theory and the interactions between quarks are mediated by a gauge boson called gluon. However contrary to the properties of photon, the force carrier in QED, gluons take on different color charges as well and can interact among themselves. This gives rise to the rich phenomena in strong interactions. Free quarks or gluons carrying apparent color charges have never been observed because of the confinement nature of strong interactions. As opposed to QED interactions the coupling between a pair of colored objects in QCD becomes stronger as their distance increases, and at some point it becomes energetically favorable to create another pair of colored objects out of the vacuum so that when combined with each one of the original pair they form colorless particles. On the other hand it was discovered that the QCD theory has another property called the asymptotic freedom which states that as the colored objects come closer their interaction

strength decreases [1]. In particle physics short distance is equivalent to high momentum transfer in the process of probing the fine structures at such distance scale. The strength of the strong interaction has been calculated theoretically and measured through different experimental observables, as shown in Figure 1.2.

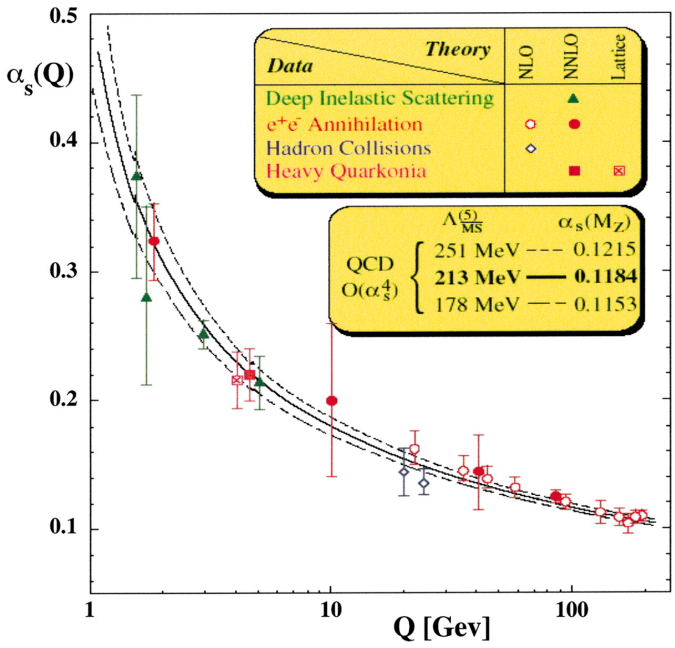

Figure 1.2: The running coupling constant of strong interaction calculated theoretically and measured by different experiments as a function of the energy scale [2]

The asymptotic freedom property of QCD offers a theoretical advantage that the calculations at short distance scale can be done perturbatively, order by order in terms of the coupling constant $\alpha_s(Q)$. For example to date the scattering cross-sections between partons (quarks and gluons) can be calculated at next-to-next-to-leading order (NNLO) for some processes [3]. However short distance partonic interactions only accounts for one piece of information needed to describe the entire scattering process. There are additional non-perturbative stages related to how partons are distributed in the original hadrons and how the outgoing colored partons becomes the final state colorless particles we observe. To address the non-perturbative part of the scattering process powerful factorization theorems have been developed, which systematically separates the short distance analytical calculations from long distance non-perturbative functions. The strength of QCD factorization

lies in the universality of these non-perturbative functions: the ones related to initial state distributions of partons inside a hadron are called the Parton Distribution Functions (PDF) while the other describing how partons become final state particles are parameterized as the Fragmentation Functions (FF). Once universality is proven for the non-pertubative functions pertaining to a specific process then one can use various experimental data to constrain and parameterize such functions. A global analysis of PDFs and FFs will enable theorists to make predictions on various other observables with different kinematics. One common example is unpolarized production cross-section of jets and hadrons in collider experiments. In this case the differential cross-section can be written as

$$E_h \frac{\mathrm{d}\sigma^3}{\mathrm{d}^3 p_h} = \sum_{abc} \int \mathrm{d}x_a \mathrm{d}x_b \frac{\mathrm{d}z}{z} f_{a/A}(x_a) f_{b/B}(x_b) \mathcal{H}(a+b \to c+X) \mathcal{D}_{h/c}(z) \tag{1.1}$$

in which $f_{a/A}(x_a)$ and $f_{b/B}(x_b)$ are the aforementioned PDFs, representing the probability of finding a parton which carries momentum fraction x_a (x_b) of the parent nucleon A (B). $\mathcal{H}$ is the hard-scattering part given by perturbative-QCD (pQCD) calculations, in this case it denotes the particular process of parton a scatters off parton b and one of the outgoing partons is c. The species of the other outgoing parton is not specified and is integrated over (denoted by X) because we are interested in the inclusive production of c. $\mathcal{D}_{h/c}(z)$ represents the probability of observing a hadron h as a result of the fragmentation process of parton c, and the fraction of the momentum of parton c taken by h is z. In the case of jet cross-section measurement the Fragmentation Function $\mathcal{D}_{h/c}(z)$ does not appear because the purpose of jet reconstruction is to directly measure the kinematics of the outgoing parton c. Fig 1.3 shows two examples of jet cross-section measurements at different center-of-mass energies and the comparison with next-to-leading order pQCD calculations. The consistency between experimental measurements and theory predictions over 10 orders of magnitudes of the data marks the great success of QCD framework for high-p_T hard processes.

Since universality can be proven for a variety of unpolarized PDFs and FFs, one can utilize special probes to study the structures of composite hadrons such as the proton. One of the probes ideal for this purpose is deep inelastic scattering (DIS) of leptons (electrons or

muons) off protons and will be discussed in the next section.

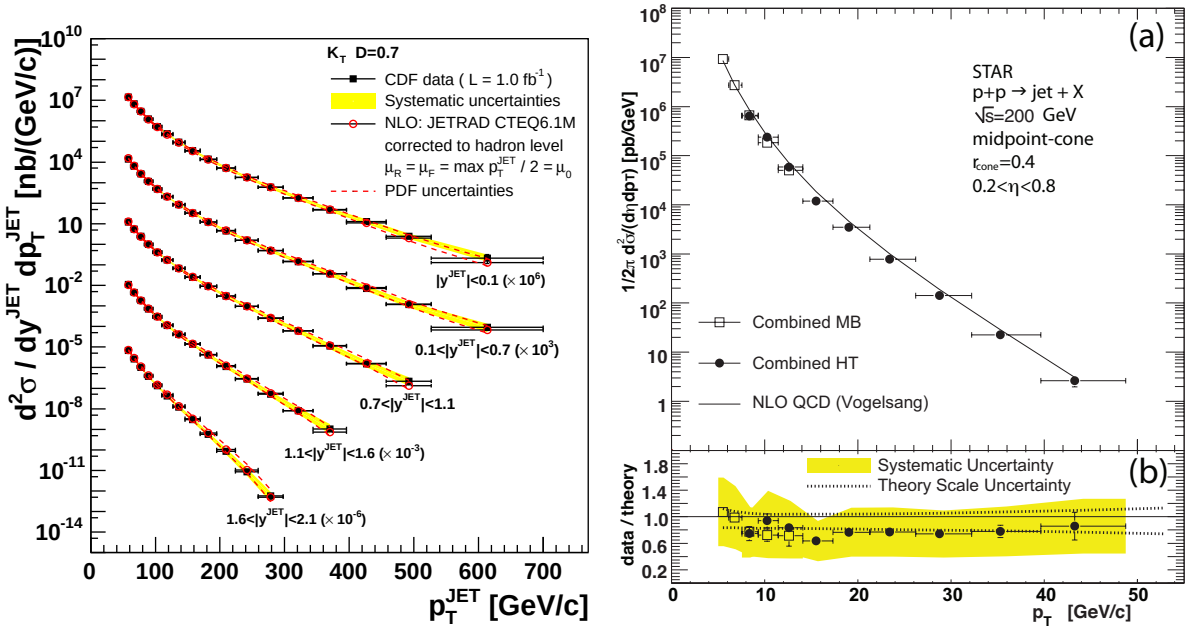

Figure 1.3: Jet cross-sections at different energy scales, Left: $\sqrt{s} = 1.96TeV$ [4], Right: $\sqrt{s} = 200GeV$ [5]

1.3 The Structure of Proton

Since its discovery in 1917 by E. Rutherford, proton was thought be an elementary particle without any internal structures and acts as the building block of all elements. In 1960s with the presence of a multitude of particles discovered by then, people set out to formulate a systematic approach to categorize them. One of the successful methods is the so called *Eightfold Way* proposed by Murray Gell-Mann [6] and Yuval Ne'eman [7]. This method has motivated the quark model developed by Gell-Mann and George Zweig [8] independently, based on the hypothesis of the existence of more fundamental constituents called *quarks* and the $SU(3)$ symmetry among the three flavors (up, down and strange) of them. In this system proton (p) belongs to the baryon octet family and is composed of three valence quarks–two up (u) quarks and one down (d) quark, as shown in Figure 1.4. It should be pointed out that quarks were initially proposed as pure mathematical concepts in order to explain the

seemingly periodic characteristics (e.g. mass, charge, iso-spin) of groups of hadrons. It wasn't until 1968, through a series of deep inelastic scattering experiments conducted at Stanford Linear Accelerator Center (SLAC), that their physical existence was confirmed. Subsequently three more flavors of quarks–charm (c), bottom (b) and top (t) were also discovered.

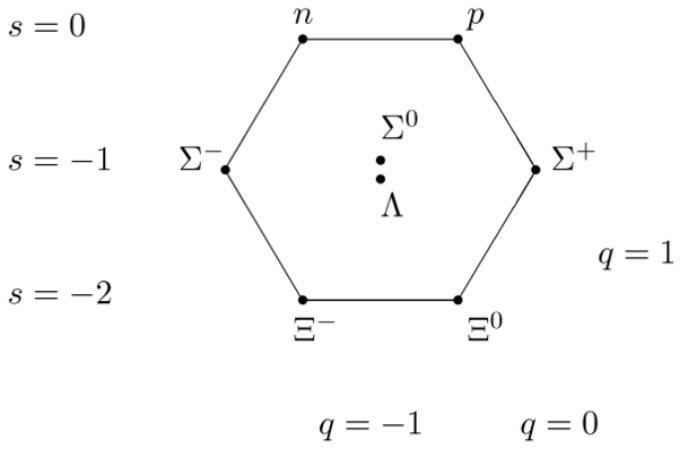

Figure 1.4: Proton (p) as in the Baryon-Octet system

1.3.1 Deep Inelastic Scattering

Deep inelastic scattering of leptons off proton is a powerful tool to probe the structure of the proton and to precisely measure the distribution of quarks inside the proton. It basically involves sending a beam of electrons or muons towards a proton target and select the ones with large scattering angles (large momentum transfers). Due to the large momentum transfer the intermediate virtual photon is sensitive to structures and dynamics at short distance scale, therefore it could provide information on point-like particles such as quarks. Since leptons do not carry color charges, their interactions with quarks are purely electromagnetic at leading order. One can obtain the virtual photon's kinematics by measuring the momentum and scattering angle of the lepton. On the other hand, in the infinite momentum frame, scatterings with large momentum transfer happen much faster than the average quark-quark or quark-gluon interactions within the proton, therefore the quark struck by the virtual photon

can be considered as a free quark and the interactions between two point-like free particles can be easily calculated. With the above line of reasoning the kinematics of quarks inside the proton can be derived from the measurement of the hard scattered leptons. A limited number of DIS experiment using neutrino beams have been performed as as well, using the Z boson instead of photon as the intermediary particle. These processes select other portions of the target hadron's PDF but the concepts are the same as for charged leptons.

Specifically we consider the process as illustrated in Figure 1.5

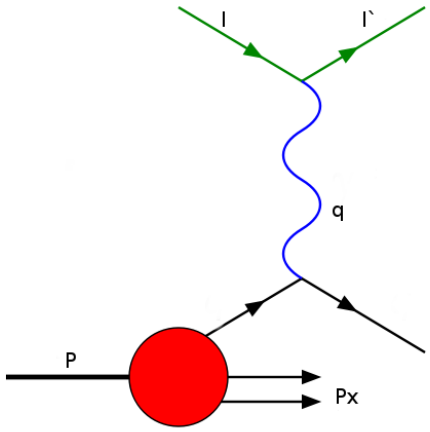

Figure 1.5: Deep inelastic scattering

Here l and l' denote the 4-momentum of the lepton before and after the scattering. q is the 4-momentum of the virtual photon. P and P_x represent the 4-momentum of the proton before and after the scattering, which are simply ignored in a inclusive DIS measurement. The following invariants are usually used to describe the DIS process [9],

$$q^2 = (l - l')^2 = -2EE'(1 - cos\theta) \tag{1.2}$$

$$\nu = \frac{P \cdot q}{M} \tag{1.3}$$

$$x = \frac{Q^2}{2P \cdot q} = \frac{Q^2}{2M\nu} \tag{1.4}$$

$$y = \frac{P \cdot q}{P \cdot l} \tag{1.5}$$

Where θ is the lepton scattering angle, ν is the virtual photon energy in lab frame, x is called the Bjorken scaling variable and y being the inelasticity, $Q^2 = -q^2$. In the infinite momentum frame the kinematics approach the Bjorken limit where ν, $Q^2 \to \infty$, with x fixed. One can easily show that in this limit, when the process is reduced to scatterings between the virtual photon and a free quark, x represents the momentum fraction of the proton taken by the struck quark. But, on the other hand, x can be calculated from the kinematics of the scattered lepton. So just by measuring the lepton before and after the scattering, one can derive the distributions of the quarks' momenta inside the proton. Formally the DIS cross-section can be written as [9],

$$d^3\sigma = \frac{1}{4P \cdot l}\frac{e^4}{Q^4}L_{\mu\nu}W^{\mu\nu}2\pi\frac{d^3l'}{(2\pi)^3 2E'} \tag{1.6}$$

The leptonic tensor $L_{\mu\nu}$ depends on the spin and momentum of the incoming and outgoing lepton. It can be calculated precisely via Feynman diagrams. The hadronic tensor $W^{\mu\nu}$ contains information on the structure of the proton and involves non-perturbative dynamics. $W_{\mu\nu}$ is usually written as the sum of a symmetric and an anti-symmetric part to facilitate the calculation of polarized and unpolarized cross-sections,

$$W_{\mu\nu} = W^S_{\mu\nu}(q, P) + iW^A_{\mu\nu}(q; P, S) \tag{1.7}$$

Furthermore the symmetric and anti-symmetric part of W can be represented by two pairs of structure functions W_1, W_2 and G_1, G_2 by factoring out variables related to kinematics of virtual photons and quarks while maintaining gauge invariance. The leptonic tensor $L_{\mu\nu}$ can also be decomposed in a similar fashion, therefore one arrives at a general expression for the cross-sections that can be easily applied to unpolarized and polarized cases [9]

$$\frac{d^2\sigma}{dE'd\Omega} = \frac{\alpha^2_{em}}{2MQ^4}\frac{E'}{E}\left(L^{(S)}_{\mu\nu}W^{\mu\nu(S)} - L^{(A)}_{\mu\nu}W^{\mu\nu(A)}\right) \tag{1.8}$$

1.3.2 Unpolarized parton distributions

The unpolarized cross-section can be obtained by averaging over the spins of the incoming lepton and of the proton in e.q. 1.8. Note that the anti-symmetric part of leptonic and hadronic tensor cancel out during the averaging, therefore one obtains

$$\frac{d^2\sigma^{unp}}{dE'd\Omega} = \frac{\alpha_{em}^2}{2MQ^4}\frac{E'}{E}L_{\mu\nu}^{(S)}W^{\mu\nu(S)} = \frac{4\alpha_{em}^2 E'^2}{Q^4}\left(2W_1 sin^2\frac{\theta}{2} + W_2 cos^2\frac{\theta}{2}\right) \tag{1.9}$$

The dimensionless structure functions F_1 and F_2 are defined as

$$F_1(x, Q^2) = MW_1(\nu, Q^2) \tag{1.10}$$

$$F_2(x, Q^2) = \nu W_2(\nu, Q^2) \tag{1.11}$$

In the Bjorken limit F_1 and F_2 depend only on x. This phenomenon has also been observed experimentally and is considered as strong evidence for the existence of point-like structures inside the proton [10]. The fact that these structure functions, or rather the DIS cross-sections, are almost independent of the momentum transfer Q^2 is strongly against the scenario of the virtual photon being scattered off by diffused medium carrying electric charges. Because if proton is made of diffused medium the DIS cross-section is going to drop rapidly as the momentum transfer increases since the greater the Q^2 the smaller distance scale the virtual photon is sensitive to, therefore the less amount of electric charge is participating the scattering. But in experiment the measured cross-section shows very weak dependence of Q^2, as shown in Figure 1.6

Existing experimental data strongly suggests that in the deeply inelastic region the virtual photon is scattered off by approximately point-like objects even at the smallest scale that current high energy leptons can probe, which is consistent with the hypothesis of structureless quarks inside the proton.

The unpolarized structure functions are related to unpolarized quark/parton distribution functions in the quark-parton model of nucleon. Under this model the hadronic tensor $W^{\mu\nu}$

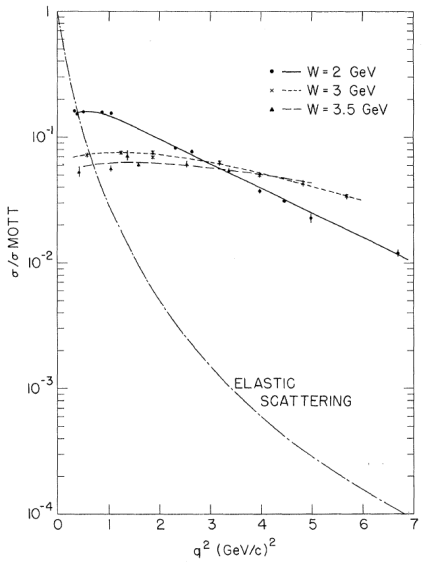

Figure 1.6: cross-section *vs* Q^2 measured by MIT-SLAC DIS experiment [10]

is represented by the so-called *handbag diagram* as shown in Figure 1.7 and is related to the quark field and quark-quark correlations.

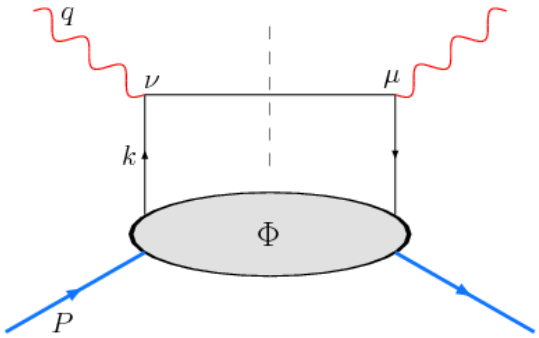

Figure 1.7: Handbag diagram of DIS

F_1 and F_2 can be extracted from the quark-parton model representation of $W^{\mu\nu}$ and they can be shown to have to following relation in the Bjorken limit

$$F_2(x) = 2xF_1(x) = \sum_a e_a^2 x f_a(x) \tag{1.12}$$

in which the first equation is called the Callan-Gross relation, the second part of the equation is the quark-parton model expression for the unpolarized structure functions. $f_a(x)$ describes

the distribution of quarks of flavor a as a function of x, the fraction of proton's momentum taken by a. To account for anti-quark contributions one can simply introduce anti-quark PDFs, e.g. $\bar{f}_a(x)$.

Various DIS experiments have measured the structure functions, e.g. as shown in the left panel of Figure 1.8. Together with global analyses, the unpolarized parton distribution functions for quarks, anti-quarks and even gluons have been extracted. By tagging the type of leading hadrons from the fragmentation of target remnants one can decompose the quark PDFs into different flavors. This is the so-called semi-inclusive DIS (SIDIS) measurement.

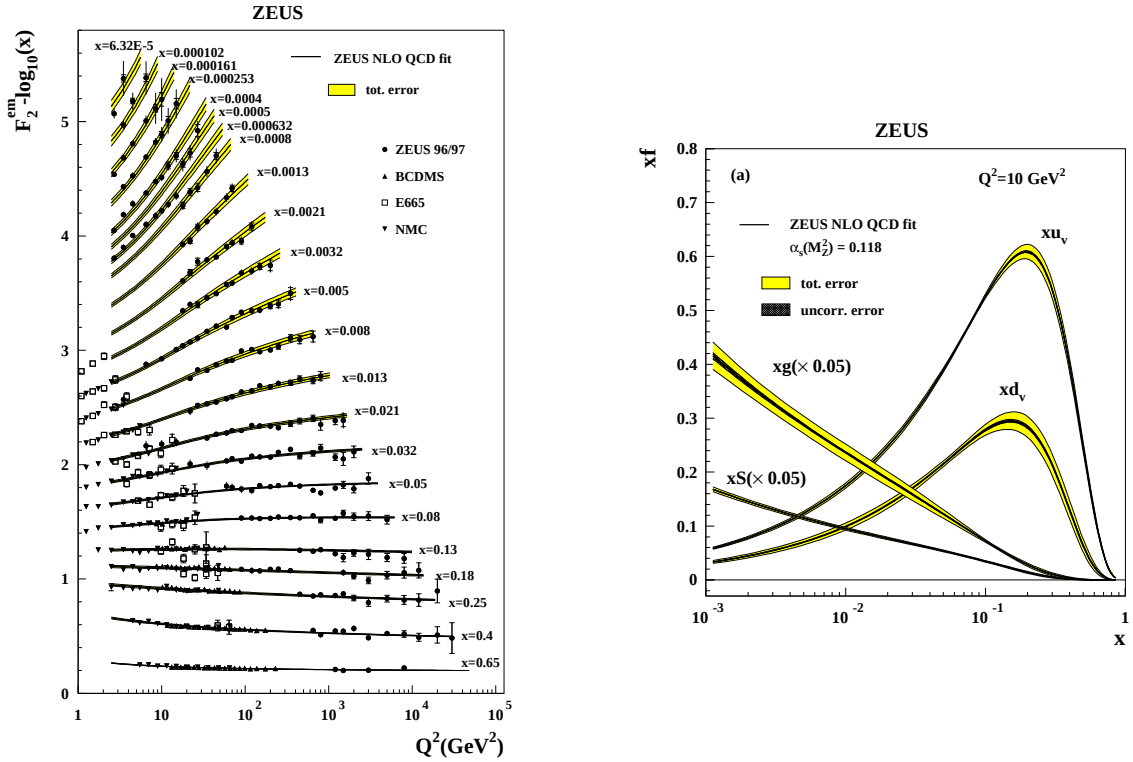

Figure 1.8: Left: F_2 structure functions measured by ZEUS and the corresponding NLO QCD fits, Right: Parton distribution functions extracted from F_2 [11]

Note that in the left panel of Figure 1.8 the structure function F_2 slightly drops at high x and Q^2, and increases as Q^2 at low x, which can be understood by the radiative emission of gluons from quarks with large x at high Q^2, and gluon splitting into quark anti-quark pair at low-x and high Q^2 region. This is precisely how the gluon distribution was derived from

DIS experiment since virtual photon does not couple with gluon at leading order. From the right panel of Figure 1.8 one can see that gluon becomes dominant at low x and its density keeps increasing towards lower x regions. But due to the unitarity constraints the gluon distribution has to saturate at some point. However, because of limited machine capability and detector acceptances, previous DIS experiments did not have enough kinematics coverage to observe the gluon saturation effects. The pursuit of low-x phenomena in nucleon and heavy nucleus has become a major research topic in recent years, especially due to its impact on our understanding of the initial conditions of heavy-ion collisions in an effort to create the Quark-Gluon Plasma [12].

1.3.3 Polarized parton distributions

To understand the detailed structure of the proton the next step forward is naturally to extract the spin information, namely how the spin and orbital motions of its constituents contribute to the spin of the proton itself. The quest for the spin structure of the proton brings both theoretical and experimental challenges. In theory there need to exist a consistent sum rule for the decomposition of proton spin into different components, the sum rule has to be unambiguous in terms of the physical interpretation of each component and at the same time translates to experimentally measurable quantities. A few candidate sum rules have been considered within the theory community, the first one is the Jaffe-Manohar sum rule [13]

$$\frac{1}{2} = \frac{1}{2}\Delta\Sigma + \Delta G + L_q + L_g \tag{1.13}$$

in which $\frac{1}{2}\Delta\Sigma$ represents the contributions from quark spin to the proton spin, ΔG represents gluon spin contributions and L_q, L_g being the quark and gluon orbital angular momentum. This sum rule has the desired properties that each term is gauge invariant and can be translated into an integral over the respective partonic densities. But it is difficult to relate L_q and L_g to experimental observables.

The second sum rule is the one proposed by Ji [14] which states that

$$\frac{1}{2} = J_q + J_g = \frac{1}{2}\Delta\Sigma + J_g + L_q \tag{1.14}$$

where the total angular momentum J_q and J_g are gauge invariant. Ji also showed that J_q and J_g can be measured in deeply virtual Compton scattering process (DVCS). However further decomposition of J_q and J_g exhibits problems. Although $\frac{1}{2}\Delta\Sigma$ still represents quark spin contributions and permits integration over quark densities, L_q on the other hand contains quark-gluon interactions which can not be simply interpreted as quark orbital angular momentum. J_g can not even be separated in a gauge invariant way into gluon spin and orbital angular momentum, only J_g as a whole is physically meaningful [14] [15]

Albeit facing theoretical uncertainties experimentalists have engaged in a series of efforts to measure $\Delta\Sigma$ [16] [17], ΔG [18] in Jaffe-Manohar sum rule and J_q, J_g through DVCS [19]. In the case of Jaffe-Manohar sum rule $\Delta\Sigma$ can be extracted from the spin asymmetries with longitudinally polarized lepton beam and proton target in a DIS experiment

$$A_{long} = \frac{d\sigma^{\leftarrow\Rightarrow} - d\sigma^{\leftarrow\Leftarrow}}{d\sigma^{\leftarrow\Rightarrow} + d\sigma^{\leftarrow\Leftarrow}} \tag{1.15}$$

with the superscripts $\leftarrow$, $\Rightarrow$ indicating the polarization direction of the beam and target respectively. Notice that the denominator is simply the unpolarized cross-section thus involves F_1 and F_2 structure functions. The numerator can be expressed by two polarized structure functions g_1 and g_2 using the general results in e.q. 1.8. The significance of the polarized structure functions g_1 and g_2 lies in their quark-parton model interpretations where g_1 is related to quark (anti-quark) polarized parton distribution functions via

$$g_1(x) = \frac{1}{2}\sum_a e_a^2 \left(\Delta f_a(x) + \Delta \bar{f}_a(x)\right) \tag{1.16}$$

whereas g_2 partially depends on g_1 and at the same time also contains higher-twist effects [9]

$$g_2(x) = -g_1(x) + \frac{1}{2}\sum_a e_a^2 g_T^a(x) \tag{1.17}$$

in which g_T incorporates both finite quark mass contributions and twist-3 component generated by quark-gluon interactions [9]. From the above relations it can be seen that longitudinal

spin asymmetry measurements from polarized DIS experiment could provide information on the quark and anti-quark polarized parton distribution functions. These polarized distribution functions admits similar probabilistic interpretations as their unpolarized counterpart, for example

$$\Delta f_a(x) = f_a^{\uparrow}(x) - f_a^{\downarrow}(x) \tag{1.18}$$

Namely $\Delta f_a(x)$ quantifies the difference in the probabilities of quark carrying flavor a has its spin aligned with the proton spin versus anti-aligned, when the proton is longitudinally polarized with respect to the beam. DIS data could constrain quark polarized PDFs pretty well but not so much for sea quarks and gluons. Figure 1.9 shows the results of three global analyses with DIS data [20].

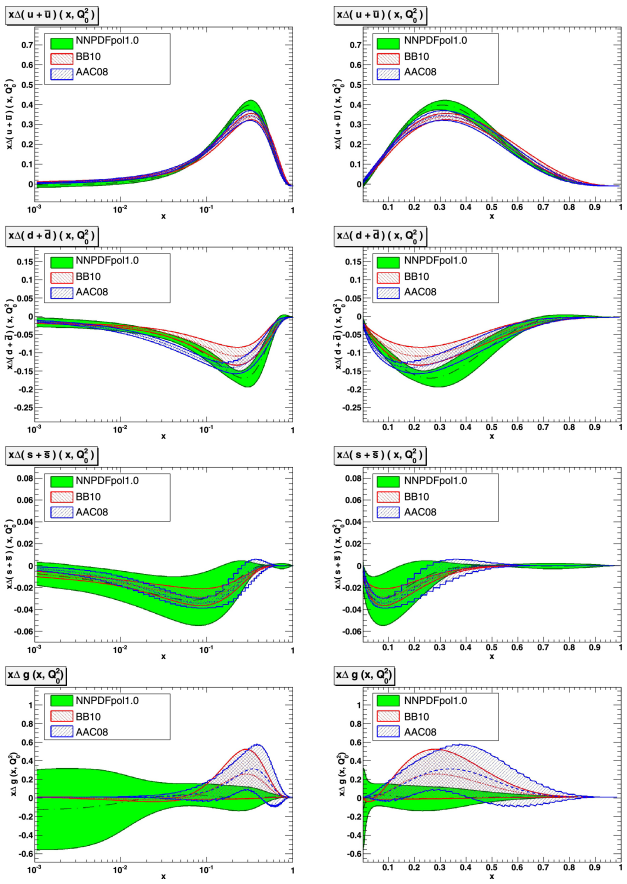

Figure 1.9: Polarized parton distributions extracted by three global analyses on DIS data[20]

The most striking result obtained from polarized DIS experiments is that quark spin only

contributes to about 30% of the proton spin [16] [17] [20], the rest must come from gluons and orbital angular momenta.

Due to limited kinematics coverage and the fact that gluons only emerge through next-to-leading order processes deep inelastic scattering is not the best tool to access sea quark and gluon polarizations. In fact they are most extensively studied in hadronic collisions, for example through $W^{\pm}$ [21] [22] and jet [18] productions at Relativistic Heavy-Ion Collider (RHIC) at Brookhaven National Laboratory (BNL).

Better understanding of proton structure eventually has to come from our improved knowledge on the strong interactions described by QCD theory. In practice the proton serves as a manageable laboratory to which we can test our predictions and update our theoretical framework. One of the important conclusions from QCD theory studies is that the aforementioned unpolarized and longitudinally polarized PDFs do not contain enough information on the proton structures to allow for a complete description even with leading-order accuracy on the experimental data. To understand such argument one simply needs to realize that in relativistic theory spatial rotations do not commute with boost transformation, therefore the spin structures of the proton as probed by longitudinally polarized beams and targets are not equivalent to the structures probed transversely, namely when the spin of the proton is perpendicular to its momentum direction. In leading order calculations they are complementary to each other and are both indispensable. In the extreme ideal case if we have complete knowledge on the proton structure and have obtained its full wave function by solving QCD Lagrangian on such a composite system, we would be able to derive its longitudinally and transversely polarized PDFs from one another by applying rotation and boost in different orders. But in reality since we do not have such an omnipotent wave function the best we can do is to study these two configurations separately in order to recover as much information on the proton structure and/or the master wave function as possible. To that end the main contribution of this thesis work is to measure the proton's transverse spin structure and to learn about the QCD dynamics responsible for the asymmetries of the particle production that we measure in transversely polarized *pp* Collisions

1.4 Transverse Single Spin Asymmetries

The particular form of asymmetry studied in this work is called the Transverse Single Spin Asymmetry (TSSA),

$$A_N = \frac{d\sigma^{\uparrow} - d\sigma^{\downarrow}}{d\sigma^{\uparrow} + d\sigma^{\downarrow}} \tag{1.19}$$

namely the difference in the production cross-sections of a certain final state when flipping the spin orientation of the transversely polarized proton beam (or proton target, in the case of DIS) while averaging over the spin of the other beam, then divide it by the unpolarized cross-section. The final states considered in this work are π^0 and jets. Unlike the small longitudinal asymmetries of various final states the amplitude of TSSA for many final states (charged pions, kaons, eta mesons, lambdas, protons and neutrons) are often very large, which has stimulated a lot of interest in the theory community since its discovery [23] [24]. It has been shown that in conventional leading-twist collinear QCD factorization framework these transverse asymmetries should be highly suppressed due to the Chiral-odd nature of transversely polarized quark PDFs [9]. The observation of such large asymmetries as shown in Figure 1.10 have motivated theorists to consider effects beyond the collinear picture of partons inside the proton and next-to-leading twist distributions involving muti-parton correlations.

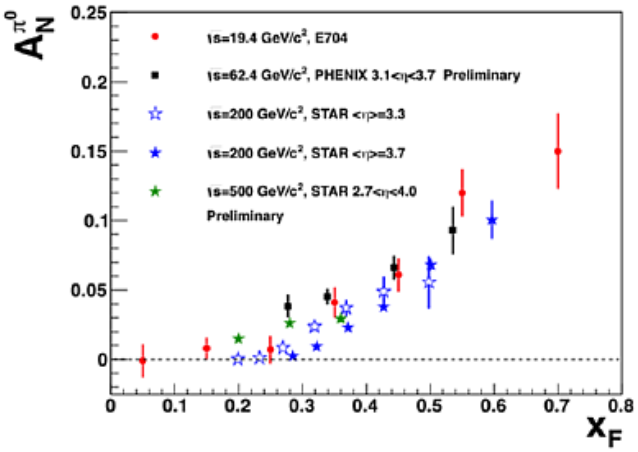

Figure 1.10: TSSA of π^0 production in various center-of-mass energies

The magnitude of A_N rises as Feynman-x variable x_F which is related to Bjorken-x in e.q. 1.4 via the relation

$$x_F = x_{bjor,1} - x_{bjor,2} \tag{1.20}$$

with $x_{bjor,1}$ and $x_{bjor,2}$ being the Bjorken-x of the parton from the polarized beam and that from the unpolarized beam, respectively. The asymmetry increases when the partons participated in the hard partonic collisions become more and more asymmetric in terms of their momentum fractions. Processes with large x_F usually ended up having most of their final state products going in the forward direction with respect to the polarized beam because of momentum conservation, so experimentally it is of more interest to conduct measurements at forward rapidities.

On the theory side the description regarding the origins of large TSSAs generally fall into two categories, those invoking Transverse Momentum Dependent (TMD) factorization approach and those including sub-leading twist distributions within collinear framework. These two categories generally deal with different processes and they have been shown to be equivalent in their overlapping kinematic region [25]

1.4.1 TMD framework

In conventional collinear factorization calculations the transverse motion of partons in both PDFs and FFs are averaged out before the convolutions with the perturbative hard scattering stages. Specifically the integration over partonic transverse momentum is always carried out first, e.g.

$$f_{a/A}(x) = \int f_{a/A}(x, k_T) \mathrm{d}k_T \tag{1.21}$$

But in the TMD framework explicit dependence on intrinsic transverse momentum is allowed, both k_T-dependent distribution and fragmentation functions acquire additional contributions which are spin-dependent. Under this framework the cross-section is usually written in the following factorized form

$$\sigma(p_h, \overrightarrow{S}) \propto f_{a/A}(x, k_T) \otimes \hat{\sigma}_{parton} \otimes D_{h/c}(z, P_T) \tag{1.22}$$

It should be noted that the TMD factorization theorem has only been proven for a few processes such as SIDIS [26] and Drell-Yan production [27]. For general hadron production in proton collision the validity of the TMD factorization is still an assumption [28]. One of the conditions for the applicability of TMD factorization is that the process should involve two different scales Q and Q_T such that $Q \gg Q_T \geq \Lambda_{QCD}$ where Λ_{QCD} is approximately 200 MeV. For example in SIDIS process the momentum transfer Q can be directly measured by detecting the scattered lepton, and Q^2 needs to be large for the pertubative calculation to work. At the same time the transverse momentum of the produced hadron with respect to the virtual photon direction serves as another scale Q_T, which need to be small enough in order to be sensitive to the intrinsic transverse momentum of its parent parton.

1.4.1.1 Sivers asymmetry

In eq. 1.22 the k_T and spin-dependent distribution function is called the Sivers function and is written as

$$f_{q/h\uparrow}(x, \overrightarrow{k}_T, \overrightarrow{S}) = f_{q/h}(x, k_T) + \frac{1}{2}\Delta^N f_{q/h\uparrow}(x, \overrightarrow{k}_T)\overrightarrow{S} \cdot \hat{p} \times \hat{k_T} \tag{1.23}$$

The first term is a spin-independent piece but the second term depends on the spin orientation of the proton. Physically the Sivers function $\Delta^N f_{q/h\uparrow}(x, \overrightarrow{k}_T)$ signifies the correlation between parton intrinsic transverse momentum and the spin of the proton. In a simple model developed in [29] the Sivers function is connected to quark orbital angular momentum. On the other hand Sivers function is naively time-reversal odd and is supposed to disappear due to the invariance of strong interactions under time-reversal transformation. In order for the asymmetries to survive the amplitude of the Sivers function must be equipped with an additional phase through a gauge link $\mathcal{P}e^{ig\int_y^\infty A(\lambda)\mathrm{d}\lambda}$ [30]. This phase is process-dependent and is generated by the interactions between the active parton and the remnant of the proton. For example the leading order diagrams that generate the TSSA in DIS and Drell-Yan processes are shown in Figure 1.11

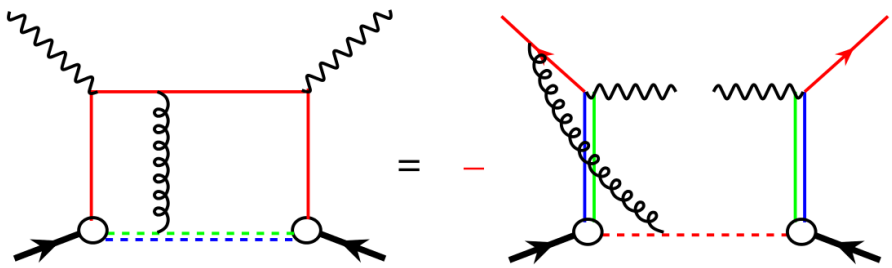

Figure 1.11: Sivers function for DIS (Left) and Drell-Yan (Right) process

Non-zero Sivers function in the DIS process is generated by the final state interactions between the struck quark and spectators of the proton which did not participate in the hard scattering, whereas in Drell-Yan production it is generated via the initial state interactions between the quark (or anti-quark) and the beam remnants. The relation between the Sivers functions involved in these two processes are governed by the Modified Universality rule which states that they only differ by a sign [31]. This relation serves as one of the most stringent tests for the QCD theory description of the origins of transverse spin asymmetries and has stimulated a lot of efforts on the experimental side within communities at BNL/RHIC, CERN/COMPASS and Fermilab.

1.4.1.2 Collins asymmetry

While the transverse spin asymmetries can be generated by the initial state correlations in the Sivers mechanism, they can also arise through correlations in the final state during the fragmentation of the hard scattered parton. The later is the so called Collins mechanism [32], in which the asymmetries are generated by the correlations between intrinsic transverse momentum of the produced hadron from the fragmentation and the spin of its parent parton after hard scattering. The spin-dependent production cross-section contains a term that is proportional to $H_1^{\perp}(z, k_T^2)[\widehat{k \times P_h} \cdot \hat{S}]$, where $\hat{S}$ is the unit vector of the spin of the parent parton and $\widehat{k \times P_h}$ is the unit vector of the cross product of parton and hadron's momentum. Experimentally this vector triple product generates a $\sin\phi_C$ modulation of the cross-section for which the amplitude is determined by the Collins function $H_1^{\perp}(z, k_T^2)$. ϕ_C is called the

Collins angle and can be written as the difference between the azimuthal angle of parton's spin and that of the hadron's transverse momentum with respect to parton's momentum direction on the scattering plane. A schematic diagram of the geometry for Collins mechanism in polarized proton collisions is shown in Figure 1.12.

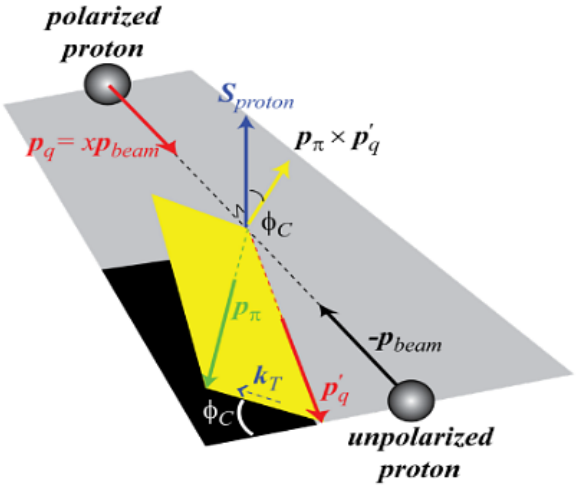

Figure 1.12: Collins mechanism in pp collisions

At large x_F the parton originated from the polarized proton beam has high probability of maintaining its spin orientation through the hard scattering. Therefore the transversely polarized parton distribution function, or transversity distribution $h_1(x)$, can manifest itself by its coupling with the Collins fragmentation function via

$$\sigma(p_h, \overrightarrow{S}) \propto h_1(x) \otimes \hat{\sigma}_{parton} \otimes H_1^{\perp}(z, k_T^2) \tag{1.24}$$

since both of them are chiral-odd together they form a chiral-even product that can be measured in physical processes.

1.4.2 Collinear Twist-3 framework

In contrast to TMD approach the twist-3 formalism stays within the collinear framework but instead attributes the asymmetries to sub-leading twist effects. Note that the leading twist term (twist-2) of the operator product expansion of the structure functions (or rather the

bi-local product of two quark currents) results in the three parton distribution functions mentioned previously–unpolarized, longitudinally polarized and transversely polarized PDFs. At twist-3 level three parton correlations are involved and they contain spin-dependent contributions which are responsible for generating spin asymmetries [33]. For example Figure 1.13 shows a Feynman diagram for the generation of TSSA for inclusive hadron productions via initial-state correlations in polarized proton collisions [34].

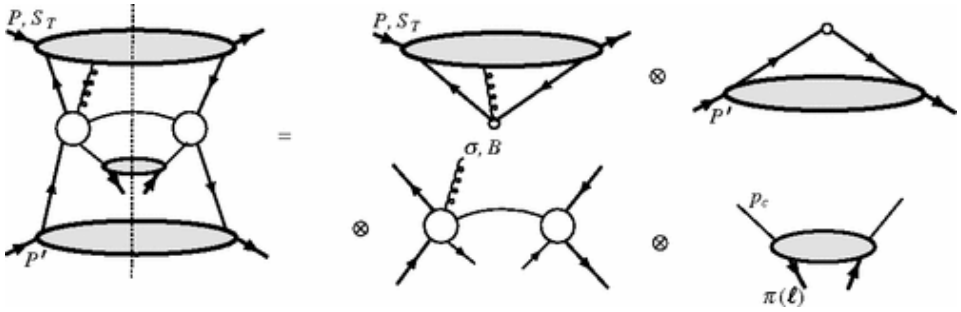

Figure 1.13: Initial state twist-3 contributions to the TSSA of hadron production in *pp* collisions [34]

The above figure indicates that the spin-dependent cross-section can be generated via the convolution between initial state quark-quark-gluon correlation functions, a hard scattering matrix with interference of two- and three-particle systems and a usual fragmentation function. Mathematically,

$$E_h \frac{\mathrm{d}\Delta\sigma}{\mathrm{d}^3 P_h} \propto \sum_{abc} D_{h/c}(z_c) \otimes f_{b/B}(x_b) \otimes T_{a,F}(x,x) \otimes H_{ab\to c} \tag{1.25}$$

of which the most important piece is the Efremov-Teryaev-Qiu-Sterman (ETQS) function $T_{q,F}(x,x)$ [33] [35] that encodes the quark-quark-gluon correlations in the initial state. The ETQS function is related to the Sivers function in TMD scheme via an integral relation

$$T_F^q(x,x) = -\int d^2\overrightarrow{p}_\perp \frac{\overrightarrow{p}_\perp^{\,2}}{M} f_{1T}^{\perp q}(x, \overrightarrow{p}_\perp^{\,2})|_{SIDIS} \tag{1.26}$$

In addition to initial state twist-3 functions final state interactions and fragmentations also admit twist expansions. The twist-3 fragmentation function and its relations with the

Collins function have been under consideration in recent years in order to provide better description of the experimental data [36].

Unlike TMD framework the twist-3 formalism generally applies to processes that only involve a single hard scale, for example inclusive jet and hadron productions at high-p_T in proton collisions and high-p_T regions in DIS processes. Due to this reason measurements conducted in this thesis work are more appropriately described by twist-3 formalism. Being a subleading twist effect the transverse single spin asymmetries are expected to decrease as $\mathcal{O}(\frac{1}{P_T})$.

The remaining chapters of this document are arranged as follows: Chapter two mainly describes the experimental facilities involved in making the measurements of TSSA for inclusive π^0 and jet production possible in polarized proton collisions; Chapter three discusses the methods used to extract the asymmetries from experimental raw data; Chapter four shows the results as well as their physics implications; Chapter five describes simulation works related to future detector upgrades in order to expand the experimental program on TSSA measurements; and finally Chapter six provides a summary and outlook.

CHAPTER 2

Experimental Setup

The polarized proton-proton collision data analyzed in this thesis work is collected by the STAR (Solenoidal Tracker At RHIC) detector at the Relativistic Heavy Ion Collider (RHIC) at Brookhaven National Laboratory (BNL). This chapter provides a general introduction to the RHIC facility and the STAR detector system. One of the forward detector subsystems, the Forward Meson Spectrometer (FMS), played a central role in the analysis and will be described in detail.

2.1 Relativistic Heavy Ion Collider

The Relativistic Heavy Ion Collider is a high energy, multi-purpose particle collider located at Brookhaven National Laboratory in Long Island, New York. It is by now the world's only collider capable of colliding polarized proton beams at relativistic energies up to $\sqrt{s}$ = 510 GeV, which puts it at the center of precision QCD studies and proton structure measurements within the QCD community. RHIC's unique versatility also makes it possible to deliver heavy ion collisions with a wide range of species, from uranium all the way down to deuterium, in a wide range of energies from 200 GeV per nucleon to a few GeV. The main focus of heavy ion running is to study nuclear matter in extreme conditions. The hot and dense environment created in heavy ion collisions are believed to have existed moments right after the Big-Bang of our Universe, therefore the study of the strong interactions within matter under these extreme condition could potentially shed light on the conditions of the early formation of our Universe [37] [38].

Particles are accelerated in the RHIC complex through multiple stages before reaching

their top energy and are brought into collisions. Figure 2.1 shows a sketch of the essential components of the accelerator facility.

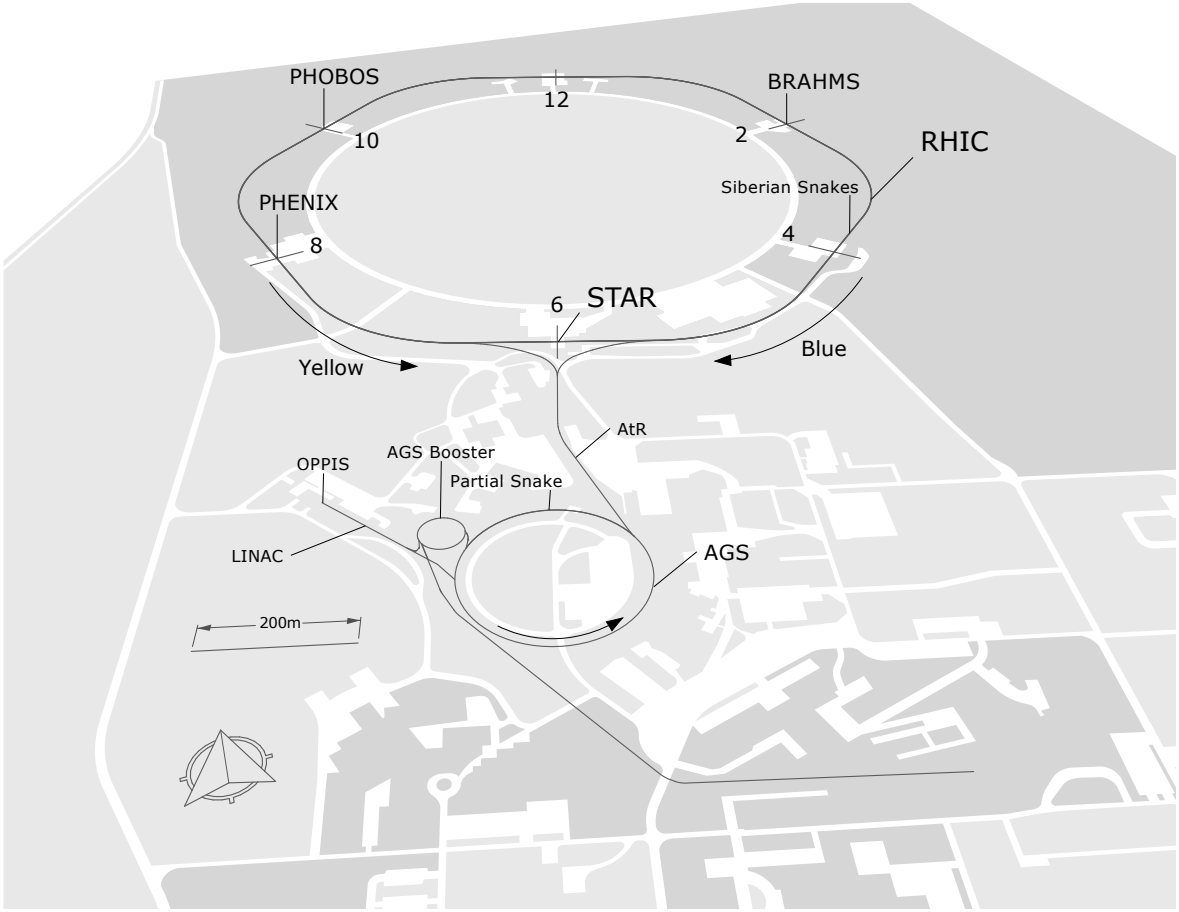

Figure 2.1: The RHIC complex

2.1.1 RHIC as a polarized proton collider

In the polarized proton mode protons starts off in the form of H^- ions from the Optically-Pumped Polarized H^- Source (OPPIS) [39], where the initial energy out of the source is 35 KeV. The polarized H^- ion beam is then accelerated to 200 MeV in the linear accelerator (LINAC) for the strip-injection to Booster Synchrontron, where the electrons are stripped off and they become bare protons. The H^- ion pulse is captured in a single Booster bunch [40] before being transferred to the Alternating Gradient Synchrontron (AGS). The term "Alternating Gradient" refers to the fact that the field gradients of a pair of focusing magnets

in AGS are alternated in orthogonal directions, so that the overall effect is to focus beams in both directions [41]. The AGS itself used to be the main high energy experiment facility before the RHIC era, it is well known for its role in three Nobel Prize discoveries, the J/Ψ particle (1974), the CP violations in kaon decay (1964) and the discovery of muon neutrino (1962). The protons are accelerated to 24.3 GeV before injection into RHIC. Through the AGS to RHIC transfer line the proton bunches are injected into two quasi-circular rings (Blue and Yellow rings) in which they circulate in the opposite directions. The circumference of the RHIC ring is 2.4 miles and consists of 1740 superconducting magnets. In the ring the proton beams can be further accelerated up to 255 GeV before being brought into collisions at six interaction points. The STAR experiment is located at 6 clock of the ring while the PHENIX experiment is at 8 clock. There were two smaller scale experiments at 10 and 2 clock interaction point, PHOBOS and BRAHMS, but have been decommissioned since 2006.

As the polarized protons are accelerated in AGS and RHIC ring it is crucial to maintain their polarization. Due to the existence of the orbit guiding dipoles in order to to keep the beams in the ring the magnetic field is mainly in the vertical direction. Therefore the stable direction of proton's spin vector is vertical, or transversely polarized. In the ideal case when the spin of the proton is perfectly aligned with the orbit guiding dipoles' magnetic field the proton beam is not going to lose its polarization. In practice due to misalignment the proton spin will precess along the direction of the transverse magnetic field, but its vertical component will remain stable. The existence of orbit focusing magnets and localized imperfections in the guiding magnets both introduce magnetic field in the longitudinal direction along the beam. The longitudinal magnetic field tends to drive the spin away from its stable vertical direction, however most of the time this disturbance is in random direction. The real problem is that in the course of an acceleration there are times when the proton spin points to the same direction every time it arrives at the same location, so that the spin vector gets pushed away towards the same direction by the longitudinal field in every revolution. These are called depolarizing resonances.

To fight against depolarizations a new device was invented by former Soviet scientists Derbenev and Kondratenko from the Institute of Nuclear Physics, Novosibirsk [42]. This

device is called the Siberian Snake which consists of a group of helical magnets. It rotates the spin of the proton by 180 degrees vertically every time the proton bunches pass through it. With two sets of full Siberian Snakes installed at RHIC the spin of the proton will be pointing to opposite directions in the transverse plane after a full revolution when it reaches the depolarizing resonance, while the vertical component remains in the same direction. Therefore the disturbance of the longitudinal field is in completely opposite directions every time the beam passes through it and the depolarization effect cancels out. With Siberian Snakes the average polarization of the proton beams at RHIC could be kept at about 50% in stores lasting over 10 hours.

Since the proton beams are transversely polarized during acceleration and store in order to get longitudinal polarizations a pair of spin rotators are installed at each interaction point. The spin rotators are similar to Siberian Snakes but they only rotate the spin vector by 90 degrees. After the collision the spin vector will be turned by another rotator so the beam remains in transverse polarization in the RHIC ring.

2.1.2 Polarimetry

To go from raw asymmetry measurements to physics asymmetries the extent to which the beam is polarized has to be determined with high accuracy. This is usually characterized by the beam polarization quantity, which is defined as the average of the spin component along the desired direction divided by the norm of the spin vector. In practice the beam polarization is measured with processes that have known physics asymmetries (or analyzing powers) at a polarimeter. There are two types of polarimeters installed at RHIC, the Hydrogen-jet (H-jet) polarimeter and the proton-Carbon (pC) polarimeter.

The Hydrogen-jet polarimeter measures the single and double transverse spin asymmetries of proton proton elastic scattering in the Coulomb-Nuclear Interference (CNI) region [43]. The device consists of three parts: the atomic beam source, the scattering chamber and the Breit-Rabi polarimeter. Figure 2.2 shows a schematic diagram of the H-jet target system. The atomic beam source sends a beam of highly polarized ($\approx$95% polarization)

hydrogen atoms perpendicularly through the RHIC-beam, the hydrogen atoms collide with protons from the RHIC-beam elastically in the scattering chamber then one of the recoil protons are detected by the silicon detectors mounted on the left and right hand side of the RHIC-beam. The rest of the hydrogen beam which did not participate in the scattering ends up landing at the Breit-Rabo polarimeter, where its polarization can be precisely measured.

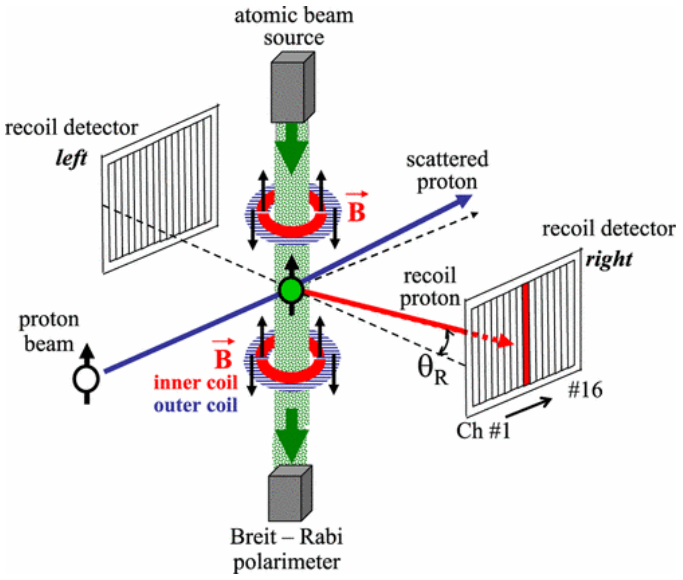

Figure 2.2: Layout of the Hydrogen-jet polarimeter setup

The single spin asymmetries of proton-proton elastic scattering can be measured and calculated by the following equation [43]

$$A_N = \frac{1}{P_T} \frac{\sqrt{N^L_{0\uparrow} N^R_{0\downarrow}} - \sqrt{N^R_{0\uparrow} N^L_{0\downarrow}}}{\sqrt{N^L_{0\uparrow} N^R_{0\downarrow}} + \sqrt{N^R_{0\uparrow} N^L_{0\downarrow}}} = \frac{\epsilon_T}{P_T} \tag{2.1}$$

where $N^L_{0\uparrow} = N^L_{\uparrow\uparrow} + N^L_{\downarrow\uparrow}$ is the number of recoil protons for selected proton-proton scattering events detected on the left of the beam with the direction of the target polarization up. P_T is the polarization of the atomic hydrogen beam as measured by the Breit-Rabi polarimeter. Due to indistinguishability of the target beam and RHIC beam during and after scattering the spin asymmetry A_N (or analyzing power) remains the same when calculated according to the spin orientations of the RHIC-beam, therefore the polarization of the RHIC-beam can be computed by

$$P_B = \frac{\epsilon_B}{P_B} \tag{2.2}$$

where ϵ_B is defined in the same way as ϵ_T except the spin is sorted according to the spin of the RHIC-beam.

The Hydrogen-jet polarimeter provides absolute beam polarization measurements, but due to its limited hydrogen beam intensity the statistical precision of this measurement over a single fill is typically 8% to 20%. Usually only the average over an entire running period is precise enough for an overall normalization on the level of 1.5%. It certainly is not able to provide fill-by-fill polarizations values for monitoring purposes or physics A_N measurements of any process. For a prompt and relative beam polarization measurements the proton-Carbon polarimeter serves as a better tool.

The proton-Carbon polarimeter utilizes the analyzing power of polarized proton-Carbon elastic scattering to monitor the relative variations of beam polarization, in which the proton comes from the RHIC-beam. Two proton-Carbon CNI polarimeter stations are located at up and down stream of the beam line at the 12 o'clock interaction point of RHIC. The polarimeter consists of an ultra-thin carbon ribbon target ($5\mu g/cm^2$) surrounded by six silicon strip detectors to provide signals for the scattered Carbon nucleus [44]. Figure 2.3 is a schematic of the layout of pC polarimeter.

In normal physics data-taking mode the p-Carbon polarimeter is inserted into the proton beam for about 10 seconds to measure the instant beam polarizations bunch-by-bunch. The beam polarization is usually measured at the beginning and end of each store, as well as every 1.5 hours in between. These measurements make it possible to quantify the decay of beam polarization over time so that more accurate physics asymmetries can be obtained from the collisions.

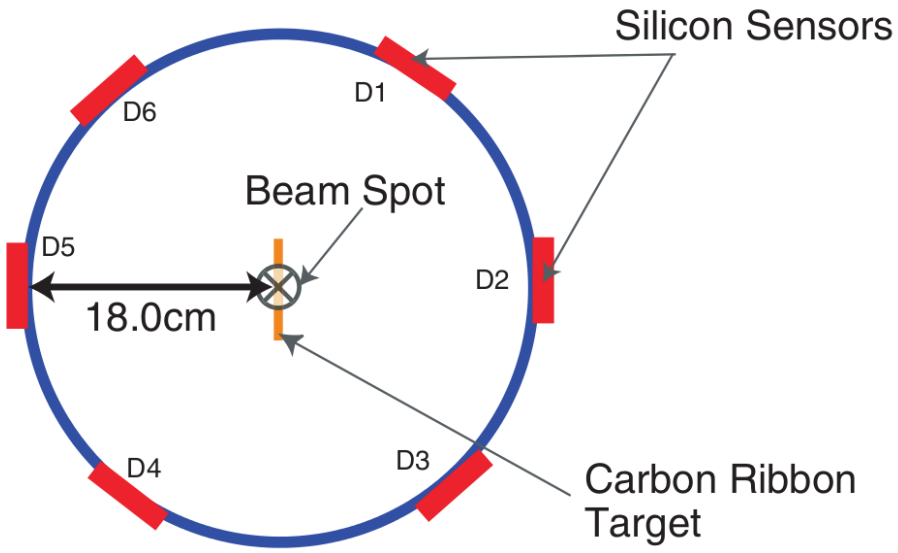

Figure 2.3: Layout of the p-Carbon CNI polarimeter setup [45]

2.2 The STAR detector system

The Solenoidal Tracker At RHIC (STAR) is one of the two major detector systems at RHIC. Its full azimuthal coverage at mid-rapidity ($|y| < 1$) as well as its forward rapidity detector subsystems support a wide range of physics measurements from high-p_T hard probes in heavy-ion collisions [46] to proton proton elastic scatterings at very small angles [47]. Figure 2.4 shows a general layout of detector subsystems of STAR.

The main central detector subsystems of STAR are the Time Projection Chamber (TPC, as shown in Figure 2.5) and the Barrel Electro-Magnetic Calorimeter (BEMC). The TPC provides tracking measurements for charged particles, their momentum, charge sign and spatial location. At the same time through measuring their ionizing power $\mathrm{d}E/\mathrm{d}x$ charged particles can be identified [48]. As a low material high-segmentation gaseous tracker TPC has the capability of measuring low momentum tracks in a high multiplicity environment, but due to the necessity of having to wait until the ionized secondary particles have drifted to the anode pad and magnified before recording the next event and the gating grid operations the readout frequency of TPC is limited to about 1.5 kHz. This rate sets the limit of the global readout speed of any trigger that requires the TPC data.

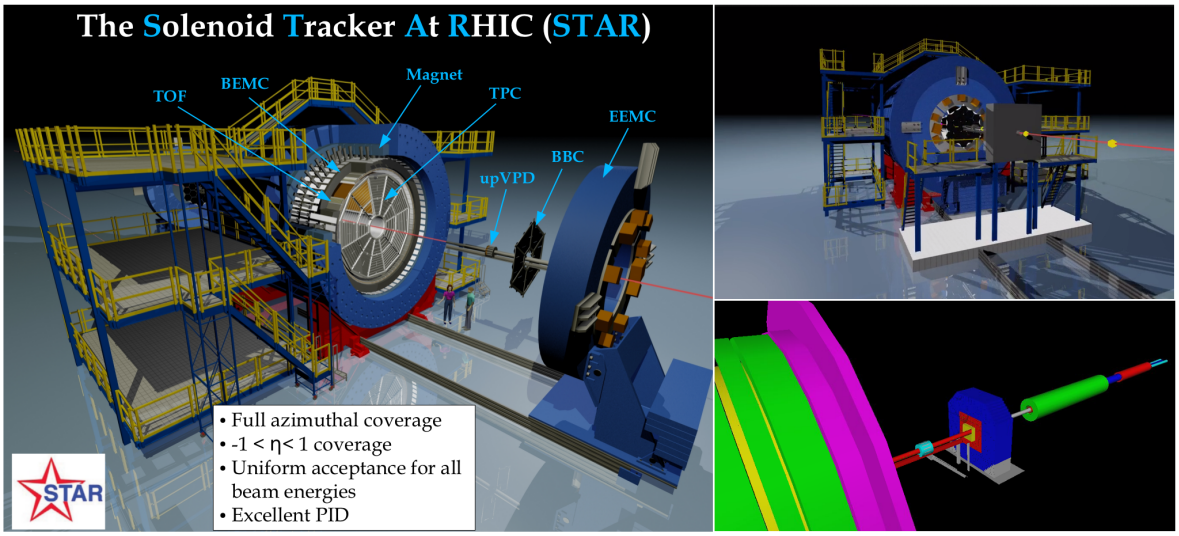

Figure 2.4: Left: Layout of the STAR detector system. Right Top: rear review of the Forward Meson spectrometer (Gray box) as seen from the west side of STAR. Right Bottom: FMS geometry as described in GEANT simulation.

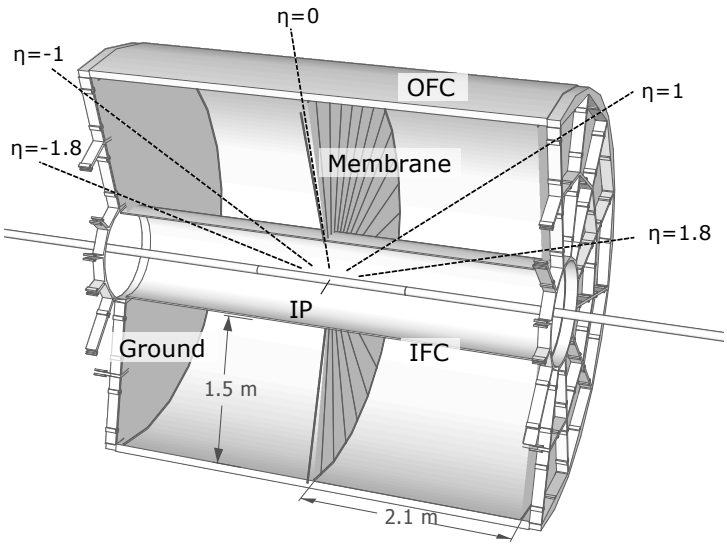

Figure 2.5: Layout of the STAR Time Projection Chamber

The Barrel Electro-Magnetic Calorimeter (BEMC) is located outside the TPC. It measures the energy and location of electrons and neutral particles such as photons through the electromagnetic (EM) showers initiated by these particles. Being a sampling calorimeter the BEMC consists of alternating layers of lead absorber and scintillating tiles [49]. The lead absorbers are mainly used to initiate the EM showers of the primary particles and absorb most of the energies of the secondary particles produced in the shower, while the particles traversing the scintillating tile produce light signals which are then collected by the Photo-Multiplier Tubes (PMT). Figure 2.6 shows the layout of BEMC and one of its 120 tower modules.

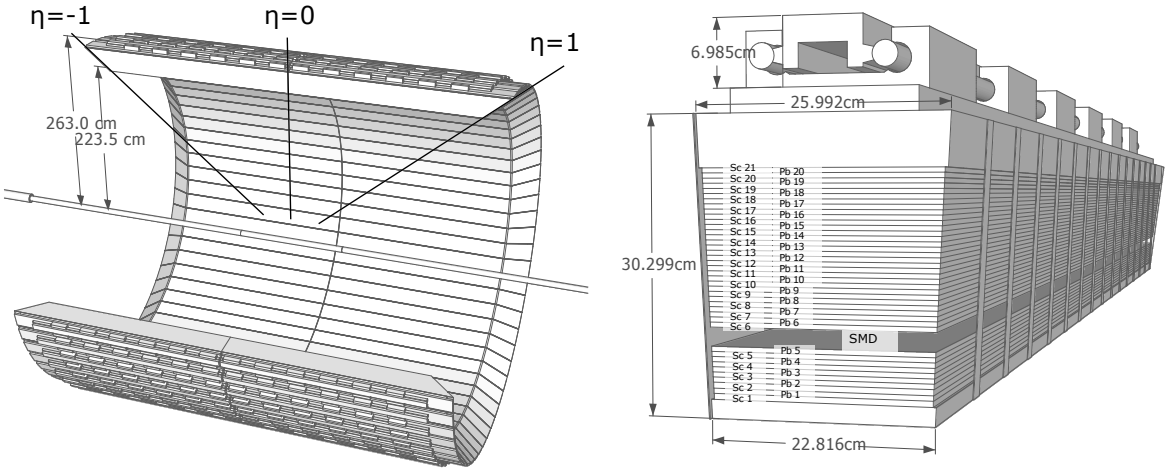

Figure 2.6: Left: Layout of STAR BEMC Right: One of the BEMC modules

The depth of the towers in the radial direction is 20 radiation length (X_0), this provides enough material to fully absorb electromagnetic showers while the nuclear interaction length is not sufficient for hadronic showers to develop. The addition of Multi-wire Proportional Chambers (MWPC) at approximately $5.6X_0$ into the tower helps discriminating EM showers against hadronic showers by measuring the shower width, since EM showers are expected to be fully developed at this depth while most of the hadronic showers are not. The two dimensional readout of the shower-max detector also provides better position resolutions. Figure 2.7 shows the layout and the readout mechanism of the shower-max detector [49].

Other important detectors in STAR include the Time-of-Flight (TOF) detector located

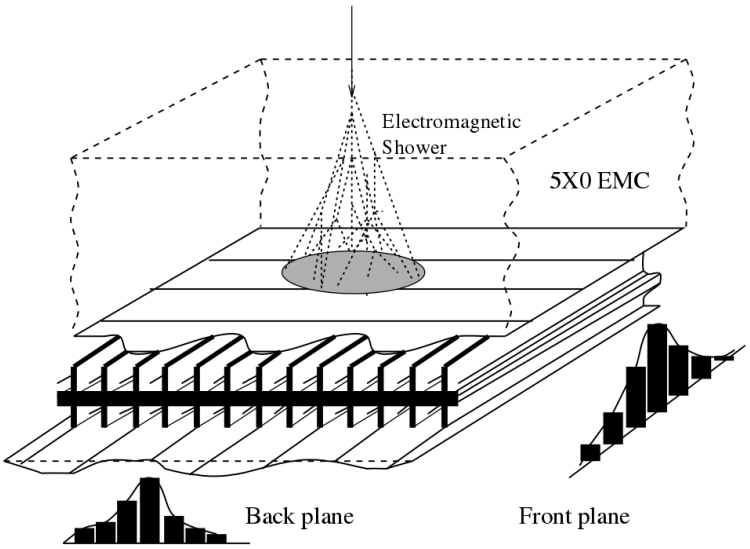

Figure 2.7: Schematic illustration of the double layer STAR BEMC Shower-Max Detector. Two independent wire layers, separated by an aluminum extrusion, image electromagnetic showers in the η and ϕ directions on the corresponding pad layers.

between TPC and BEMC which provides additional particle identification capability by measuring their flight time, the End-cap Electro-Magnet Calorimeter (EEMC) covering the mid-forward area $1 < \eta < 2$, The Beam-Beam Counter (BBC) used for minimum-bias trigger definitions as well as local polarimetry and the Muon Telescope Detector (MTD) sitting on the backlegs of the STAR magnet outside BEMC to provide muon identification. Starting from 2013 a group of new silicon vertex detectors have been installed at STAR with the goal of measuring open charm mesons (e.g. D^0) by reconstructing secondary vertices of hadron decays in nuclear collisions [50].

2.2.1 The STAR Forward Meson Spectrometer (FMS)

The main detector subsystem used in this analysis is the Forward Meson Spectrometer (FMS). FMS is an Electromagnetic calorimeter located at the west side of STAR covering pseudorapidity $2.6 < \eta < 4.0$. It consists of 1264 lead glasses with two different sizes, the 576 large cell modules (cross-sectional area = 5.8 cm x 5.8 cm, length = 60 cm) cover the perimeter area $2.6 < \eta < 3.3$ while the 488 small cells (cross-sectional area = 3.8 cm x 3.8

cm, length = 45 cm) provide higher granularity for large rapidity region ($3.3 < \eta < 4.0$). The right panel of Figure 2.4 shows the rear view of the FMS from west side of STAR and the FMS geometry in GEANT4 detector simulation software [51]. Figure 2.8 shows configurations of the lead glass stack and their physical locations in terms of pseudorapidity assuming the interaction point is at the center of the TPC.

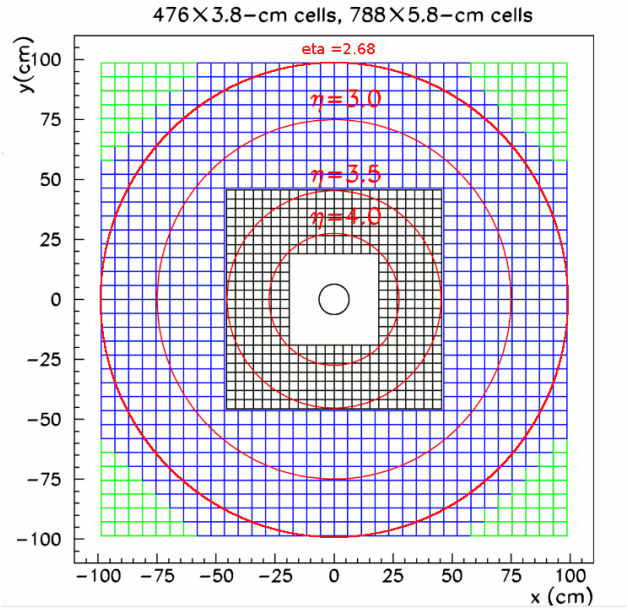

Figure 2.8: Layout of the FMS lead glasses

The FMS is a full absorption calorimeter in that the lead glass itself acts as both an absorber and an active element generating signals. Due to the addition of heavy elements such as Pb the transparent glasses of large and small cells both have approximately $18X_0$ radiation length in depth. Electromagnetic showers of electrons, positrons and photons are initiated and almost fully contained within the glass. The index of refraction of the glass is about 1.67. The Cherenkov radiation generated by the secondary particles in the showers will be directed towards the end of the glass and collected by Photo-Multiplier Tubes, the optical photons from the radiation arriving at the PMTs form the signal of the detector. Each single cell is wrapped by $10\mu m$ aluminized mylar to provide optical isolation. The optical properties of the small cells as well as the quantum efficiencies of the cathode of PMTs have been studied in [52]. These properties are implemented for both small and large cells in the

simulation with slight modifications which will be discussed in the next chapter. As a result the photon-electron yield per unit energy deposit in the glass is estimated to be around 1000 $p.e./GeV$ for large cells and 700 $p.e./GeV$ for small cells, including effects such as absorption by the glass and loss at glass/mylar surface reflections during light propagation, and limited quantum efficiencies of PMT cathodes. Notice that these light yield is smaller than that of typical scintillator-based active volumes (a few thousands $p.e./GeV$), mostly due to the inherent properties of Cherenkov light production. But the advantage of using Cherenkov light as the calorimeter signal is that it is generated much faster than scintillating light [53] so that the signal integration time at the Front-End Electronics can be very short, typically about 20 ns, which allows the calorimeter to be operated at a much faster read-out speed. The short integration time also helps discriminating electron/photon against hadron since the nuclear processes involved in hadronic showering (such as nucleus spallation, neutron evaporation) happen much slower than the Cherenkov light production by fast-traveling electrons and positrons. The difference in the time structure of signals can be utilized to enhance the discrimination power.

The FMS was initially installed in STAR in 2008 with slightly different configuration (and was called FPD++). In 2013 it was demonstrated that the lead glasses had experienced serious radiation damages and refurbishment work was performed to get the detector ready for the year 2015 running. The major task was to unstack the lead glasses and treat them by exposing to sunlight, so that the ultraviolet radiations in natural sunlight would cure the gray spots in the glass. Figure 2.9 shows a few lead glasses before and after a 40-hour annealing process. Figure 2.10 shows a quantitative comparison of the lead glass transmittance before and after UV treatment, measured at three difference locations along the glass using a deuterium lamp. The average transmittance for $\lambda > 900nm$ is normalized to be 1.

In addition to curing the radiation damages in the lead glass the PMT bases of all of the large cells have been replaced by the resistive bases acquired from Fermilab, a few hundred of the small cell PMT bases have been repaired as well. At the time of this writing the FMS is fully restacked and has been taking data for the 2015 proton-proton and proton-Au collisions.

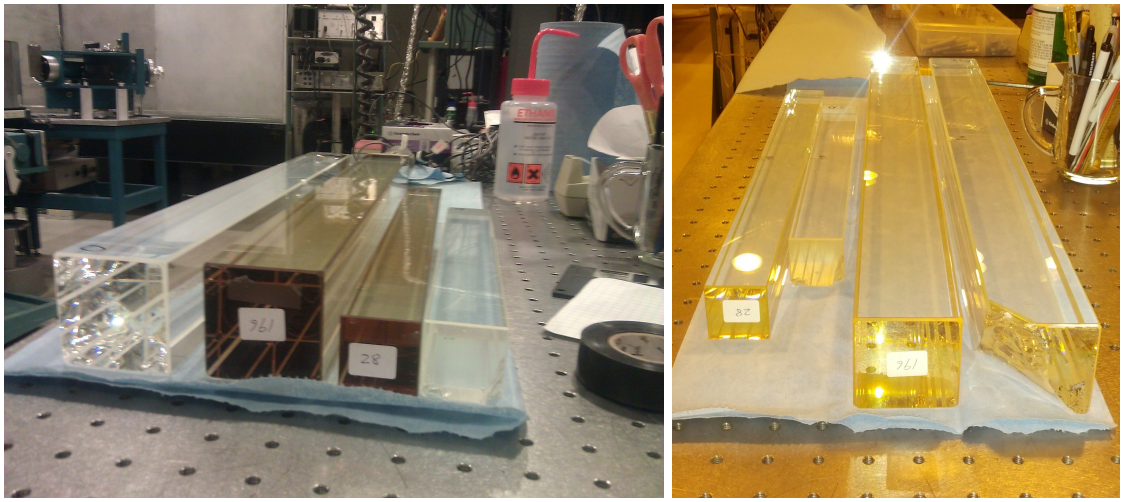

Figure 2.9: Left: FMS lead glasses before UV treatment. Right: The same lead glasses after UV treatment

The response of FMS lead glasses to high energy particles produced in the collisions as well as the propagation of Cherenkov photons inside the glasses are model by the GEANT detector simulations, for which the main purpose is to understand the detailed composition of signal and background seen in the data so that the asymmetries of the π^0 signal can be extracted. The details of modeling the FMS in simulation will be discussed in the next chapter as an important step of the analysis.

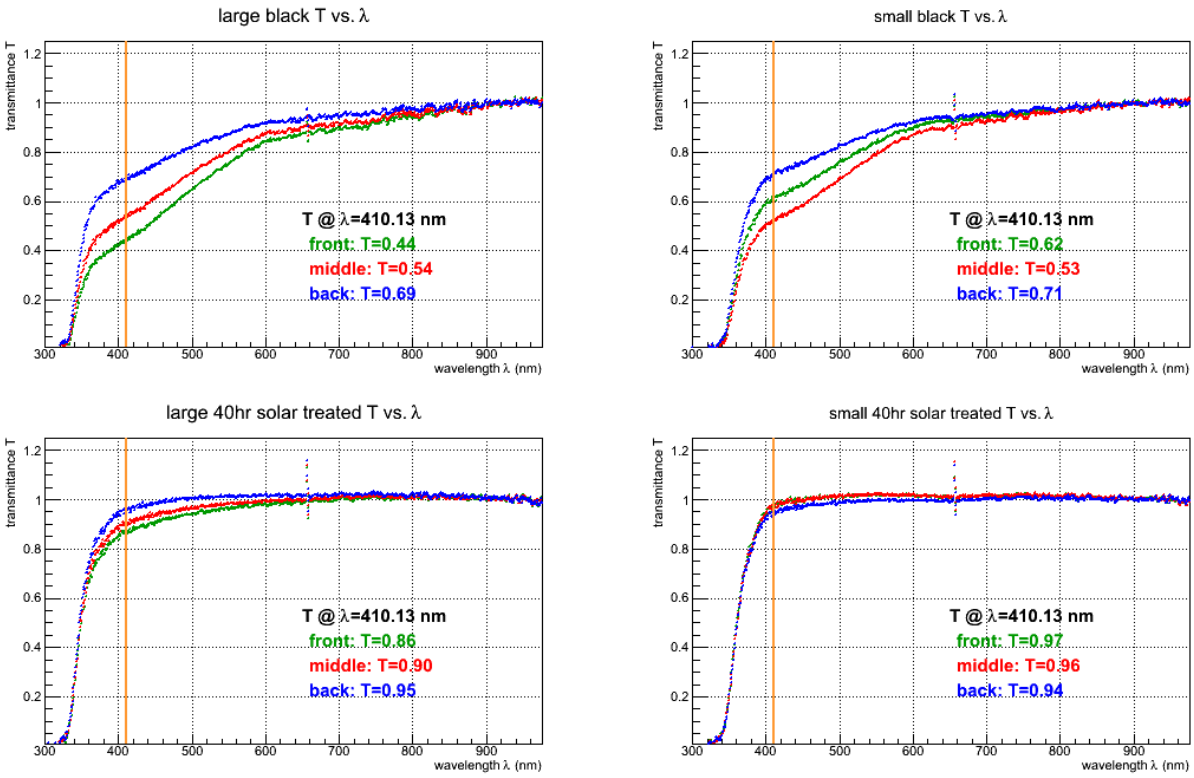

Figure 2.10: Top: Transmittance of small and large cells before UV treatment. Bottom: Transmittance of the same small and large cells after UV treatment

CHAPTER 3

Analysis

This chapter describes the details of the data collection and processing procedure. The main focus is the analysis methodology for π^0 asymmetry extraction. Before computing physics quantities, the raw data usually needs to go through several preprocessing steps including data sanity checks, transformation and reconstruction of features representing physical objects such as photons or their parent particles in the decay chain, and understanding of signals and backgrounds.

3.1 Triggers and Dataset

Most inelastic proton-proton collisions are not of interest to general physics analysis. For example the total inelastic cross-section of proton-proton scatterings at $\sqrt{s} = 500$ GeV is about 45 mb [54], while those producing a π^0 with $p_T = 2$ GeV at pseudorapidity $\eta = 3.7$ has a cross-section of only about 10 μb. The three orders of magnitude difference means it would be very inefficient to record each inelastic scattering event if we are only interested in those containing π^0 at forward rapidities with relatively high p_T. To that end a group of hardware trigger logics [55] has been implemented using the electronic signals readout from the FMS. These are called the STAR Level-0 triggers. The Level-0 triggers scan fast detector outputs for every bunch crossing in RHIC at 9.3 MHz and are supposed to issue a decision within 1.5 μs. For the FMS branch the depth of the hardware trigger logic is three-fold. The logic modules (DSM boards) at first layer directly operate on the sums of FMS channel signals over a local area, the second and third layers in turn work with their previous layer and form their outputs to the next layer. Finally the output of the third layer is fed into the

STAR global Trigger Control Unit–the TCU, which decides whether to accept the event or not. Figure 3.1 shows the organization of the layer-0 trigger patches on FMS channels.

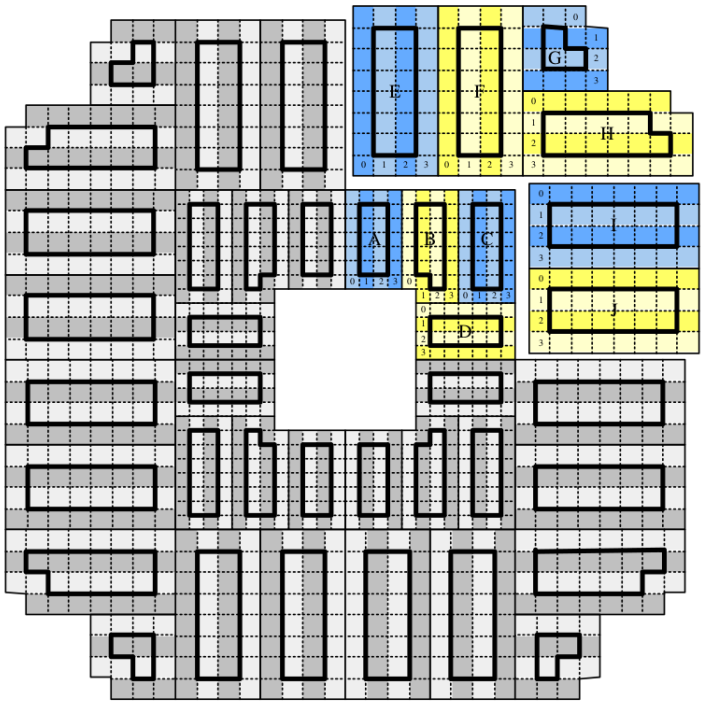

Figure 3.1: Layout FMS channel to layer-0 DSM board assignment scheme

The amplitude of the digitized electronic signals (ADC) of a group of FMS channels are summed up and fed into the layer-0 Data Storage and Manipulation (DSM) boards. There are four groups of channels involved for each individual layer-0 DSM board (board A, B, C, etc.). They are colored differently in blue and yellow and are given numerical labels (0, 1, 2, 3). Each DSM board takes as input the sum of channel ADCs within each one of the four groups and calculates the board sums from them. The board sum of each layer-0 DSM is then fed into one of the layer-1 DSMs which in turn calculates the total of several board sums, e.g over board A-B-C-D. Finally the layer-2 DSM computes the total of all boards from the same detector quadrant. The assignment of detector channels to layer-0 DSM boards as shown in Figure 3.1 applies to the other three quadrants in the same way. The final trigger definitions are built on top of the ADCs of single channels, DSM board sums and layer-2 quadrant sums. For example the simplest FMS trigger is a high tower trigger that requires the ADC of at least one FMS channel to be above a certain threshold. Board

sum trigger selects events based on energies deposited on a group of adjacent cells, which is geometrically more closely related to the electromagnetic showers initiated by photons and electrons. The quadrant sum or jet-patch trigger selects more diffused structures similar to the activities generated by jets. In practice different FMS triggers may fire at vastly different rates depending on their thresholds and topological configurations. To efficiently utilize the bandwidth of the data acquisition system (DAQ) these triggers are usually pre-scaled in different ways. A pre-scaling factor of N refers to the strategy of taking every other N event satisfying a certain trigger type instead of recording all of them. In this way one can allocate more bandwidth to the rare but interesting events.

In the actual data-taking process, the FMS triggers usually have to be working together with other triggers which are not directly related to the FMS physics program. To accommodate the goal of each trigger and not to interfere with other physics programs, decisions have to be made before the start of the Run in terms of the pre-scale factors (or allocated rate) for each trigger as well as detectors involved in the trigger definitions. For example in the 2011 running period almost all of the FMS-related triggers did not require reading out the TPC. Therefore the rates of these triggers are not limited by the 1.5 KHz rate of the TPC readout. In special run configurations where only FMS triggers are included the DAQ systems can run at $\sim$ 3 KHz, allowing more events to be taken due to the small event data size for FMS-only triggers.

The dataset used for the analyses presented in this document is from the year 2011 running period with transversely polarized proton proton collisions at $\sqrt{s} = 500$ GeV. The set of triggers generated this dataset includes the FMS low- and high-threshold jet-patch triggers (JP1 and JP2), board-sum triggers on large cells (LgBS1 and LgBS2) and board-sum triggers on small cells (SmBS1 and SmBS2). There are 375 million triggered events in total recorded with an average polarization of 52.3%. The main detectors involved are all calorimeters–FMS, BEMC and EEMC.

3.2 Data Quality Assurance

The entire data-taking period is broken up into a few hundred short runs, each lasting no more than 2 hours. The goal of data quality assurance (QA) is to make sure that the detector was functioning properly and to remove outliers of the runs or malfunctioned regions of the detector. These outliers could potentially corrupt the data or even lead to false conclusions in the physics analysis.

The first stage in data quality assurance is online monitoring, namely examining the diagnostic plots and trigger rates as the data comes in and make prompt adjustments as soon as something goes wrong. For example Figure 3.2 shows two examples of online trigger monitoring plots. The one on the left panel is DAQ rate *vs* time for a healthy run where the rate is stabilized at around 1 KHz. The right panel shows a run suffering from 'trigger run-away' problem towards the end, caused by stuck bits in the FMS DSM board output logics. The stuck bits forced the trigger logic to be always at ON state which caused the DAQ system to run at its highest rate of ∼3 KHz, recording nothing but useless uninteresting events. This is where the shift crew had spotted the problem and terminated the run.

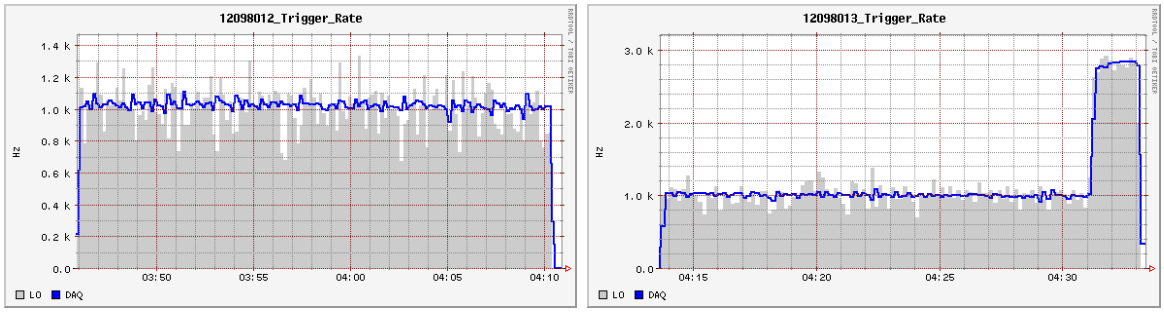

Figure 3.2: Left: DAQ rate *vs* time for a healthy run. Right: Another run that suffers from a FMS trigger run-away problem.

At the same time there are also L0-trigger diagnostic plots generated right after each run which help experts evaluate DSM board performances. For the offline analysis, any run having the trigger problem as shown on the right panel of Figure 3.2 is excluded. The equivalent luminosity after online QA is $22pb^{-1}$.

The offline data QA consists of evaluating the detector performance with reconstructed physical objects such as clusters and photons, as well as masking out malfunctioned regions on the detector instead of discarding the whole event. The procedure of removing malfunctioned regions begins with generating a run-by-run hot tower list. A hot tower refers to the tower/cell of the calorimeter that has way more number of hits above a certain energy threshold than the average over the entire detector. This is usually caused by mis-calibration or time-dependent gain shifts. These hot towers needs to be removed from reconstruction otherwise the combined effect of mis-calibration and a high occupancy will distort the detector acceptances and report incorrect energy scales. The procedure of generating the list is as follows: First the number of hits with energies falling in 6 different bins are accumulated for each tower on each day, the energy bins used in this analysis are (0,10),(10,40), (40,60), (60,80), (80,100), and geq100 GeV. Then the hot towers in each energy bin were identified by an iterative procedure. In each iteration the hottest tower with more than 10 times the averaged count is removed. The average count is re-calculated from the remaining non-zero towers. The iteration stops when none of the towers has more than 10 times the average number of hits. Figure 3.3 shows an example of the list of hot towers identified from the 40 GeV to 60 GeV range.

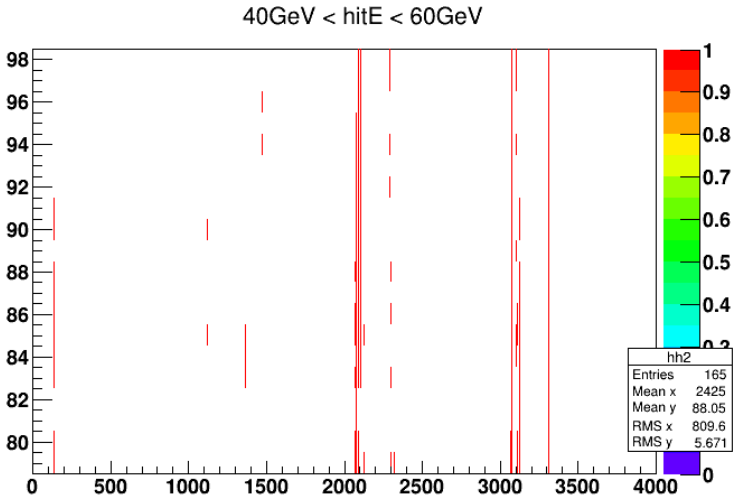

Figure 3.3: FMS hot tower list identified in the 40 GeV to 60 GeV energy bin. X-axis: tower id. Y-axis: day number

The above procedure is effective at identifying hot towers. Figure 3.4 shows the number of hit distributions for energies within (10, 100) GeV before and after hot tower removal.

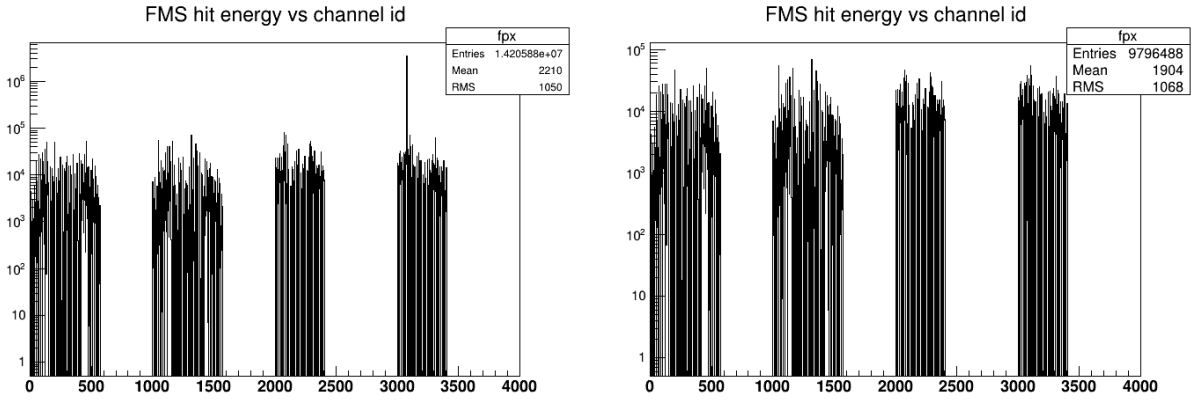

Figure 3.4: Left: FMS tower occupancies before hot tower removal. Right: After hot tower removal. The hit energy range is (10, 100) GeV

With the hot towers removed, a run-by-run offline QA was conducted using reconstructed objects such as clusters and photons. These are high level physical observables directly related to π^0 reconstruction and asymmetries measurements. The offline QA verifies that all reconstructed variables have reasonable distributions over time. Figure 3.5 shows an example of the FMS cluster and photon QA for all of the runs taken in a single day.

3.3 γ/π^0 reconstruction

π^0 candidates are reconstructed through their 2-photon decay channel $\pi^0 \to \gamma\gamma$. Photons are the most basic physical units to be reconstructed from the FMS in order to build up higher level objects such as π^0 and jets. Photons initiate electromagnetic showers in the lead glass array which generate Cherenkov light that is subsequently collected by the PMTs. By grouping together the energies of several contiguous cells one can expect to reconstruct the energy of the primary photon. The procedure of converting electronic signals (ADCs) to energy is called calibration and will be discussed in later part of this chapter. The position of the photon on the detector is another piece of equally important information. A straightforward way of measuring the photon's position is to approximate it by the energy-

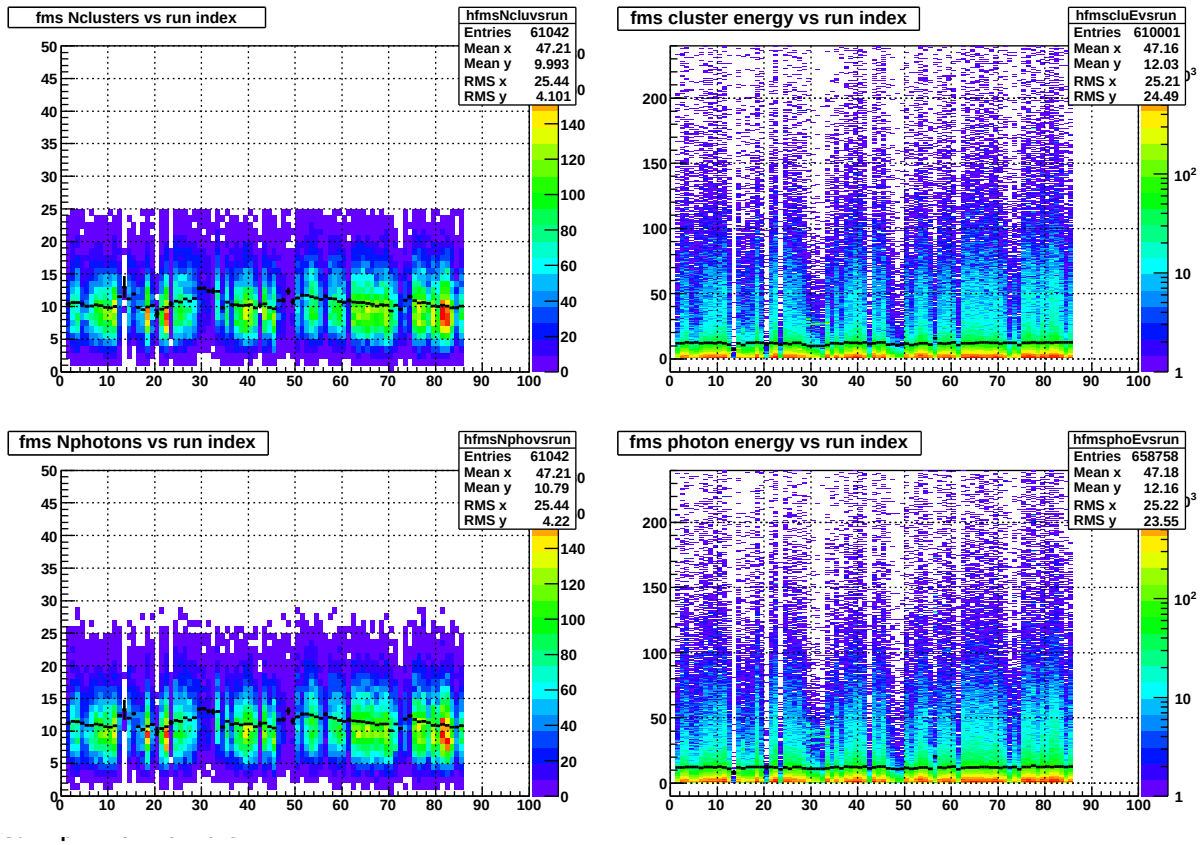

Figure 3.5: FMS cluster and photon QA. X-axis is the relative run index. Top Left: number of reconstructed clusters, capped at 25. Top Right: cluster energy. Bottom Left: number of photons. Bottom Right: photon energy. Black line indicates the average.

weighted centroid of all of the towers within the group which, at this point, is referred to as a cluster. More advanced methods include a sophisticated weighting scheme, or by utilizing the shower shape information to get a more accurate estimate. To reconstruct π^0 candidates one can simply pair up two photons and use the following relativistic relation to calculate the pair mass.

$$\begin{aligned} M_{\gamma\gamma} &= \sqrt{2E_{\gamma 1}E_{\gamma 2}(1-\cos(\theta_{\gamma\gamma}))} \\ &= 2\sqrt{E_{\gamma 1}E_{\gamma 2}}\sin(\frac{\theta_{\gamma\gamma}}{2}) \\ &= E_{\gamma 1,2}\sqrt{1-Z_{\gamma\gamma}^2}\sin(\frac{\theta_{\gamma\gamma}}{2}) \\ &\approx E_{\gamma 1,2}\sqrt{1-Z_{\gamma\gamma}^2}\frac{D_{\gamma\gamma}}{2Z_d} \end{aligned} \tag{3.1}$$

where $E_{\gamma 1}$ and $E_{\gamma 2}$ are the energies of each individual photon, $E_{\gamma 1,2}$ is the energy of the photon pair, $Z_{\gamma\gamma}$ is the energy sharing between the photon pair $Z_{\gamma\gamma} = |E_{\gamma 1} - E_{\gamma 2}|/E_{\gamma 1,2}$, $\theta_{\gamma\gamma}$ is the opening angle of the photons pair which can be approximated by the distance between them on detector $D_{\gamma\gamma}$ divided by the distance from the collision vertex to the detector plane (or shower maximum) Z_d. In practice the task of γ/π^0 reconstruction is to evaluate ($E_{\gamma 1,2}$, $Z_{\gamma\gamma}$, $D_{\gamma\gamma}$) from the signatures of the electromagnetic showers left by the photons. The next few subsections will describe each step in detail.

3.3.1 Tower clustering algorithm

In the first step of the photon reconstruction the adjacent towers are grouped together by a clustering algorithm based on energies deposited in the towers. A tower with non-zero energy deposit is called a hit. The clustering algorithm is described in [56] and the details can be found therein. The main workflow of the algorithm is as follows:

1) Towers are categorized as 'seed' towers or 'neighbor' towers according to how their energies compare to their closest neighbors. If the tower energy is the highest among these neighbors it is moved to the seed tower list, meanwhile its neighbors are moved to the neighbor tower list. Otherwise the tower in question is moved to the neighbor tower list.

After looping over all non-zero towers, one ends up with two arrays, the seed tower array contains the towers around which clusters will be gradually generated and the neighbor tower array has the towers that will be associated with existing clusters.

2) Towers in the seed array are taken as initial 1-tower clusters. Those in the neighbor array are added to the nearest clusters based on their distances to the seed tower. If there is an ambiguity, e.g. distance to two or more seed towers are the same, the assignment is deferred and the neighbor tower in question is added to a new array called the 'valley' array which contains all the towers with ambiguous cluster assignment.

3) When all neighbor towers are either added to the existing clusters or to the valley array the energy weighted centroid of each cluster is calculated as follows

$$x_{clu} = \frac{\sum_{i \in clu} ln(E_i + E_{offset}) x_i}{\sum_{i \in clu} ln(E_i + E_{offset})}$$
$$y_{clu} = \frac{\sum_{i \in clu} ln(E_i + E_{offset}) y_i}{\sum_{i \in clu} ln(E_i + E_{offset})} \tag{3.2}$$

where E_{offset} is set to 0.5 GeV. Any tower with $ln(E_i + E_{offset}) < 0$ is excluded from the sum. Therefore $1 - E_{offset}$ serves as a low energy cutoff which for this case is 0.5 GeV. The energy weighted cluster centers are used to compute more accurate distances to the towers in the valley array. The valley towers are assigned to the closest cluster based on this metric.

4) If there are still ambiguous towers left in the valley array they are assigned to the cluster that has the highest energy among the candidates. This step typically exhausts the valley array after which all towers will be associated to a cluster. Finally the cluster centroids are recalculated and the variance or second moments of the clusters are computed as follows

$$\sigma_x^2 = \frac{\sum_i ln(E_i + E_{offset})(x_i - x_{clu})^2}{\sum_i ln(E_i + E_{offset})}$$

$$\sigma_y^2 = \frac{\sum_i ln(E_i + E_{offset})(y_i - y_{clu})^2}{\sum_i ln(E_i + E_{offset})} \tag{3.3}$$

$$\sigma_{xy}^2 = \sigma_{yx}^2 = \frac{\sum_i ln(E_i + E_{offset})(x_i - x_{clu})(y_i - y_{clu})}{\sum_i ln(E_i + E_{offset})}$$

Compared to linear energy weighting the log-energy weighting has the advantage of being insensitive to the cluster topologies, namely whether the center of the cluster is close to a tower center or to the tower boundaries does not affect the cluster moments as much as that with linear weighting.

3.3.2 Cluster categorization

Photons from high energy π^0 decays are usually traveling very close to each other, such that their electromagnetic showers in the calorimeter overlap. At higher energies there is an increased probability that the clusters found on the detector are actually generated by two photons, so a decision has to made to categorize the photon content of a cluster. For this analysis only 1-photon and 2-photon clusters are considered. Clusters having more than 2 overlapping photons are rare.

Clusters are classified in a 2-step procedure. The first step is based on a Principal Component Analysis (PCA) of the 2-dimensional cluster shape. PCA tries to find important directions of variation in the dataset instead of using the original coordinate system for data representation. For example in PCA the first principal component is the direction along which the data has the largest variance, the second principal component is the one that has the largest variance among all the directions orthogonal to the first principal component. For the 2-dimensional cluster distribution there are only two principal components, denoted by σ_{max} and σ_{min} respectively. Figure 3.6 shows the distribution of the cluster energy *vs* the product of σ_{max} and cluster energy for small and large cells derived from data. The cluster

moment-based categorization is based on these distributions.

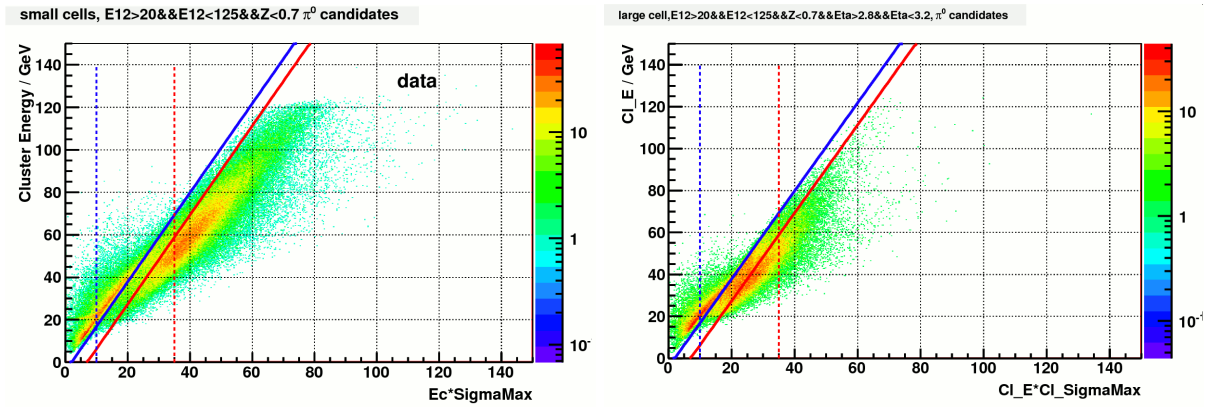

Figure 3.6: Cluster energy *vs* SigmaMax times Cluster energy in data. Left: Small cells Right: Large cells.

If the cluster signature falls to the left of the dashed blue line and above the solid blue line it is categorized as a 1-photon cluster. If it falls to the right of the dashed red line and below the solid red line it is considered to be a 2-photon cluster. Any other regions are considered as ambiguous and the actual class label will be determined in the second step. Figure 3.7 shows the same distributions in GEANT detector simulations for 40 GeV single photons and daughter photons of 40 GeV π^0.

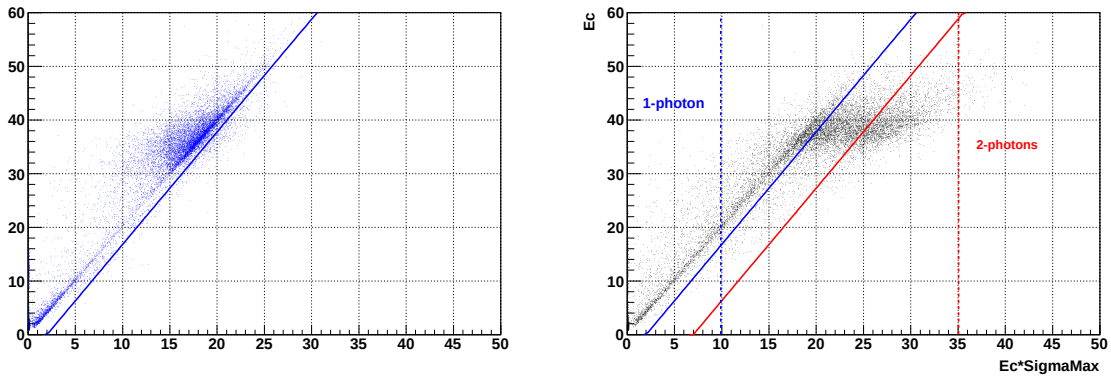

Figure 3.7: Cluster energy *vs* SigmaMax times Cluster energy in simulation. Left: 40 GeV single photons Right: Daughter photons of 40 GeV π^0

Comparing these two plots one can clearly see how the classification should be made. Details of the simulation setup will be discussed in later part of this chapter. The decision

for ambiguous clusters will be deferred to the second step when the clusters are fit to a shower shape with 1-photon and 2-photon assumptions. The model that fits the cluster shape better determines the photon content of the cluster.

3.3.3 Fitting to the shower shape

The shape of the cluster contains much more information than its centroid and second order moments. An accurately parameterized shower shape function could aid to the cluster categorization as well as getting better estimate on the position of the photon. To this end the differential shower shape has been proposed to have the following form [52] [57]

$$\begin{aligned} f(x,y) =& \sum_{i=1}^{3} a_i f_i(x,y) \\ f_i(x,y) =& \frac{1}{2\pi}\left[\frac{1}{1+\left(\frac{x}{b_i}\right)^2+\left(\frac{y}{b_i}\right)^2}\right]^{\frac{3}{2}} \end{aligned} \tag{3.4}$$

where $f(x,y)$dxdy represents the fraction of the photon's energy deposited in an area of $\mathrm{dx}\cdot\mathrm{dy}$ located at position (x,y) when the origin of the coordinate system is on the photon itself. The differential shower shape is made up of a linear combination of three pieces each has a form of $\frac{1}{1+r^2}^{\frac{3}{2}}$. Figure 3.8 shows the 2-dimensional differential shower function as well as its cross-sectional shape at y = 0.

To obtain the observed shower shape, which represents the fraction of the photon energy deposited on a tower, one needs to integrate the differential shower shape over the dimensions of a tower. From eq. 3.4 one can obtain the integrated shower shape as follows

$$\begin{aligned} G(x,y) =& F(x+\frac{d}{2},y+\frac{d}{2}) - F(x-\frac{d}{2},y+\frac{d}{2}) - F(x+\frac{d}{2},y-\frac{d}{2}) + F(x-\frac{d}{2},y-\frac{d}{2}) \\ F(x,y) =& \frac{1}{2\pi}\sum_{i=1}^{3} a_i \left[\arctan\left(\frac{x}{b_i}\right) + \arctan\left(\frac{y}{b_i}\right) + \arctan\left(\frac{xy}{b_i\sqrt{b_i^2+x^2+y^2}}\right)\right] \end{aligned} \tag{3.5}$$

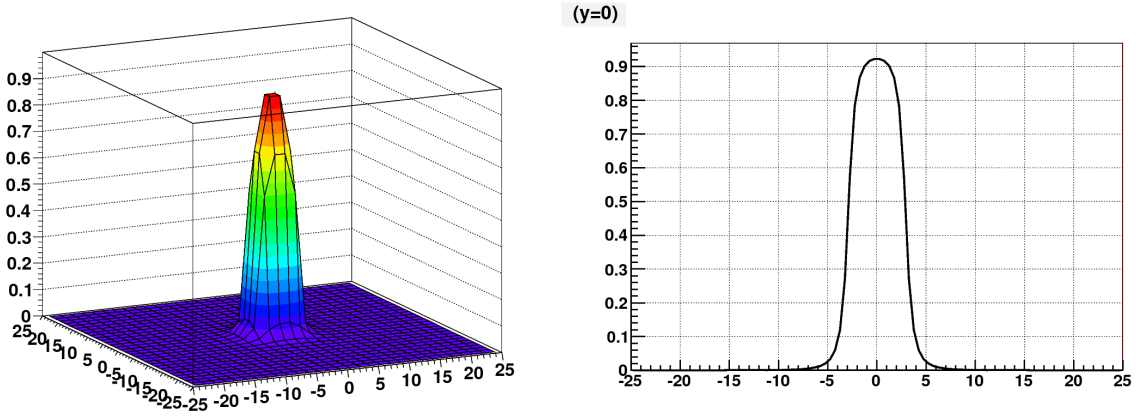

Figure 3.8: Differential shower shapes

Shower shape measurements are important for both data analysis and Monte Carlo simulations. As will be discussed later, the uncertainties in the energy scales of the final results are estimated through the difference in reconstructed π^0 mass between simulation and data. For that strategy to work one has to understand other non-energy related variables that play a role in computing π^0 masses, e.g. $D_{\gamma\gamma}$ which is calculated from photon positions from shower fitting. The photon shower shapes in data has been studied in [57] [58]. Here the focus is to studying the shower shape in simulation and incorporating the incident angle effect.

Although the FMS is placed at about 7 meters away from the interaction point, due to its considerable size the incident angle at the outer perimeter of the detector could be as large as 8 degrees. Combined with the non-projective geometry of the towers, the observed shower shape is not strictly transverse and depends on the incident angle. In other words the centroid of the transverse shower profile is going to be shifted outwards as the shower develops inside the lead glass. This effect has been observed in both data and simulation. Figure 3.9 shows where the shower shape is measured in simulation.

The basic symmetric shower shape without incident angle effect is studied first since the asymmetric version that accounts for incident angle effect will be built upon them. For that purpose 40 GeV single photons are generated in simulation and those that fall in the blue area in Figure 3.9 are used to measure the shower shape. In practice the transverse shower

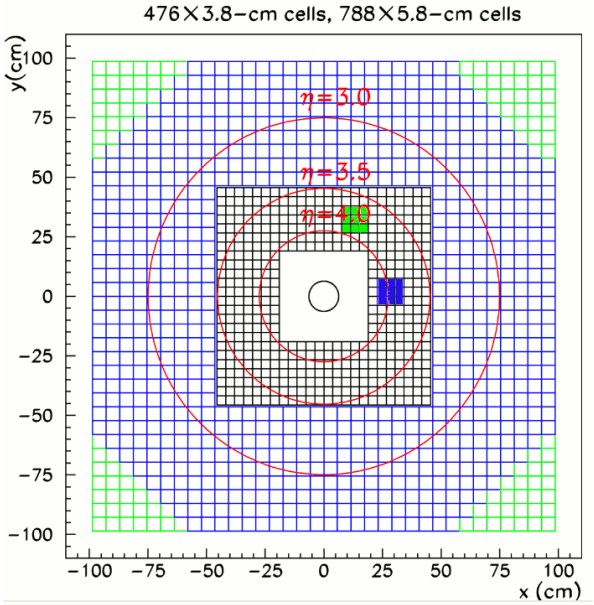

Figure 3.9: Regions on the detector where the shower shape is measured. Compared to the green area the vertical shower shape in the blue area does not suffer from incident angle effect since it is closer to the X-axis

shapes are found to be almost energy-independent [53] since it is dominated by the Cherenkov radiations of $\sim$ MeV particles at the shower maximum. The blue region is chosen since it is close to the horizontal axis, in this location the shower development in the vertical direction does not exhibit incident angle effect while in the transverse direction it does. Figure 3.10 shows the y $\sim$ 0 intersection of the vertical shower shape using towers on the same column as the central tower being hit by the photon. A set of the shower parameters (a's and b's) are obtained by the TMinuit minimization routine.

The shower parameters obtained from the fit are shown in Table 3.1. Note that the a's need to be normalized to 1 before being compared to the previous results or applied to the actual reconstruction. Notice that all of the parameters can be fixed just by measuring the shape at the y $\sim$ 0 intersection since the 2-dimensional shower function is symmetric around its central axis.

Figure 3.11 shows the comparison between shower shapes in simulation (black points) and that in data (dashed blue line). The data shower shape is slightly wider in the hip area.

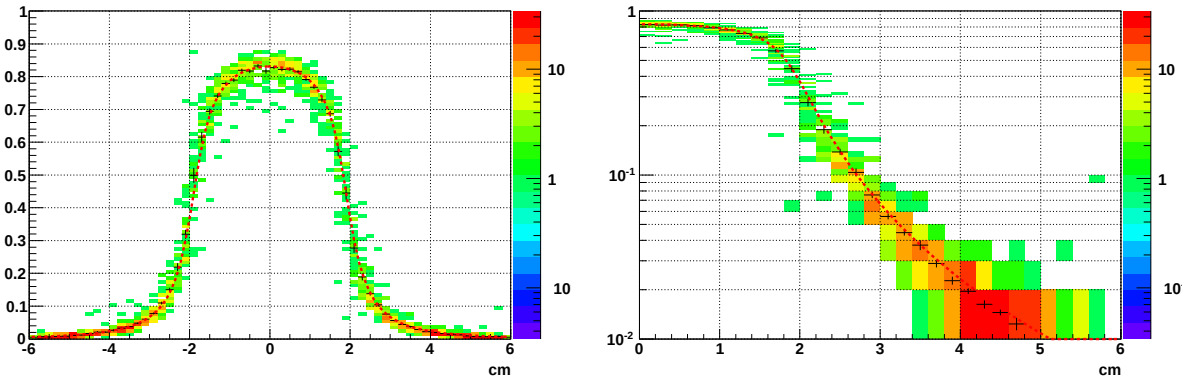

Figure 3.10: Left: Vertical shower shape measured in the blue area. Right: Log-scale zoom in on the tails

a_1	a_2	a_3	b_1	b_2	b_3
1.06841	0.150087	-0.171292	0.37491	0.860969	0.386676

Table 3.1: parameters of the symmetric shower shape

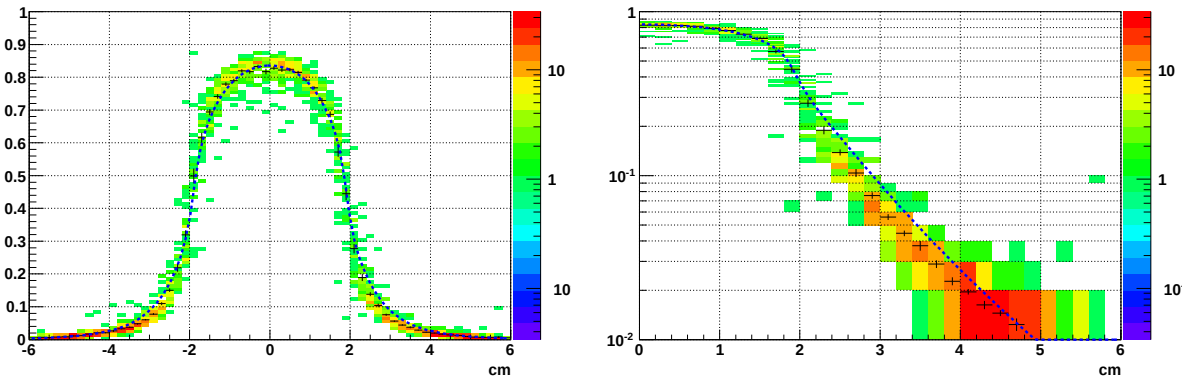

Figure 3.11: Left: comparing symmetric shower shape in data (dashed blue line) and simulation (black points). Right: Log-scale zooming in on the tails

The incident angle effect can be easily seen in the transverse shower shape obtained from the same group of cells in the blue region. This time only the cells on the same row as the central cell are included, as shown in Figure 3.12.

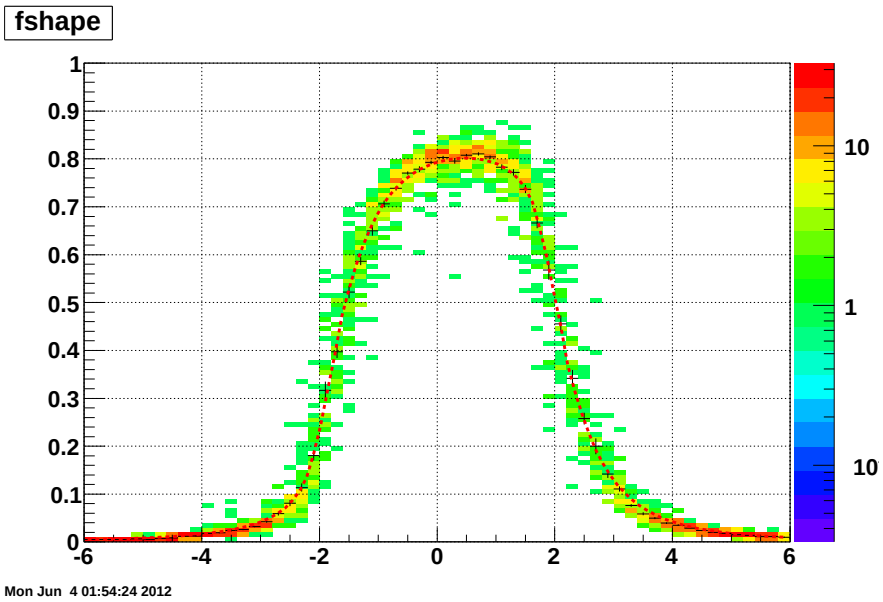

Figure 3.12: Horizontal shower shape fitted by an asymmetric shower function incorporating incident angle effect.

The transverse shower shape can be nicely fit by an asymmetric shower function obtained through the following procedure. Basically, when an incident angle is involved, the shower shape that is seen at the transverse detector plane is a projection of the 3D shower distribution, with its longitudinal component mixed in to the transverse profile. Therefore the most exact way to describe this type of shower shape would be having a differential 2D shower function $T(x(z), y(z))$ convoluted with the longitudinal shower development G(z), so that the final shower function can be written as

$$f(x,y) = \int T(x - x_c(z), y - y_c(z)) \cdot G(z)\mathrm{d}z \tag{3.6}$$

But in practice the exact form of the differential transverse shower function $T(x, y)$ at depth z can not be determined experimentally. $T(x(z), y(z))$ represents the transverse shower profile within an infinitesimal longitudinal z-slice. So the best thing one can do is to approximate the integral by a finite sum

$$f(x, y) = \sum_i g_i \cdot \hat{T}(x - x_{ci}(z_i), y - y_{ci}(z_i)), \tag{3.7}$$

where the overall shower distribution is split up into several z-slices, each with a finite thickness. The transverse shower profile of each slice $\hat{T}(x, y)$ can be measured in simulation by only accumulating Cherenkov photons generated within that slice. All the z-slices are then added up with a weighting factor g_i which approximates the longitudinal shower development. The weighing factors are proportional to the number of Cherenkov photons generated within each z-slice which have propagated to the photo-cathode of the PMT. The incident angle effect comes into the equation through the z-dependence of the shower center (x_{ci}, y_{ci}) of each slice

$$\begin{aligned} x_{ci} =& x_{cmax} + \tan\theta_x \cdot (z_{ci} - z_{cmax}) \\ y_{ci} =& y_{cmax} + \tan\theta_y \cdot (z_{ci} - z_{cmax}) \end{aligned} \tag{3.8}$$

in which (x_{cmax}, y_{cmax}) are the position of the shower center in the z-slice that has the highest weight, this coordinate will be reported as the position of the photon. In summary, (x_{cmax},y_{cmax}, $\tan\theta_x$, $\tan\theta_y$) are the variable parameters obtained from the fit during reconstruction. They can be initialized by the similar parameters from the cluster. To extract the weights and transverse shower shapes within each z-slice a procedure similar to the symmetric shower shape measurement in the vertical direction is conducted on the group of cells in the blue region, only this time the Cherenkov photons generated within a particular slice were counted and others are ignored. Figure 3.13 shows the group of shower shapes measured in 6 z-slices which are used to form the final incident angle dependent shower function.

It can be seen that as the shower progresses into the lead glass it becomes wider and wider. Figure 3.14 shows the distribution of Cherenkov photon yield within each slice as a

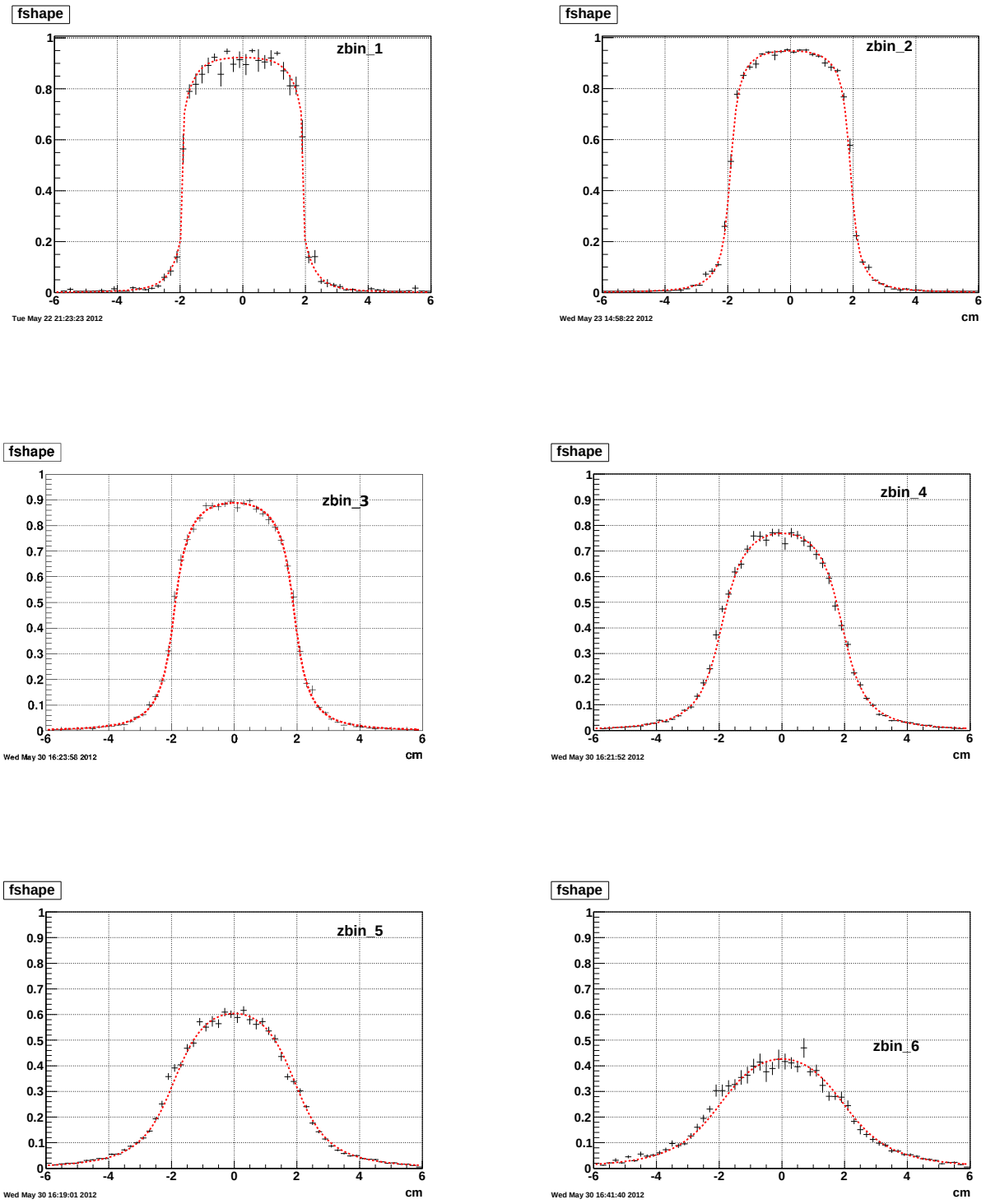

Figure 3.13: Transverse shower shape in different z-slices. $zbin_1$: (0, 7.5cm), $zbin_2$: (7.5cm, 15cm), $zbin_3$: (15cm, 22.5cm), $zbin_4$: (22.5cm, 30cm), $zbin_5$: (30cm, 37.5cm), $zbin_6$: (37.5cm, 45cm). All distances are measured from the front surface of the lead glass

fraction of the total yield. The mean of each distribution is used as the weight of each shower function $\hat{T}(x(z), y(z))$. In this plot the 3rd slice has the highest weight, therefore the shower center of the 3rd slice will be used as the (x_{cmax}, y_{cmax}) and reported as the reconstructed position of the photon.

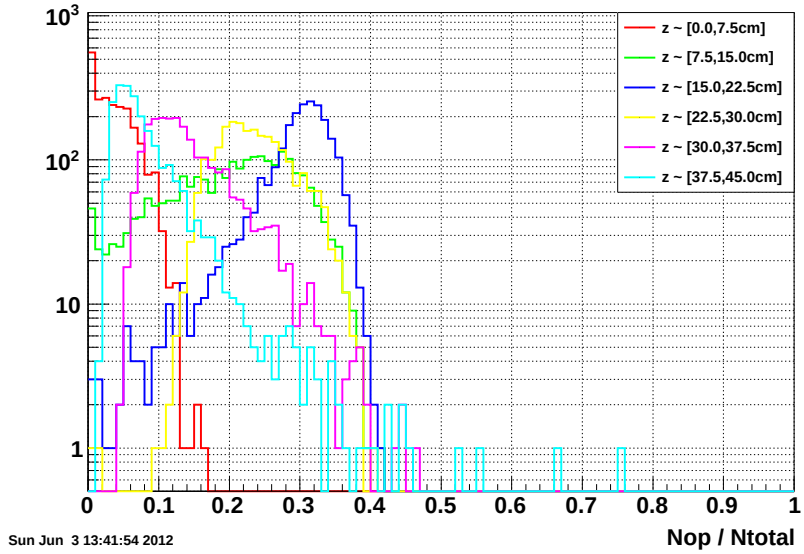

Figure 3.14: Cherenkov photon yield of each z-slice as a fraction of the total

Note that since the shower max position depends on the energy of the primary photon the weighting factors will have energy dependence too. An improvement of the current shower shape model would be a parameterization of the weights g_i in term of energy. For the current study constant weighting factors have been used which are derived from 40 GeV single photon simulations as shown in this case. The same asymmetric version of the shower function is used in both data and simulation. Reconstructed variables in data and simulation such as the two-photon separation $D_{\gamma\gamma}$ will be compared in larter part of this chapter.

3.3.4 Constructing π^0 candidates

π^0 candidates are constructed by finding all possible photon pairs, namely each reconstructed photon will be paired up with all other photons in the same event and their pair masses and total energies will be calculated. This procedure guarantees the inclusiveness from an experimental point of view and the result can be compared to theory calculations. Experimentally very asymmetric decays of π^0, e.g. those with $Z_{\gamma\gamma} \to 1$ will likely produce a photon out of the detector acceptance. So a $Z_{\gamma\gamma} < 0.8$ cut is applied to the photon pairs included in the final result. This cut also removes a large portion of the background pairs dominated by the abundant low energy photons. Figure 3.15 is an illustration of the reconstructed pair mass distribution from all of the data taken within a single day.

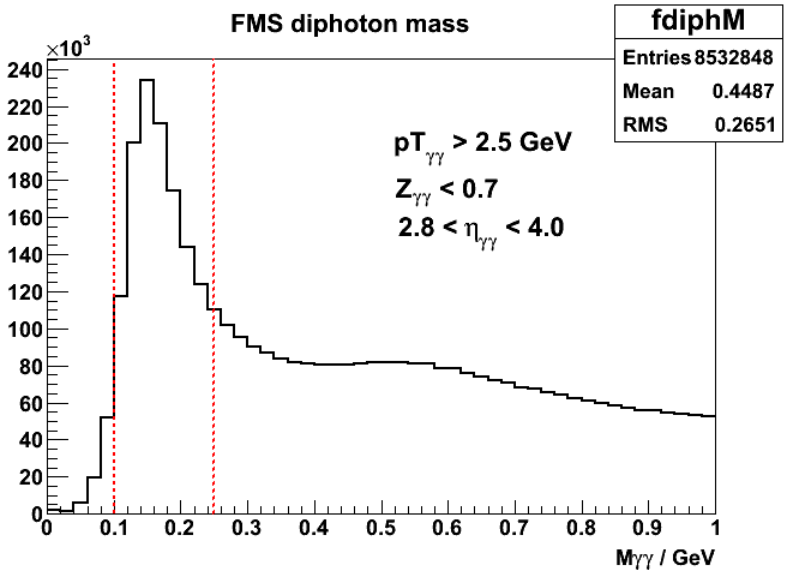

Figure 3.15: Mass distribution of photon pairs, data taken within a single day

3.4 Calibration

Calibration is the procedure of calculating gain constants of each PMT tubes such that the amplitudes of electronic signals (ADC) can be converted into energies for physical measurements. The calibration of the FMS are divided into two stages, online and offline. The goal of online calibration is to configure the detector such that it can maintain close to an ideal

gain setting where all of the channels participate in the trigger uniformly. The gain factors obtained from online calibration are used to update the high voltage for each channel in an iterative procedure to achieve almost the ideal setting. With the desired gain setting the entire detector system triggers with constant transverse energy E_T threshold.

The offline calibration are usually conducted after the data-taking. Its goal is to calculate the corrections of the gain factors of each channel on top relative to its ideal gain. This is done by collecting the reconstructed π^0 candidates associated with a specific cell (daughter photon having higher energy on the cell). Additional cuts on the π^0 candidate such as isolation requirements are applied to further reduce the background. The gain corrections are calculated as the ratio of nominal π^0 mass and the reconstructed mass from the sample associated with the cell. Details of the offline calibration can be found in [57]. During the run LED signals on each channel are activated at 1Hz and are taken with the LED trigger. The amplitude of LED signals serves as a gauge for keeping track of the gain drifting over time and has been used to make time-dependent gain corrections.

3.5 Simulation of the FMS responses

This section provides details on the FMS-related detector and physics simulations, which are essential in understanding the composition of the π^0 candidate samples as well as the uncertainties in their energy scales. The FMS simulation runs within the STAR GEANT3 simulation framework (GSTAR) which contains the geometry and material definitions of all existing STAR detector subsystems. The framework also facilitates adding new detectors for future upgrade studies. For most detectors as the particles traverse the sensitive volumes the energy deposit in each step (hit) along the trajectory is calculated. In the end the total energy deposit within the sensitive volumes of a single detector element is usually converted to ADCs by a simple parameterized function or a more realistic digitizer. However for FMS simulations it was found that the simple energy deposition model is not sufficient for describing the shower shapes [57]. Tracing the generated Cherenkov photons as they propagate through the glass and taking into account of effects such as light attenuation and

loss at surface reflections are needed for a better descriptions of the data.

3.5.1 FMS geometry setup

Figure 3.16 shows the front and top view of the FMS geometry in GSTAR, together with a 50 GeV single π^0 event.

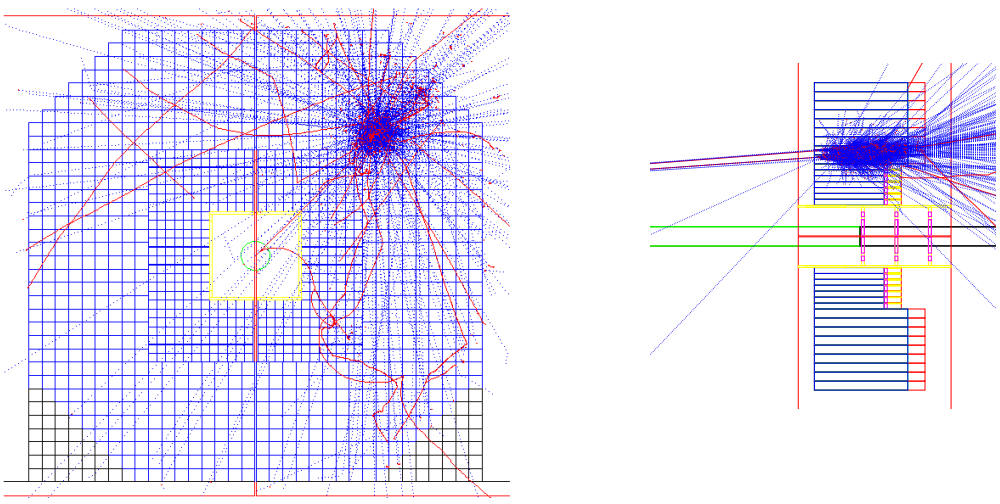

Figure 3.16: FMS geometry in GSTAR together with a 50 GeV single π^0 event

The lead glasses are wrapped with $10\mu m$ thick aluminized mylar. In order to compensate for the absence of total internal reflection at the glass-air boundary the reflection coefficient at the glass-mylar surface is increase by 7% [57] compared to what was measured in ref. [52]. Figure 3.17 shows the surface reflection coefficient and absorption length of the lead glass vs the energy of the optical photon. Note that uniform optical properties are used for all FMS lead glasses but in practice the radiation damages of each glass are not nearly the same. Some of the lead glass in the array are even made of radiation hard materials.

The diameter of the PMT photo-cathode is $51mm$ for large cells and $26.6mm$ on average for small cells. Figure 3.18 shows the efficiency of the photo-cathodes in converting photons to photo-electrons. Tracing optical photons as they propagate through the lead glass can be time-consuming. To speed up the simulation, the cathode efficiency is used to randomly remove optical photons when they are produced, instead of when they reach the photo-cathode at the end of the lead glass.

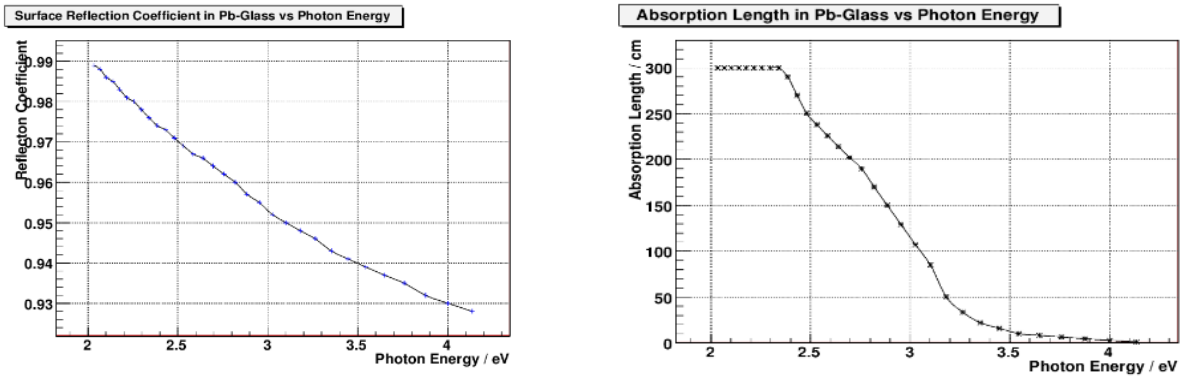

Figure 3.17: The surface reflection coefficient and absorption length of lead glass used in simulation

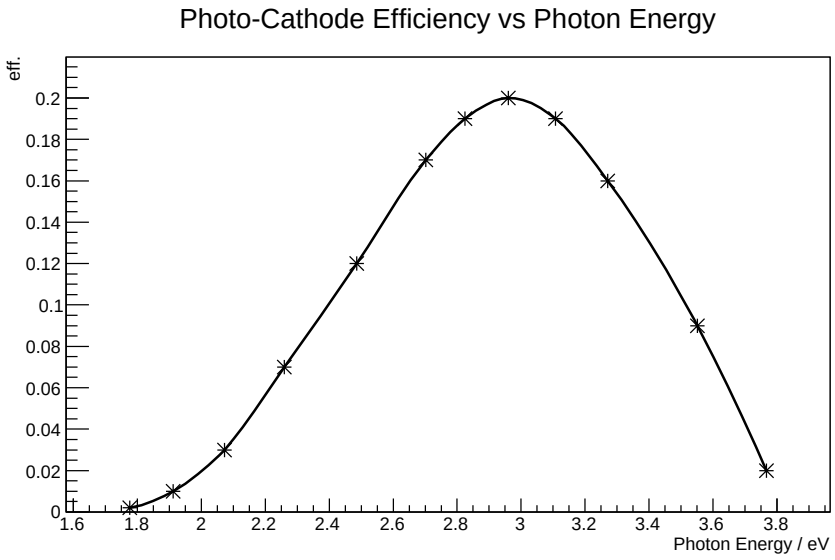

Figure 3.18: PMT photo-cathode efficiency used in simulation

3.5.2 Data simulation comparison

To generate proton-proton collision events in simulation the PYTHIA6 [59] event generator was used together with its TuneA configuration [60]. The width of the Gaussian distribution of the intrinsic parton transverse momentum k_T was set to 0.5 GeV/c in order to match previous STAR results on forward π^0 cross-sections [61] [62]. To enhance the statistics of high-p_T samples, the simulation set was separated into 5 partonic p_T bins, (2, 4), (4, 8), (8, 16), (16, 32) and (32, ∞) GeV, with 250K events generated for each bin. Then they are normalized to the same luminosity of $1pb^{-1}$. The calibration constants in the simulation are used to convert photo-electron counts to energies and are evaluated with the reconstructed π^0 masses at 25 GeV for the large cells and 40 GeV for small cells. These anchor points are the same in both data and simulation. There is a weak energy dependence for the calibration constants in simulation due to the light attenuation of the lead glass. Higher energy photons will initiate their showers deeper into the lead glass. Therefore the propagation length for the generated optical photons to reach the photo-cathode is shorter, incurring less light attenuation. In data due to the graying of the lead glass caused by radiation damage the attenuation effect is usually stronger and varies cell-by-cell. The energy-dependent gain shift is corrected by ensuring that the reconstructed mass of η mesons is constant over the energy range considered. η mesons are chosen for the task instead of π^0 mesons due to the larger opening angles of the daughter photons, therefore less systematic effects on the reconstructed pair mass from di-photon separation ($D_{\gamma\gamma}$) measurement compared to π^0. Figure 3.19 shows the ratio of reconstructed di-photon separation to generated for π^0 and η mesons from PYTHIA. The reconstructed photons are matched to daughter photons of π^0 or η based on the distance between them.

It can be seen that for π^0 at higher energies when the two daughter photons come closer to each other the reconstructed separation can be systematically larger than the true separation, whereas for η meson there is no such effect. In data this also partially accounts for the observed shift of reconstructed π^0 mass towards larger values at higher energy. But since this analysis is not about precisely measuring the π^0 mass, as long as the π^0 can be identified

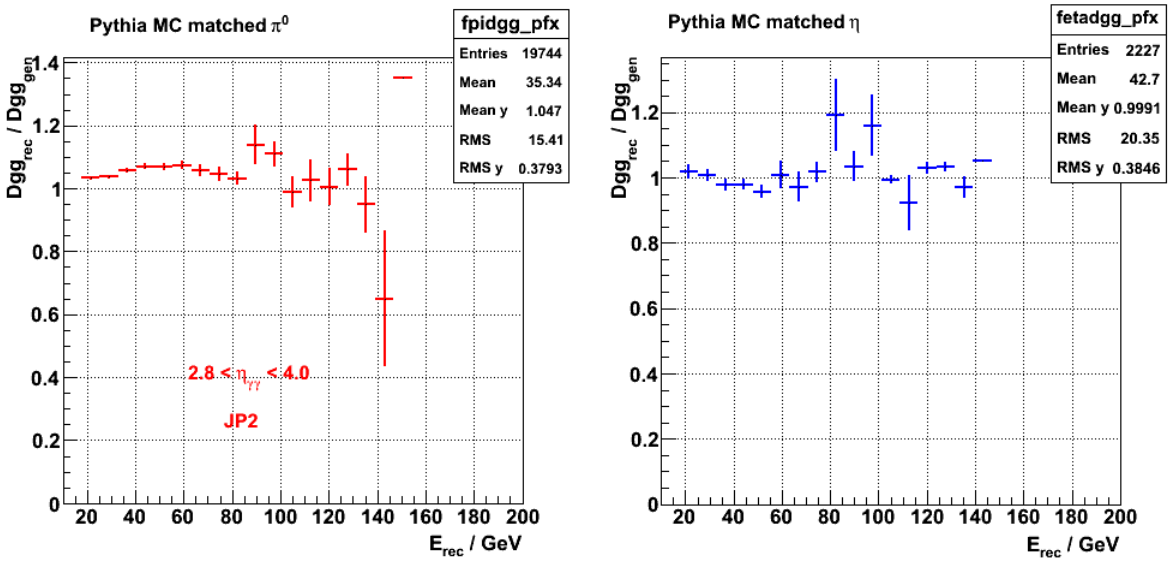

Figure 3.19: Ratio of reconstructed di-photon separation to generated. Left: π^0. Right: η

and its yield determined, one will be able to extract its production asymmetries. In order to see to what extent simulations can reproduce this effect in data, Figure 3.20 shows the comparison between the di-photon separation in the data and the simulation for photon pairs with mass $M_{\gamma\gamma} < 0.3$ GeV ($M_{\pi^0} = 0.135$ GeV) *vs* reconstructed pair energy. Figure 3.21 shows a similar comparison for photon pairs having 0.5 GeV $< M_{\gamma\gamma} < 0.8$ GeV ($M_{\eta} = 0.548$ GeV).

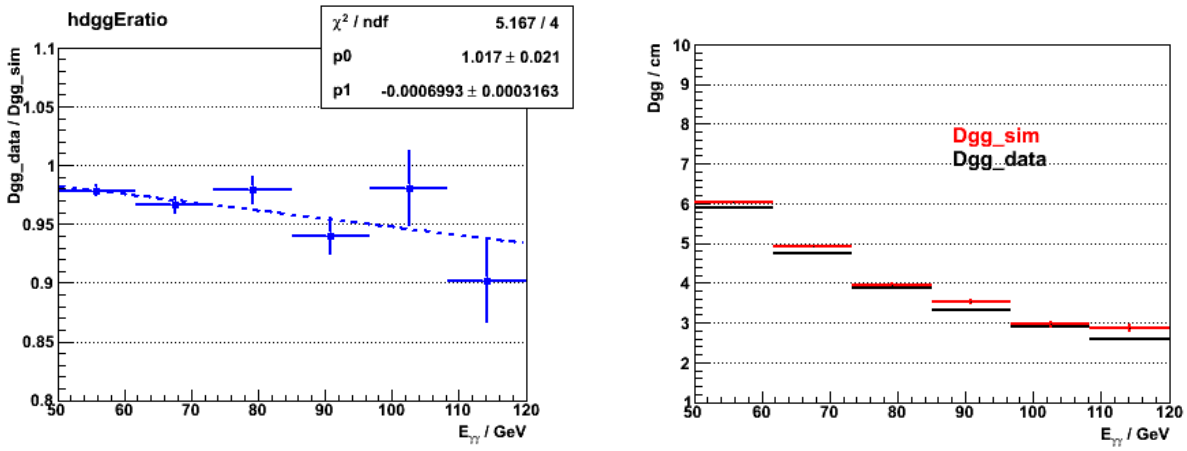

Figure 3.20: Di-photon separation *vs* pair energy in the data and the simulation, $M_{\gamma\gamma} <$ 0.3 GeV

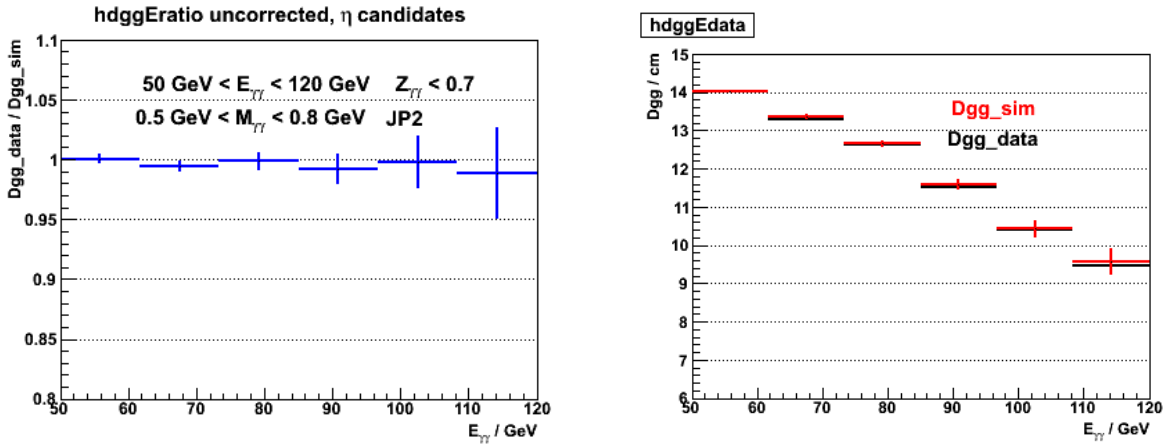

Figure 3.21: Di-photon separation *vs* pair energy in data and simulation, 0.5 GeV $< M_{\gamma\gamma}$ < 0.8 GeV

For π^0 candidates the overall difference in $D_{\gamma\gamma}$ reconstruction between data and simulation is within $\sim 5\%$, while for η candidates the discrepancy is negligible. PYTHIA + GSTAR simulations are used to extract the π^0 signal and background contributions to the di-photon mass distribution. Figure 3.22 shows the comparison between the data and simulation for the mass, energy, energy sharing $Z_{\gamma\gamma}$ and pseudorapidity of the pair. The plots are made for events satisfying the high-threshold Jet-Patch trigger (JP2).

The $M_{\gamma\gamma}$ and $Z_{\gamma\gamma}$ distributions show good agreement between the data and the simulation. The agreement for the pair energy and pseudorapidity distributions is not as good. One of the reasons for this is that the behavior of the trigger was not simulated accurately due to the presence of detector non-uniformities in the data. For example, a few channels in the low pseudorapidity region might have higher than usual gains during the run therefore would trigger more frequently than other channels. Thus although offline calibration could estimate their actual gains accurately, there are still some channels which can produce an excess of photon pairs in the vicinity of the trigger threshold energy, which is around 40 GeV for the JP2 trigger.

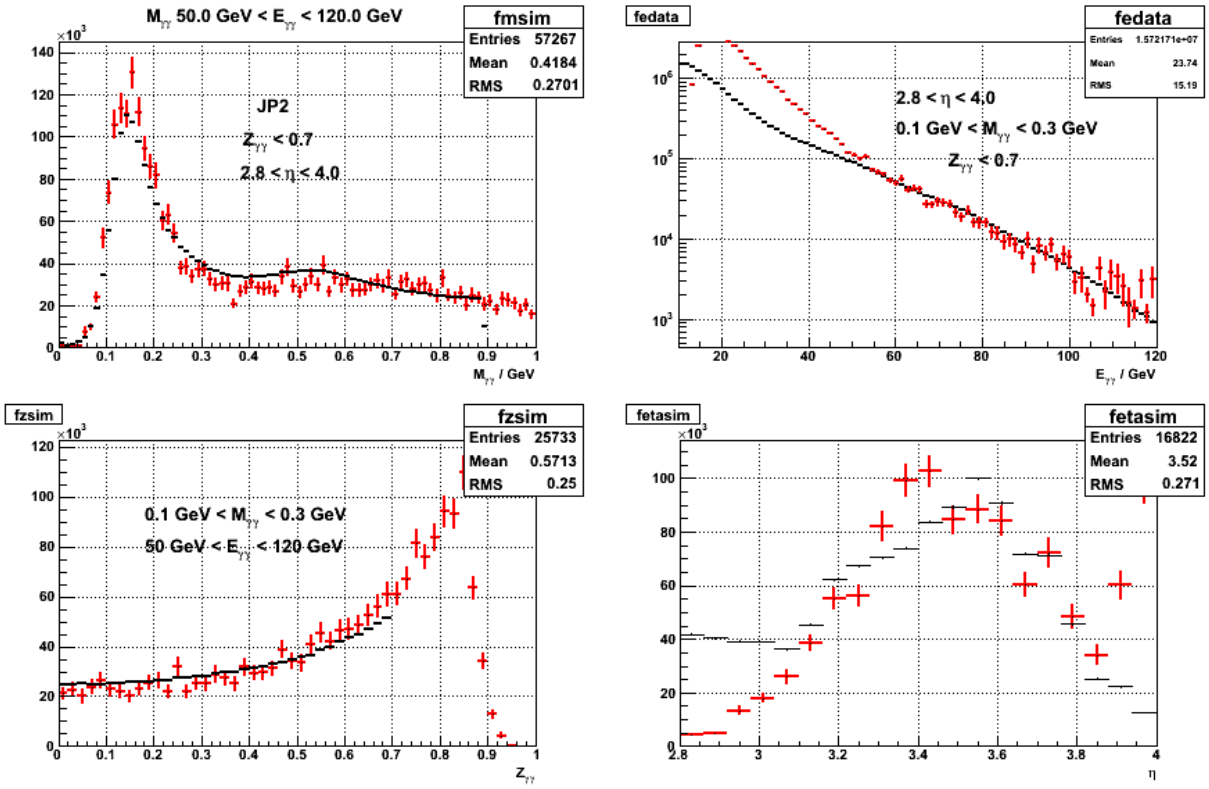

Figure 3.22: Data simulation comparison. Top Left: pair mass. Top Right: pair energy. Bottom Left: pair energy sharing. Bottom Right: pair pseudorapidity

3.5.3 Extracting the signal and background shapes from simulation

The di-photon mass distributions are used to extract the proportions of π^0 signals and backgrounds for asymmetry calculations. Since there is fairly good agreement between the mass distributions in the simulation and the data, the signal and background shapes can be modeled from the simulation, by matching the reconstructed photon to generated photon from the π^0 decay. Figure 3.23 shows one of the results, the decomposition of the raw di-photon mass distributions according to the origins of the photon pair.

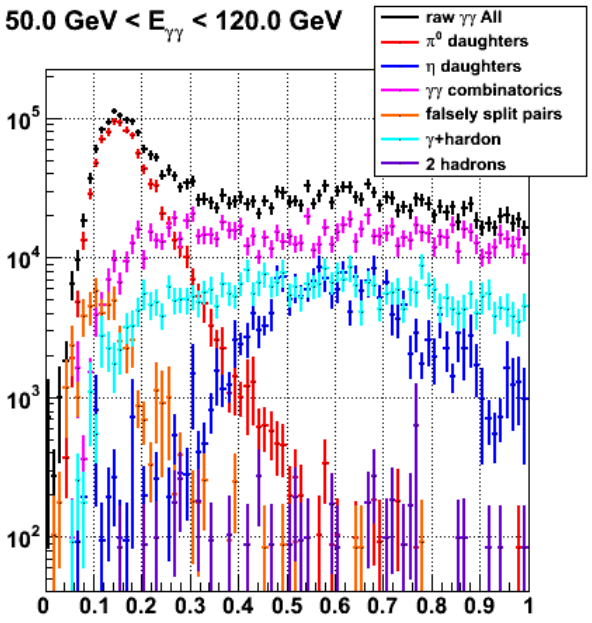

Figure 3.23: $M_{\gamma\gamma}$ decomposition in simulation

Note that $\gamma\gamma$ combinatorics means both of the reconstructed photons are matched to the daughter photons of a π^0 or η but they do not have the same parent. For each of the energy bins or (E, p_T) bins considered in the final analysis the shape of the mass distribution of the π^0 daughters are modeled with a skewed Gaussian function, while the rest of the components are lumped up together as background and are modeled with a 3rd order polynomial function. Figure 3.24 shows an example of such fits for simulated data from a single energy bin.

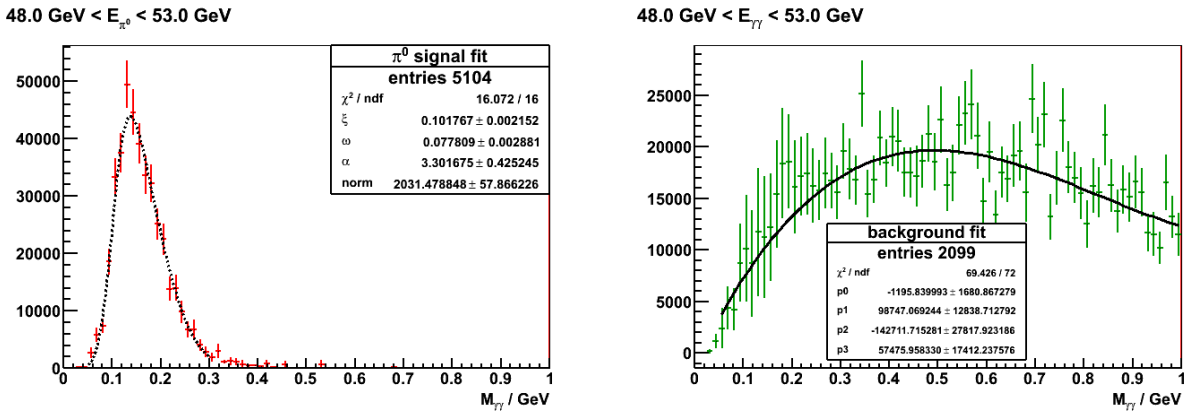

Figure 3.24: Fits to the signal and background shapes in simulation. 48 GeV $< E_{\gamma\gamma} <$ 53 GeV.

3.6 Asymmetry calculations

In this thesis work, both the inclusive asymmetries for π^0 and the event topology dependence of $A_N^{\pi^0}$ are measured and characterized. The method of extracting $A_N^{\pi^0}$ from the data will be discussed with the inclusive asymmetry measurements. The study of event topology dependence uses the same approach for asymmetry extraction except the samples are further selected with additional requirements to characterize the event structure.

3.6.1 Inclusive $A_N^{\pi^0}$ measurements

The signal and background templates are fitted to the di-photon mass distributions in the data, from which the fractions of π^0 signal pairs and background pairs are evaluated. The shape parameters of the templates are derived from simulation and used as the initial values of the fit. However they are allowed to vary during the fit. This is to account for the fact that the simulation does not fully reproduce data distributions and the full trigger mix is used in the data while only JP2 is selected for simulation. The dataset is divided up into several subsets each corresponding to a single fill. A fill represents an injection and store cycle of the proton beams in RHIC for collisions. A fill usually lasts about 6 to 8 hours. The final asymmetries are calculated fill-by-fill and then the average is taken. Figure 3.25 shows

an example of fitting to the di-photon mass distribution in the data for a single fill.

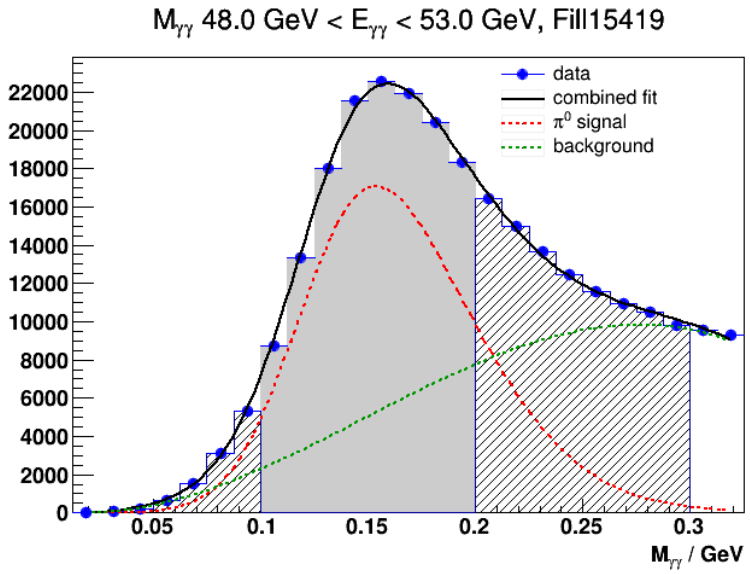

Figure 3.25: Signal and background fits to $M_{\gamma\gamma}$ distribution in data, 48 GeV $< E_{\gamma\gamma} <$ 53 GeV. Gray area: signal region. Shaded area: sideband region.

The mass range considered for asymmetry calculation is $0.0 < M_{\gamma\gamma} < 0.3$ GeV. This range is further divided into 2 regions, the signal region (0.1 GeV $< M_{\gamma\gamma} <$ 0.2 GeV) and the sideband region ($0.0 < M_{\gamma\gamma} <$ 0.1 GeV $\cup$ 0.2 $< M_{\gamma\gamma} <$ 0.3 GeV). As shown by the fits both signal and sideband regions contain π^0 signal and background contributions, so the following relations hold for the total asymmetries in these two regions

$$\begin{aligned} A_N^{total_{sig}} &= f_{sig_{sig}} * A_N^{\pi^0} + (1 - f_{sig_{sig}}) * A_N^{bkg} \\ A_N^{total_{sb}} &= f_{sig_{sb}} * A_N^{\pi^0} + (1 - f_{sig_{sb}}) * A_N^{bkg} \end{aligned} \tag{3.9}$$

In eq. 3.9 $A_N^{total_{sig}}$ and $f_{sig_{sig}}$ denote the raw asymmetries and signal fractions in the signal region, whereas $A_N^{total_{sb}}$ and $f_{sig_{sb}}$ denote the same quantities in the sideband. Note that the average background asymmetries are assumed to be the same in the signal region and the sideband. By solving these two equations simultaneously one can extract the asymmetries of the π^0 signal and the background. Figure 3.26 shows the π^0 signal fractions in the signal region *vs* fill number for the energy bin (48, 53) GeV. It is calculated with two methods: 1)

run-by-run fits to the mass distributions and taking the average over the runs in the same fill or 2) directly fitting the data from the entire fill. These two methods produced consistent results. Figure 3.27 shows the π^0 signal fractions in the sideband region vs fill number.

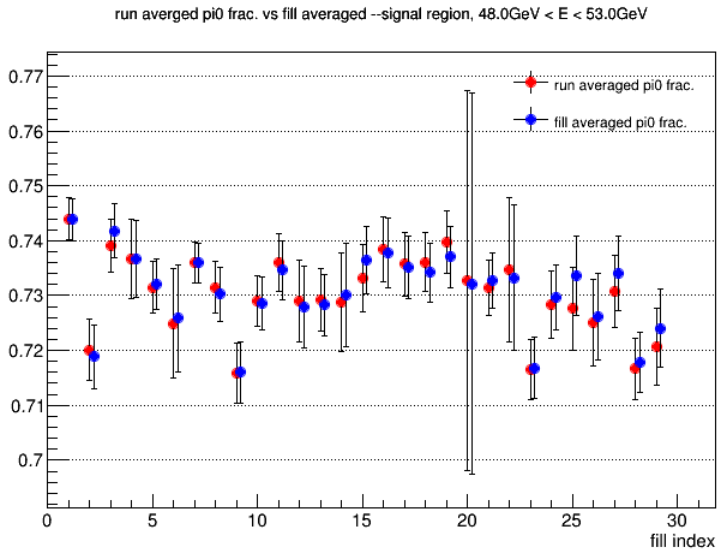

Figure 3.26: π^0 fractions in the signal region 0.1 GeV $< M_{\gamma\gamma} <$ 0.2 GeV vs relative fill number. 48 GeV $< E_{\gamma\gamma} <$ 53 GeV.

The signal and background fractions are used by eq. 3.9. Another piece needed in eq. 3.9 to calculate the signal and background asymmetries is the raw asymmetry A_N^{total} in signal and sideband regions ($A_N^{total_{sig}}$, $A_N^{total_{sb}}$). A_N^{total} is calculated by the azimuthal angle dependence of the cross-ratio (ratio of the product of yields with up and down spin configurations)

$$pol \cdot A_N^{total} \cos\phi = \frac{\sqrt{N^{\uparrow}(\phi)N^{\downarrow}(\phi+\pi)} - \sqrt{N^{\downarrow}(\phi)N^{\uparrow}(\phi+\pi)}}{\sqrt{N^{\uparrow}(\phi)N^{\downarrow}(\phi+\pi)} + \sqrt{N^{\downarrow}(\phi)N^{\uparrow}(\phi+\pi)}} \tag{3.10}$$

When eq. 3.10 is applied to $A_N^{total_{sig}}$ then $N_{sig}^{\uparrow}(\phi)$ represents the count of photon pairs at azimuthal angle ϕ and having $M_{\gamma\gamma}$ within the signal region (0.1 GeV, 0.2 GeV), when the the spin of the incoming polarized proton is pointing up. pol is the average polarization of the beam. Eq. 3.10 can be derived from the expression for the spin-dependent yield $N^{\uparrow}(\phi)$

$$N^{\uparrow}(\phi) = \epsilon^{\uparrow}\mathcal{L}^{\uparrow}(1 + pol \cdot A_N \cos\phi) \tag{3.11}$$

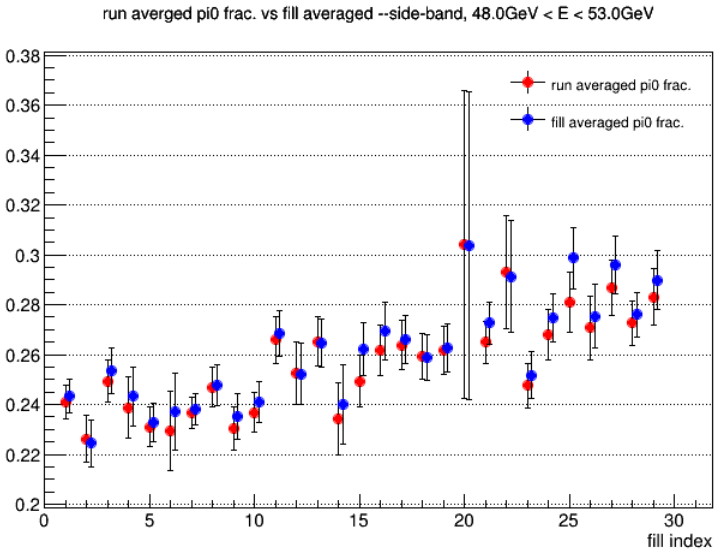

Figure 3.27: π^0 fractions in the sideband 0.0 GeV $< M_{\gamma\gamma} <$ 0.1 GeV $\cup$ 0.2 GeV $< M_{\gamma\gamma} <$ 0.3 GeV *vs* relative fill number. 48 GeV $< E_{\gamma\gamma} <$ 53 GeV.

Where $\epsilon^{\uparrow}$ and $\mathcal{L}^{\uparrow}$ are the spin-dependent detector acceptance and luminosity. These factors cancel out in the cross-ratio calculation.

In practice the azimuthal angle ϕ on the detector is divided into 10 bins and the pair of ϕ pieces opposite to each other are used to form the cross-ratio for that specific angle, as shown in Figure 3.28. The calculated raw asymmetry for each ϕ is then plotted against cosϕ and fitted by a linear function, for which the slope determines $pol \cdot A_N^{total}$. Figure 3.29 shows an example of extracting $pol \cdot A_N^{total}$ from the cosϕ dependence of the cross-ratio

Combining all the steps above, the π^0 signal asymmetry $A_N^{\pi^0}$ as well as the background asymmetry A_N^{bkg} can be calculated for the selected kinematic range on a fill-by-fill basis using the fill-averaged beam polarizations (pol). Figure 3.30 shows $A_N^{\pi^0}$ *vs* relative fill number. The average of $A_N^{\pi^0}$ over all of the fills is taken as the measured π^0 asymmetry in that particular kinematic bin. For this analysis the inclusive π^0 transverse single spin asymmetries are measured against π^0 energy as well as its transverse momentum given an energy range. The final results and estimates of their uncertainties will be discussed in the next chapter.

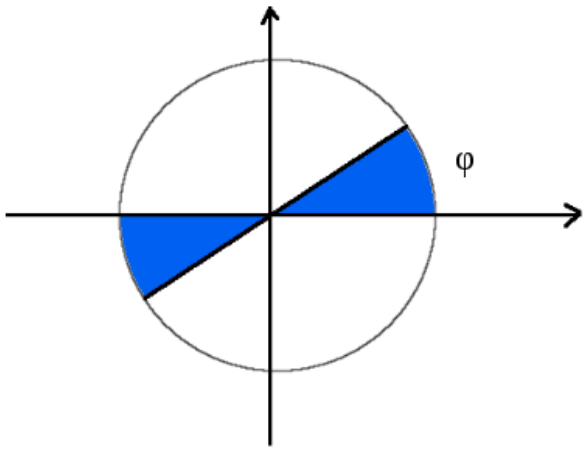

Figure 3.28: Blue: a pair of phi bins used for the cross-ratio calculation

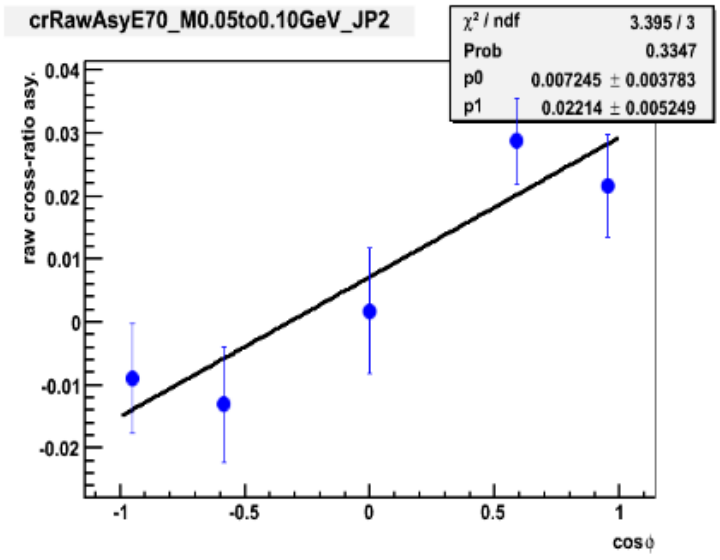

Figure 3.29: Extracting A_N^{total} from the cosϕ dependence of the cross-ratio for a specific mass range and energy bin

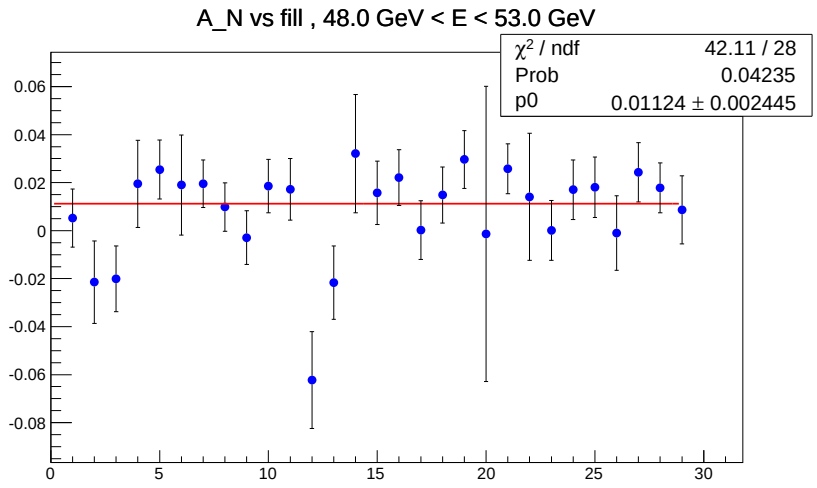

Figure 3.30: π^0 signal asymmetry $A_N^{\pi^0}$ *vs* relative fill number. 48 GeV $< E_{\gamma\gamma} <$ 53 GeV

3.6.2 Event topology dependence of $A_N^{\pi^0}$

In addition to the inclusive asymmetry measurements, the large acceptance of the FMS at forward rapidities also allows for the study of how the amplitude of $A_N^{\pi^0}$ depends on the event activities in the neighborhood of the π^0. Until now, all of the theoretical treatments of TSSAs are based on an assumption that the observed π^0 is a result of the fragmentation of partons originating from hard-scatterings. The fraction of the parton's momentum taken by the π^0 is denoted by z, which to some extent also represents how complex the final state event structure is. For example if the z of the π^0 is very close to 1 that means the final products from the fragmentation are dominated by the π^0 with some very soft particles at low energies. If on the other hand the z of π^0 is an intermediate value ~ 0.4 there could be significant amount of energy shared by other final state products. Thus the resultant events could have more complex topologies involving multiple particles.

Models based on the initial-state effects for TSSA do not have preferences on how the fragmentation variable will affect $A_N^{\pi^0}$ because the asymmetry is entirely generated by the

partons inside the proton before the scattering. Final-state models such as the Collins effect predict a z-dependence of A_N, which can be understood as follows: At very low z the parton or jet momentum is dominated by other products from the fragmentation. Even though the π^0 can be off the jet axis therefore having non-zero transverse momentum k_T relative to its parent parton, the magnitude of k_T is not large enough to generate significant asymmetries. On the other hand at very high z the parton (or jet) momentum is going to be dominated by the π^0 itself, which prevents the π^0 from having sizable k_T with respect to the parton, therefore the asymmetries will be small too. Only when the π^0 has an intermediate z value can it have a significant value of A_N. Figure 3.31 shows a recent extraction of the Collins fragmentation functions from SIDIS and e^+e^- annihilation processes for $u \to \pi^+$ (favored) and $u \to \pi^+$ (unfavored) [63]. The fragmentation function has the expected behavior as the above reasoning.

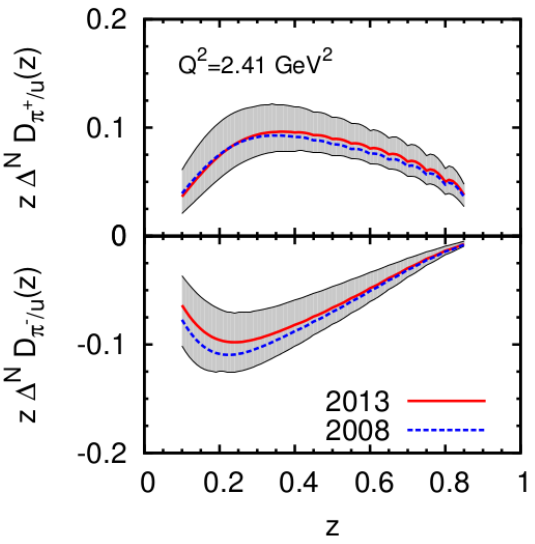

Figure 3.31: Collins fragmentation function extracted from SIDIS and e^+e^- annihilation

A full jet reconstruction at the forward rapidities in STAR is not possible due to the lack of hadronic calorimeters. But one can still tap into the final-state effects especially the z-dependence of A_N by studying the π^0 inside the electromagnetic component of a jet. The EM component of the jet is obtained by a jet finding algorithm using the reconstructed photons from the FMS. The event activities in the vicinity of the π^0 is characterized by the fraction

of the momentum of the EM-jet taken by the π^0, denoted by z_{em}. The z_{em} dependence of $A_N^{\pi^0}$ reflects how the asymmetry is affected by the degree of isolation of the π^0. To obtain an overview of the global event structure Figure 3.32 shows the azimuthal angle correlations between a π^0 candidate in the FMS and the rest of the FMS photons, as well as between a FMS π^0 candidate and the jets reconstructed from the Barrel Electro-Magnetic Calorimeter at mid-rapidity ($|y| < 1$). Due to the lack of TPC readout in the FMS dataset only the EM component of the mid-rapidity jet can be reconstructed.

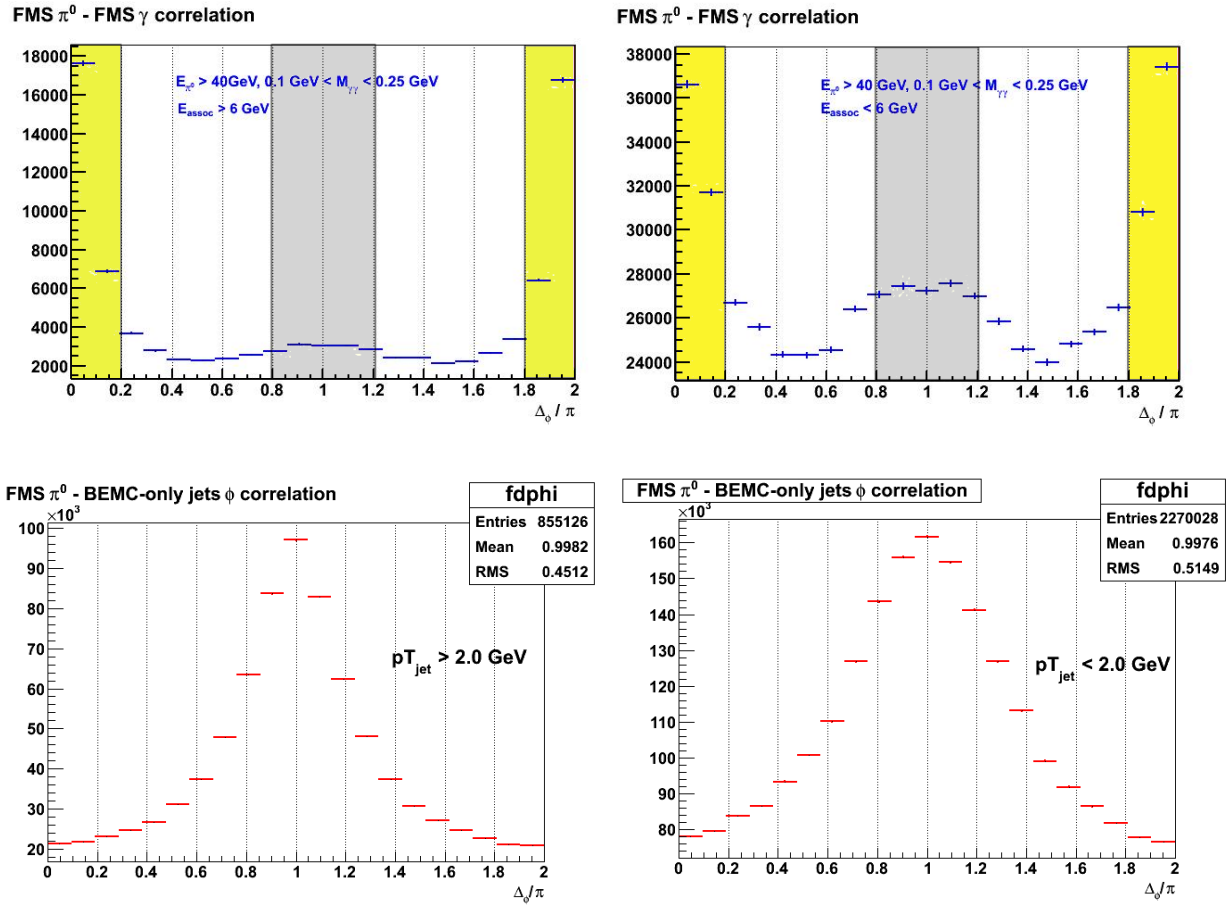

Figure 3.32: FMS π^0-FMS γ and FMS π^0-BEMC jet azimuthal angle correlations. $\Delta_\phi = \phi_{\pi^0} - \phi_{jet}$.

For this analysis, jets in the FMS and BEMC are reconstructed by anti-k_T algorithm [64] with distance parameter R = 0.7. It can be seen from the top row of Figure 3.32 that the presence of additional photons in the neighborhood of a π^0 candidate greatly enhances the

correlation strength on the near-side ($\Delta\phi \sim 0$) due to the rapid increase of the combinatorial background. For some of the events there are also increased activities on the away-side ($\Delta\phi \sim \pi$) of the π^0 candidate either in the forward rapidity (top row) or in the mid-rapidity (bottom row). These are generated by the fragmentation of the other hard-scattered parton.

The event topology dependence of $A_N^{\pi^0}$ is studied under two extreme scenarios. First A_N is measured for the reconstructed jets that only contain two photons and the mass of the photon pair is less than 0.3 GeV. This sample is dominated by isolated π^0 with nothing around it. Next another A_N is measured for π^0 inside a jet which contains more photons other than the daughters of the π^0. This requirement is enforced by the cut $z_{em} < 0.9$, where the 0.9 cut of z_{em} only removes highly isolated π^0 (with $z_{em} \sim 1$). For the second case a background subtraction procedure similar to the inclusive measurements was performed in order to calculate the π^0 signal asymmetries. One can imagine that in this scenario the combinatorial background can be higher than the inclusive π^0 due to the presence of additional photons next to the π^0. This is indeed the case and one of the example is shown in Figure 3.33. The di-photon mass distribution is Figure 3.33 can be directly compared with the inclusive mass spectrum shown in Figure 3.25, from which a clear enhancement in the background level is observed.

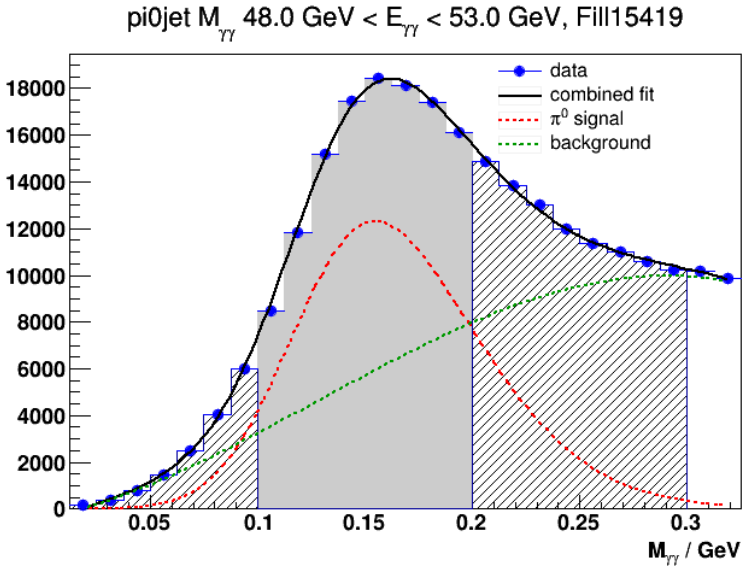

Figure 3.33: Di-photon mass distribution for photons in jet with $z_{em} < 0.9$

The comparison of asymmetries between inclusive π^0, isolated π^0 and π^0 in jets with z_{em} < 0.9 will be discussed in the next chapter. With the reconstructed EM-jets and π^0 one can also measure the Collins asymmetries of the π^0 azimuthal angle distribution with respect to the jet axis. Results of the Collins asymmetry will also be discussed in the next chapter.

CHAPTER 4

Results

This chapter presents the main results of the inclusive π^0 transverse single spin asymmetry measurements in transversely polarized proton-proton collisions at $\sqrt{s} = 500$ GeV. The observation of the event topology dependence of $A_N^{\pi^0}$ as well as the measurement of the Collins asymmetries of π^0 will also be shown and discussed.

4.1 Inclusive π^0 transverse single spin asymmetries

The transverse single spin asymmetries of π^0 signal and the background can be calculated by eq. 4.1.

$$\begin{aligned} A_N^{total_{sig}} &= f_{sig_{sig}} * A_N^{\pi^0} + (1 - f_{sig_{sig}}) * A_N^{bkg} \\ A_N^{total_{sb}} &= f_{sig_{sb}} * A_N^{\pi^0} + (1 - f_{sig_{sb}}) * A_N^{bkg} \end{aligned} \tag{4.1}$$

In practice $A_N^{\pi^0}$ is computed on a fill-by-fill basis, then the average is taken as the final result. An example of $A_N^{\pi^0}$ *vs* fill number is shown in Figure 3.30. Figure 4.1 shows the result of the inclusive π^0 and background asymmetries *vs* Feynman-x x_F.

In Figure 4.1 the π^0 asymmetries are calculated for both positive x_F and negative x_F regions. The data points with negative x_F are obtained by sorting the spin of the proton according to the polarization of the beam going away from the FMS (the Yellow beam), for which the detector is located at the backward rapidity region. The asymmetries for negative x_F is consistent with zero since the spin of low-x soft partons do not maintain significant correlations with the spin of their parent proton. A large $A_N^{\pi^0}$ is observed in the positive x_F region and its magnitude increases with x_F, while the background asymmetries is systematically lower. The background asymmetry is non-zero at high x_F since the major

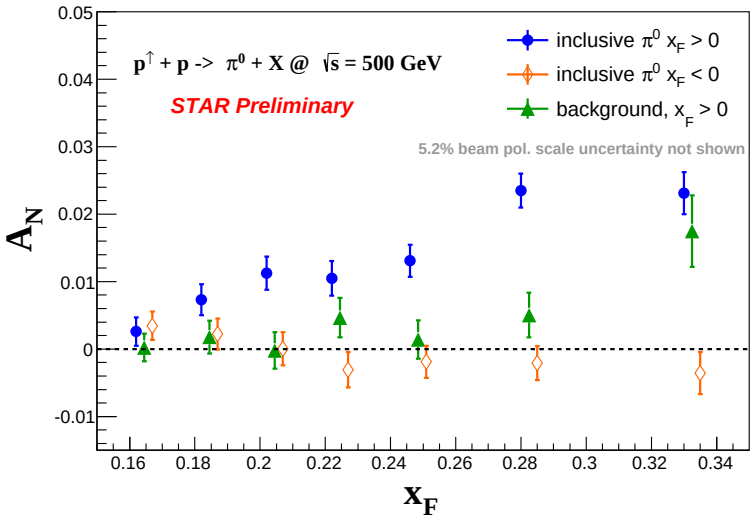

Figure 4.1: Transverse single spin asymmetries of inclusive π^0 and background

background contribution is from the combinatorics of photons from different π^0, mostly at low energy, therefore the photons themselves partially carry the asymmetries of their parent π^0.

The transverse momentum dependence of $A_N^{\pi^0}$ is also important for testing theoretical models. Figure 4.2 shows the p_T dependence of $A_N^{\pi^0}$ in two x_F bins. The uncertainty estimations of $A_N^{\pi^0}$ as well as the energy scales of the π^0 will be discussed in later part of this chapter.

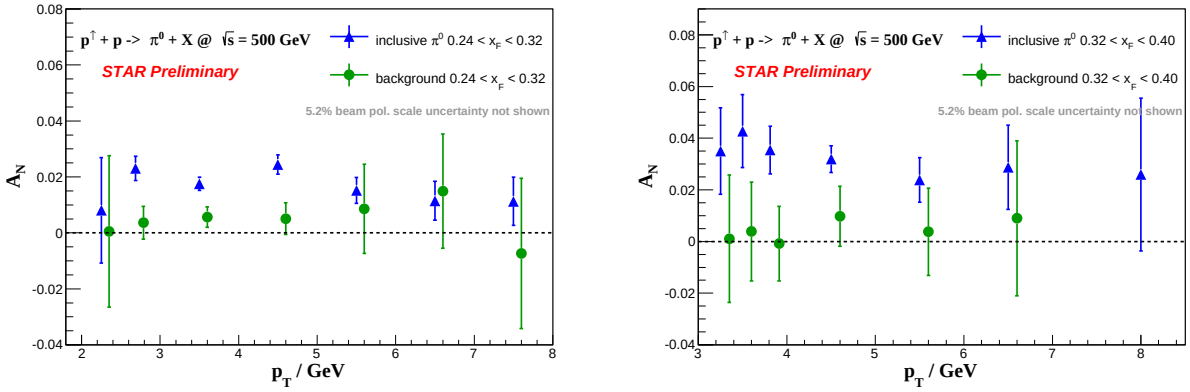

Figure 4.2: p_T dependence of $A_N^{\pi^0}$ in two x_F bins

4.2 Event topology dependence of $A_N^{\pi^0}$

The event topology dependence of π^0 asymmetries is characterized by measuring $A_N^{\pi^0}$ under two extreme scenarios. First the asymmetry is measured for isolated π^0 with nothing in their vicinity. The isolation condition is defined by an anti-k_T jet algorithm with the distance parameter R = 0.7 and requiring nothing else in the jet except the two photons from the π^0 decay. In the other extreme, the asymmetry is measured for the π^0 that must be part of the EM component of a jet and the π^0 momentum as a fraction of the momentum of the jet's EM component is less than 0.9 ($z_{em} < 0.9$). This means that there must be other particles in the same jet which contribute to the jet's total EM component. Figure 4.3 shows the comparison of the asymmetries obtained under these two scenarios, together with the inclusive π^0 asymmetry.

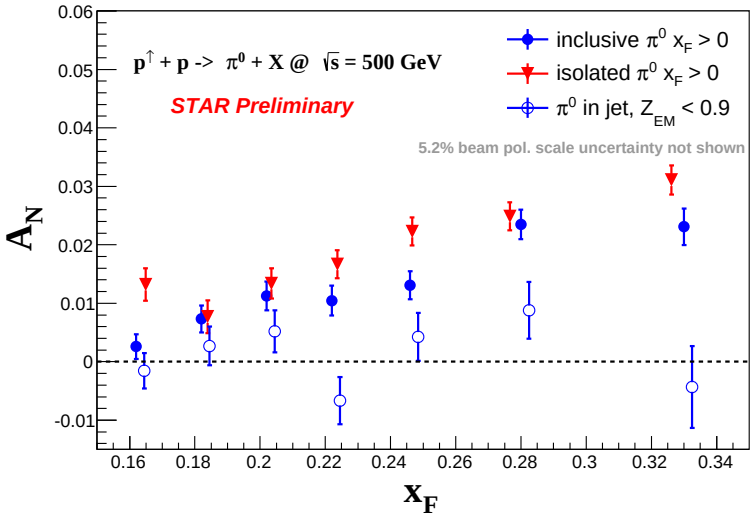

Figure 4.3: Comparing the asymmetries of inclusive, isolated and non-isolated π^0

At high x_F, there is significant difference between the asymmetries of isolated π^0 and non-isolated π^0. Note that for isolated π^0 the z_{em} is effectively at 1. Comparing to the z_{em} < 0.9 cut applied to the non-isolated π^0 sample this difference means there is either very dramatic z_{em} dependence of the asymmetry in going from 0.9 to 1, or these two scenarios actually correspond to different physical processes involved and only one of them is respon-

sible for the observed large $A_N^{\pi^0}$. Note that the jet reconstructed in this analysis is only the electromagnetic component, charged hadrons produced from the parton fragmentation do not register significant signals in the FMS most of the time therefore the jet sample has significant bias due to the FMS detector. A more complete analysis can be done in the future with the full electromagnetic and hadronic calorimeters in the forward rapidities of STAR.

4.3 Collins asymmetries of π^0 in jet

The Collins effect manifests itself as an azimuthal angle (Collins angle ϕ_C) modulation of the π^0 yield around the jet axis. The sign of the modulation depends on the orientation of the proton spin and the flavor of the quark involved in the hard scattering. Figure 4.4 shows the geometry of the Collins mechanism. In practice the Collins angle ϕ_C is calculated by $\phi_C = \phi_S$ - ϕ_H where ϕ_S represents the angle between the proton spin and the scattering plane formed by the beam direction and the jet momentum vector and ϕ_H is the azimuthal angle of the produced hadron (π^0 in this case) in a Cartesian coordinate system defined by the beam direction, jet momentum vector and the proton spin. The definition of the Collins angle in this analysis is identical to that used in the Collins asymmetry measurements in the mid-rapidity at STAR [65].

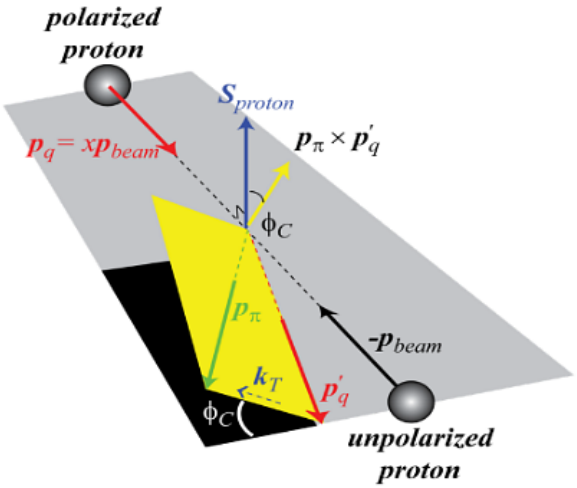

Figure 4.4: Collins mechanism in pp collisions

The total, π^0 signal and background Collins asymmetries $A_{UT}^{\sin(\phi_S-\phi_H)}$ are related by an equation similar to eq. 3.9. The asymmetry is measured as a function of x_F and z_{em} separately. Figure 4.5 shows an example of the fits to the di-photon mass distributions in a single z_{em} bin. Figure 4.6 shows the π^0 Collins asymmetry vs z_{em} as well as the background asymmetry. Figure 4.7 shows the Collins asymmetry vs x_F. Compared to the π^0 single spin asymmetries the magnitude of the Collins asymmetry is much smaller. This behavior is expected in theory due to the cancellation of u and d quark contributions to the π^0 Collins fragmentation function. The systematic uncertainty of this measurement will be discussed in the next section.

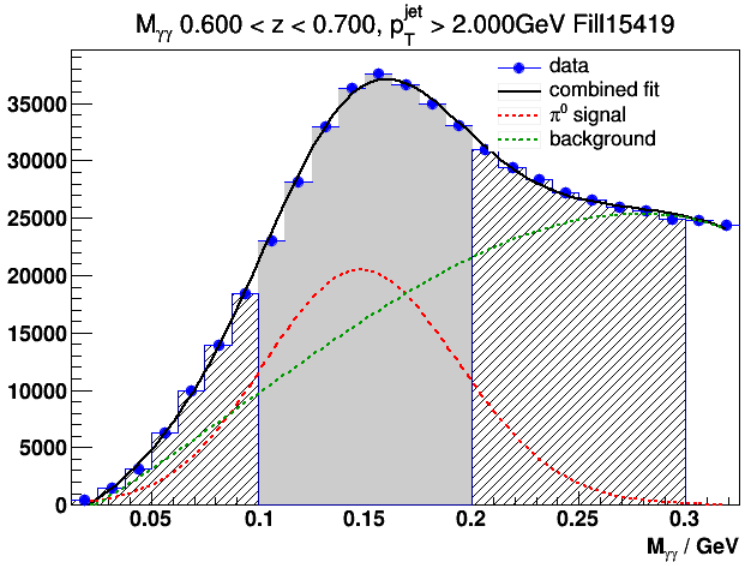

Figure 4.5: Signal and background fits to $M_{\gamma\gamma}$ distribution in data, $0.6 < z_{em} < 0.7$ and $p_T^{jet} > 2$GeV. Gray area: signal region. Shaded are: sideband.

4.4 Uncertainties in the asymmetry measurements

For the asymmetry calculations the statistical uncertainties of $A_N^{\pi^0}$ and $A_{UT}^{\sin(\phi_S-\phi_H)}$ originate from the uncertainties in the yield of the photon pairs with 0 GeV $< M_{\gamma\gamma} <$ 0.3 GeV. The systematic uncertainties mainly come from the uncertainties in estimating the π^0 signal and background fractions as well as the beam polarization. An additional systematic uncertainty

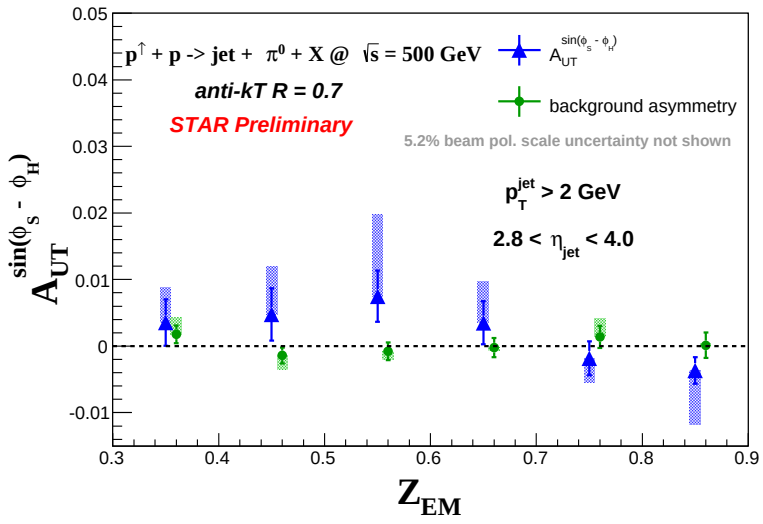

Figure 4.6: π^0 Collins asymmetry v.s. z_{em}. Blue: signal. Green: background. Vertical bars are the statistical uncertainties while the bands are systematic uncertainties due to Collins angle resolutions.

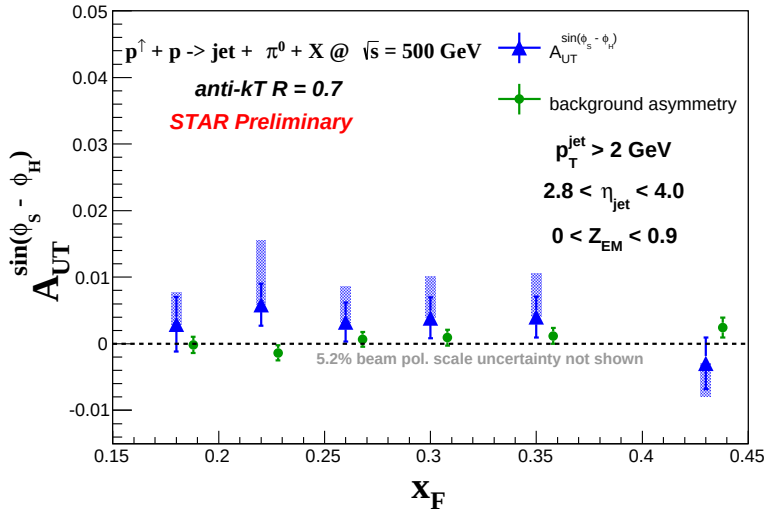

Figure 4.7: π^0 Collins asymmetry v.s. x_F. Blue: signal. Green: background. Vertical bars are the statistical uncertainties while the bands are systematic uncertainties due to Collins angle resolutions.

for the Collins asymmetry measurements comes from the resolution of the Collins angle which dilutes the amplitude of the Collins asymmetry. As most of the asymmetries are measured within specific energy or transverse momentum bins the systematic uncertainties associated with the energy scales are also important.

4.4.1 Statistical uncertainties of $A_N^{\pi^0}$ and $A_{UT}^{\sin(\phi_S-\phi_H)}$

Since both $A_N^{\pi^0}$ and $A_{UT}^{\sin(\phi_S-\phi_H)}$ are calculated by eq. 4.1 they can be expressed by the following functional form (take $A_N^{\pi^0}$ as an example)

$$\begin{aligned} A_N^{\pi^0} =& F(f_{sig_{sig}}, f_{sig_{sb}}, A_N^{total_{sb}}, A_N^{total_{sig}}) \\ A_N^{bkg} =& G(f_{sig_{sig}}, f_{sig_{sb}}, A_N^{total_{sb}}, A_N^{total_{sig}}) \end{aligned} \tag{4.2}$$

By Differentiating eq. 4.2 with respect to $A_N^{total_{sb}}$ and $A_N^{total_{sig}}$ one can obtain the statistical uncertainties for $A_N^{\pi^0}$ and A_N^{bkg} through the standard propagation of uncertainties. The uncertainties of the total asymmetries contribute to $\sigma_{A_N^{\pi^0}}$ and $\sigma_{A_N^{bkg}}$ quadratically via coefficients such as $\frac{\partial A_N^{\pi^0}}{\partial A_N^{total}}$. These coefficients can be calculated by solving eq. 4.1. Uncertainties of A_N^{total} are obtained as follows.

According to the cross-ratio formula 3.10, A_N^{total} receives contributions from the beam polarization uncertainties and the uncertainties in the raw asymmetry

$$\epsilon = \frac{\sqrt{N^{\uparrow}(\phi)N^{\downarrow}(\phi+\pi)} - \sqrt{N^{\downarrow}(\phi)N^{\uparrow}(\phi+\pi)}}{\sqrt{N^{\uparrow}(\phi)N^{\downarrow}(\phi+\pi)} + \sqrt{N^{\downarrow}(\phi)N^{\uparrow}(\phi+\pi)}} \tag{4.3}$$

The azimuthal angle ϕ is usually measured with high precision and its resulting error is negligible compared to other uncertainties. The beam polarization uncertainty combines the overall scale uncertainty of p-Carbon/H-jet polarimeters and the fill-to-fill systematic uncertainties over the 29 fills included in this analysis. The final beam polarization uncertainty is 5.2%. The uncertainty in the raw asymmetry ϵ is

$$\begin{aligned}\sigma_\epsilon^2 =& \frac{(N^\uparrow(\phi)+N^\downarrow(\phi+\pi))(N^\downarrow(\phi)+N^\uparrow(\phi+\pi))}{\left[\sqrt{N^\uparrow(\phi)N^\downarrow(\phi+\pi)}+\sqrt{N^\downarrow(\phi)N^\uparrow(\phi+\pi)}\right]^4} \\ =& + \frac{(N^\downarrow(\phi)+N^\uparrow(\phi+\pi))(N^\uparrow(\phi)+N^\downarrow(\phi+\pi))}{\left[\sqrt{N^\uparrow(\phi)N^\downarrow(\phi+\pi)}+\sqrt{N^\downarrow(\phi)N^\uparrow(\phi+\pi)}\right]^4}\end{aligned} \tag{4.4}$$

4.4.2 Systematic uncertainties of the signal fractions

By Differentiating eq. 4.2 with respect to $f_{sig_{sig}}$ and $f_{sig_{sb}}$ one can compute the systematic uncertainties of $A_N^{\pi^0}$ and A_N^{bkg} due to the uncertainties in the signal fractions. The main contribution to the uncertainties of the signal fractions comes from the fitting procedure. For this analysis the propagation of the uncertainties of the fitting parameters to the signal fractions was done by a toy Monte Carlo simulation. The analytical method for uncertainty propagation involves complicated expressions and can only be solved by approximation. The toy Monte Carlo simulation generates pseudo-random numbers which reproduce the covariance matrix of the 8 parameters (4 parameters for π^0 signal, the other 4 for the background) obtained from fitting the signal and background templates to the data. For each set of 8 fitting parameters a new signal fraction can be calculated. The sample of all signal fractions from running the Monte Carlo simulation can be used to estimate the variations of these fractions caused by uncertainties in the fitting parameters. Figure 4.8 shows the workflow of the toy Monte Carlo simulation.

First the covariance matrix of the 8 parameters is obtained from fits to the $M_{\gamma\gamma}$ distribution in data (e.g Figure 3.25). This covariance matrix (Cov) can be factorized into the product of a lower triangular matrix (U) and its conjugate transpose (U^T) by the Cholesky decomposition.

$$Cov = UU^T \tag{4.5}$$

Then the U matrix is used to correlate a set of 8 random variables sampled independently from the standard normal distribution $N(0,1)$. Each set of transformed variables can be

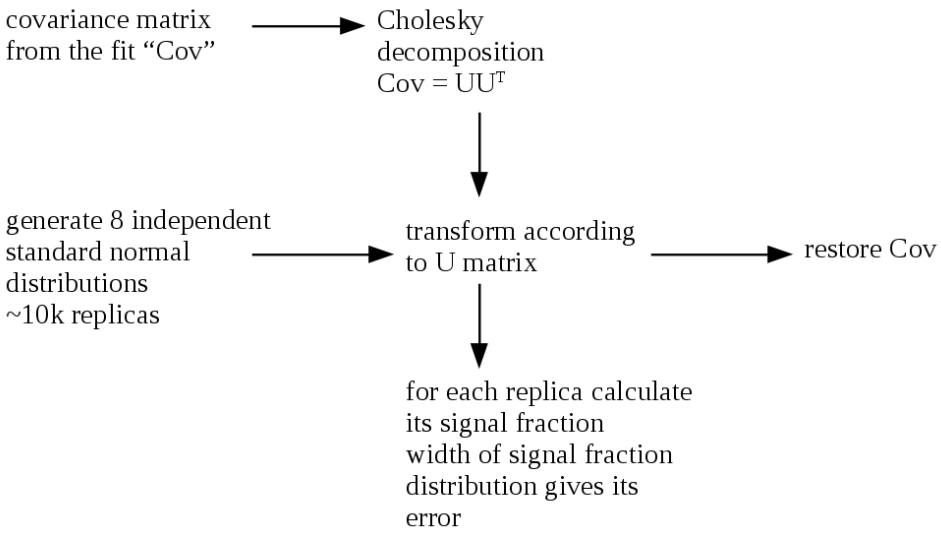

Figure 4.8: The toy MC routine to propagate uncertainties in fitting parameters to the signal fraction

considered as a result of conducting a pseudo-experiment of fitting the signal and background templates to a different data set. Therefore a new signal fraction can be calculated from a set of fitting parameters obtained from the sampling procedure. Finally the width of the distribution of the signal fractions can be used as the uncertainty of f_{sig}. Figure 4.9 shows an example of fitting to the distribution of π^0 signal fractions obtained from running the MC routine multiple rounds.

4.4.3 Systematic uncertainties in $A_{UT}^{\sin(\phi_S-\phi_H)}$ due to Collins angle resolutions

The resolution of the Collins angle is estimated by comparing the reconstructed Collins angle to the one generated in simulation, for the pair of reconstructed π^0 and its matched π^0 generated by PYTHIA as well as their associated jets at detector level and particle level . Figure 4.10 shows the distributions of the difference between the reconstructed Collins angle and the generated one for 6 z_{em} bins. To estimate the reduction of the amplitudes of the Collins asymmetry due to this resolution effect, a $\sin\phi_C$ modulation of the π^0 yield is generated in a toy Monte Carlo model for each z_{em} bin. The ϕ_C angle of each entry is then smeared according to the resolution shown in Figure 4.10. The result of this angle smearing

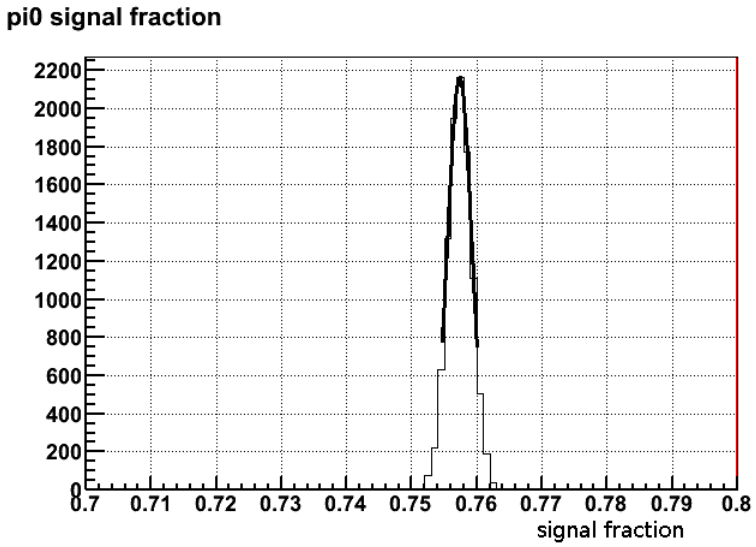

Figure 4.9: Fitting to the π^0 signal fraction distribution from toy MC for the 70 GeV energy bin.

is a different $\sin\phi_C$ modulated yield with reduced amplitude, as shown in Figure 4.11. In practice it is found that the initial amplitude of the $\sin\phi_C$ modulation does not affect the degree of reduction. The ratio of the amplitude before and after the smearing is taken as a relative systematic uncertainty of $A_{UT}^{\sin(\phi_S-\phi_H)}$. It is a one-sided uncertainty since the resolution effect will always reduce the true Collins asymmetry. This uncertainty is shown as the blue and green bands in Figure 4.6 and 4.7.

4.4.4 Systematic uncertainties of the energy scales

Uncertainty of the π^0 energy is estimated by comparing the mass of the reconstructed π^0 in data and simulation. For this method to work other effects in reconstructing the π^0 mass need to be quantified. These include the di-photon separation ($D_{\gamma\gamma}$) measurement and bin-migrations of the reconstructed mass due to the energy resolution and the steeply falling energy spectrum.

The highest energy bin in the x_F dependence of the $A_N^{\pi^0}$ measurement (Figure 4.1) is (75, 90) GeV. Comparisons of $D_{\gamma\gamma}$ in Figure 3.20 shows that $D_{\gamma\gamma}$ in simulation is higher than

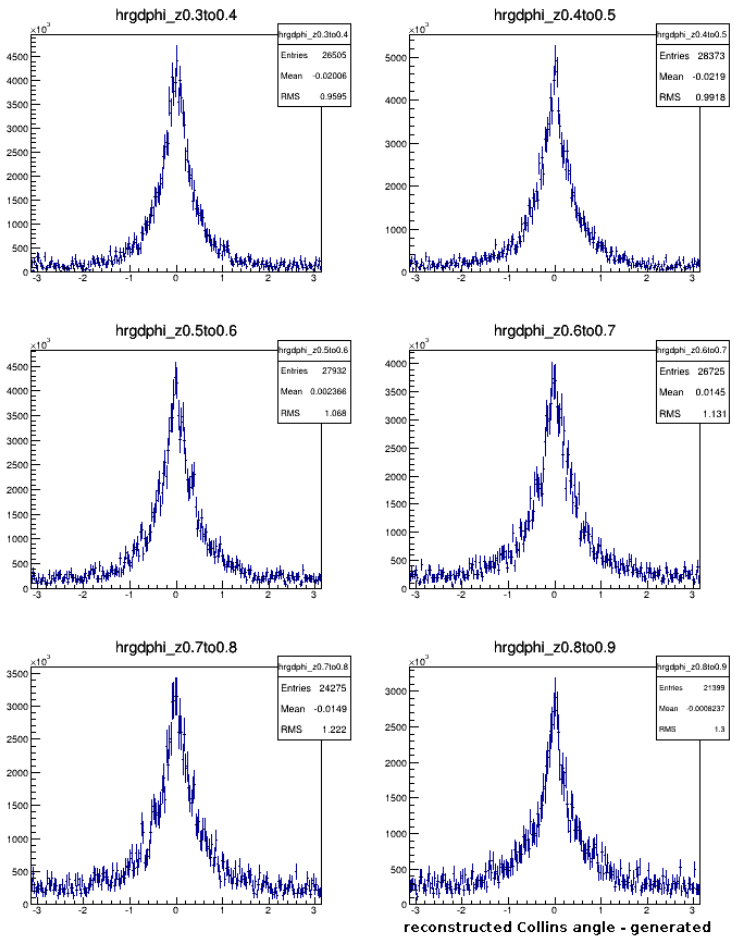

Figure 4.10: Difference between the reconstructed Collins angle and the generated Collins angle in PYTHIA for 6 z_{em} bins

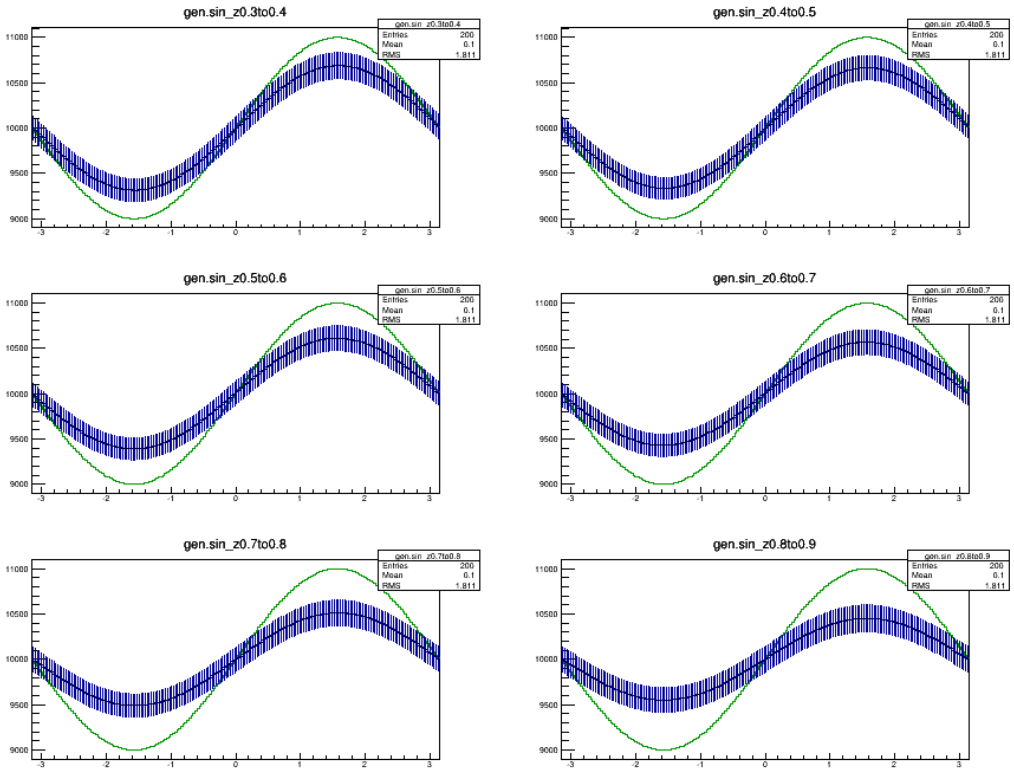

Figure 4.11: Reduction in the amplitude of $\sin\phi_C$ modulation due to ϕ_C resolutions

that in data by $\sim 5\%$ for this region. As a result the reconstructed π^0 mass in simulation could be 5% higher than that in data even if the energy scales in data are determined correctly. As an initial test, single π^0 events are generated in simulation with a flat energy distribution. Figure 4.12 shows an example of comparing the reconstructed π^0 mass from this single particle simulation sample and the fit to the di-photon mass distribution for a particular ($E_{\gamma\gamma}$, p_T) bin in data.

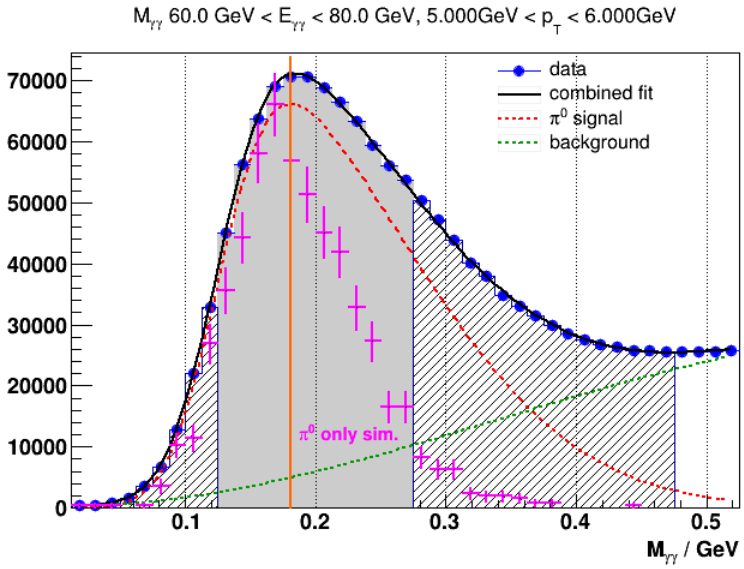

Figure 4.12: Comparing π^0 in data and the reconstructed mass from single π^0 simulation sample

The reconstructed π^0 mass is 0.17 GeV for the simulation sample and 0.18 GeV for data, both are higher than the PDG value of π^0 mass. Part of the reasons for this effect has been discussed in the data simulation comparison section of Chapter 3, where it was shown that the di-photon separation tends to be over-estimated for π^0 (Figure 3.19). The other reason could potentially come from the insufficient correction for the bin-migration effect. Bin-migration refers to the effect of over-estimating the bin-by-bin averages of an observed quantity compared to its true value when the quantity itself or the variable on which it depends has a steeply falling distribution and the observation comes with finite resolutions [57]. Applied to the case of $E_{\gamma\gamma}$ measurements one can see that since the true $E_{\gamma\gamma}$ has a steeply falling spectrum towards high energies, for any particular observed energy bin

there are always going to be more entries migrated from lower energy bins due to resolution than the entries migrated to the higher energy bins. Therefore the average observed energy in the bin is always going to be greater than the expected average of the true energy in this bin. This also applies to any other measurements which depend on the observed energy, e.g. $M_{\gamma\gamma}$. The strategy implemented in this analysis for correcting such effect is to force the average of the observed $M_{\gamma\gamma}$ of η mesons to be the same as the true value. This puts the average reconstructed mass within a bin to the correct scale, while in general it underestimates the reconstructed masses when they're compared to their true values one by one. The later scenario usually requires an unfolding step for measurements that have a strong dependence on energy. But since the single spin asymmetries do not have such a dramatic behavior, unfolding is not necessary for this analysis.

As discussed in section 4 of Chapter 3, the energy scale in the data is determined by calibrating the reconstructed π^0 mass at 25 GeV for large cells and at 40 GeV for small cells, and by forcing the reconstructed η mass to be constant over the energy range included in the analysis. To correctly compare the reconstructed mass in data and simulation, the simulated π^0 and η samples should have the same energy spectrum as the data. PYTHIA can be used to generate such samples but the steeply falling energy spectrum of the π^0/eta makes it very hard to collect enough statistics for the high energy bins. The method implemented here is to generate π^0/eta with a flat energy distribution and then re-weight the distribution according to the Next-to-Leading Order (NLO) pQCD calculations. Figure 4.13 compares the measurement of π^0 and η meson cross-sections at pseudorapidity 3.68 [61] and the prediction from NLO calculation (by W.Vogelsang et.al.)

Figure 4.14 shows the relative weighting factors derived from the NLO calculation. Its energy dependence is interpolated by a 3rd order Spline function shown as the red line. In the simulation for η mesons the energies of the η meson is re-weighted according to this curve to introduce the bin migration effect shown in Figure 4.15. In Figure 4.15 one can clearly see that the observed η mass tends to be shifted towards higher values, whereas it remains flat when generated with flat energy distribution before re-weighting. The red curve shown in Figure 4.15 is used to make corrections to the energy scales of the π^0 candidates in

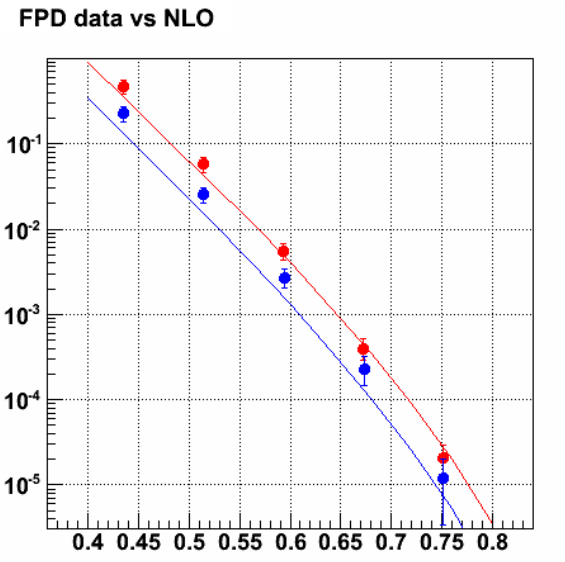

Figure 4.13: Comparing forward π^0 and η cross-sections to NLO calculation. Blue: η. Red: π^0. X-axis: x_F. Y-axis: $E\mathrm{d}^3\sigma/\mathrm{d}p^3$ $(\mu bc^3/GeV^2)$

simulation so as to mimic the procedure of bin-migration corrections in analyzing the real data. The reconstructed π^0 mass after this correction is shown in Figure 4.16 for the same $(E_{\gamma\gamma}, p_T)$ bin as Figure 4.12. The reconstructed π^0 mass is 0.16 GeV in simulation, compared to 0.18 GeV obtained from data. Together with the 5% difference from $D_{\gamma\gamma}$ reconstruction, this indicates the systematic uncertainty in the π^0 energy scales can be around 12% at high energy and transverse momentum.

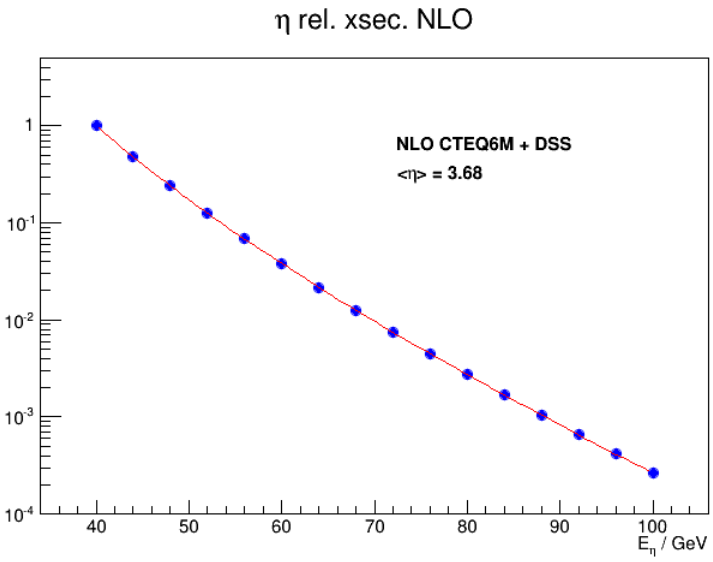

Figure 4.14: Weighting factors for η cross-section derived from NLO calculations. It is applied to a η-only simulation sample with flat energy distribution

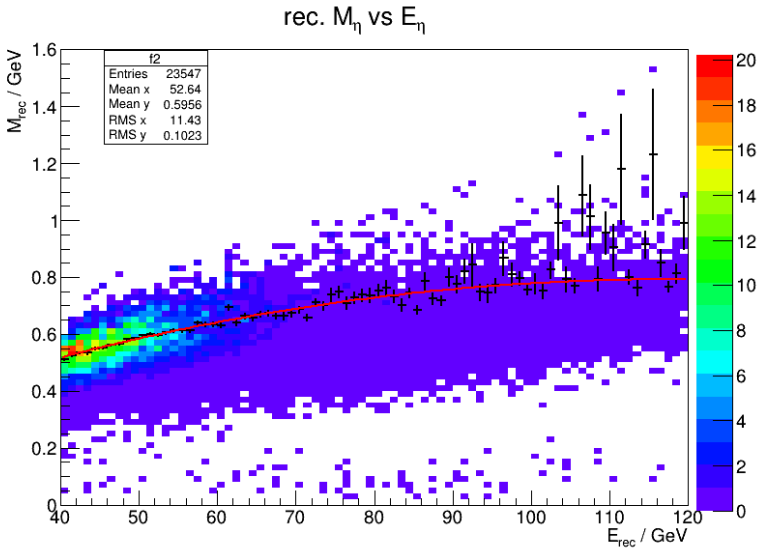

Figure 4.15: Reconstructed η mass *vs* energy after re-weighting

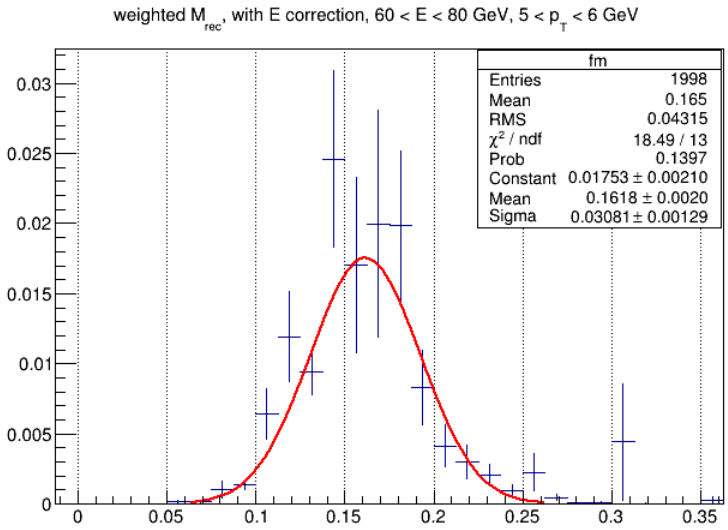

Figure 4.16: Reconstructed π^0 mass in simulation after bin-migration correction

CHAPTER 5

Simulations for STAR forward calorimeter upgrade

This chapter documents the simulation work done related to a STAR R&D project for detector upgrade at forward rapidity [66]. The goal of the STAR forward upgrade project is to expand the physics programs of forward rapidity measurements in polarized proton-proton, proton-nucleus and nucleus-nucleus collisions. Scientific topics covered by the forward upgrade project include the Sivers/Collins asymmetry measurements with fully reconstructed jets to examine the TMD factorization framework and and the study of the transverse spin structure of the proton, transverse single spin asymmetries of Drell-Yan production, longitudinal double spin asymmetry measurement of inclusive jets to constrain the gluon polarized distribution function at small x, and independent event plane reconstruction for collective flow studies in heavy-ion collisions. The forward upgrade project also facilitates the transition of the STAR detector systems in preparation for an electron-ion collider.

The major components of the forward upgrade project are the Forward Calorimeter System (FCS) and the Forward Tracking System (FTS). This chapter mainly discusses the FCS design and performance studies.

5.1 FCS design specifics

The Forward Calorimeter System will be located on the west side of the STAR detector replacing the current FMS. FCS is designed to be a longitudinally segmented, compensating calorimeter system. It is divided into two sections along the beam direction, a compact Electro-Magnetic Calorimeter (EMCAL) followed by a Hadronic Calorimeter (HCAL). Figure 5.1 shows the geometry of the FCS as defined in the GSTAR simulations. Figure 5.2

shows the location of the FCS within STAR.

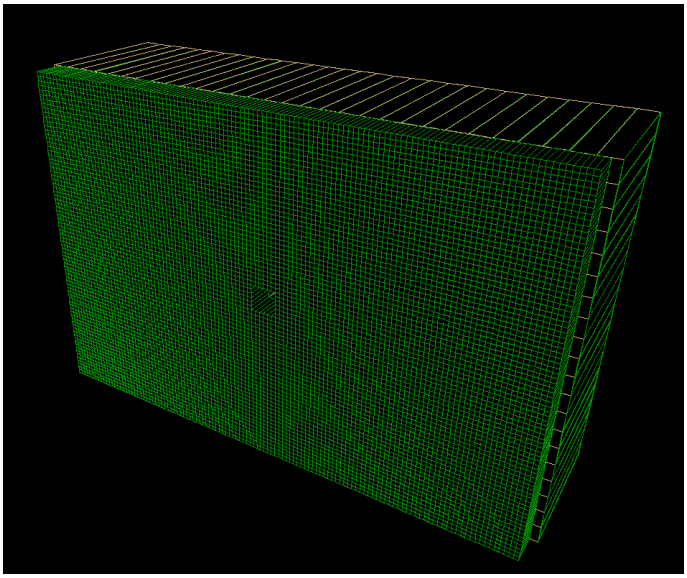

Figure 5.1: FCS geometry used in simulations. Front: EMCAL. Back: HCAL

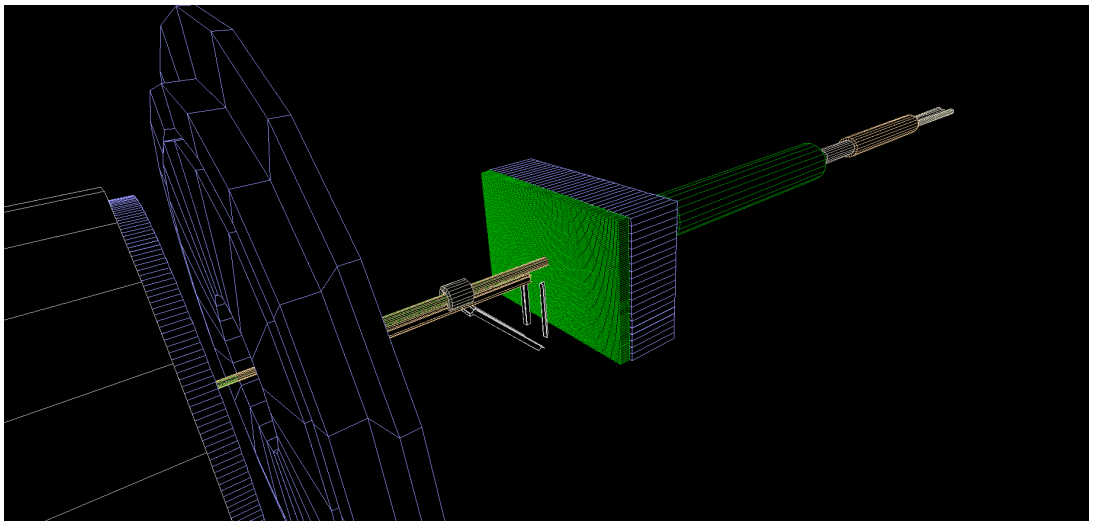

Figure 5.2: FCS within the STAR detector system

The EMCAL consists of 9600 2.6 cm x 2.6 cm x 17 cm towers made with tungsten powder and scintillating fibers. Each tower has 780 fibers, 0.047 cm in diameter. The effective radiation length of the material is $\sim$ 7 mm. Figure 5.3 shows the layout of a single EMCAL tower. The straight fiber design was derived from the Spaghetti Calorimeter (SPACAL) prototype developed by the LAA project at CERN [67]. Compared to the usual

absorber + scintillator tile sandwich type of configuration, thin fibers embedded in absorber could achieve low sampling fractions while maintaining high sampling frequency. The former condition is an important design requirement for compensating calorimeters, namely equal responses of the detector to EM showers and to hadronic showers [68]. High sampling frequency guarantees that the detector still maintain good energy resolution for EM showers. Hadronic showers will penetrate the EMCAL and continue its development in the HCAL, so the overall compensation condition drives the design requirements of both EMCAL and HCAL.

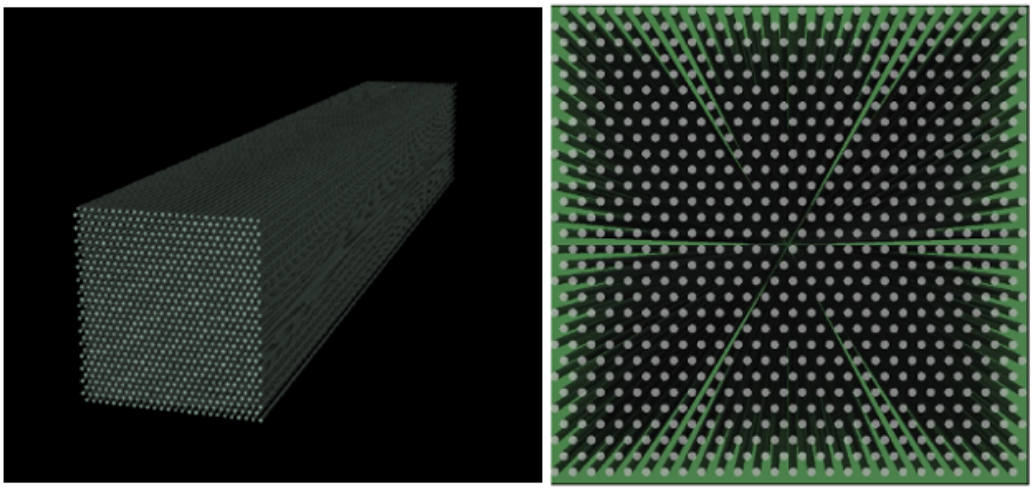

Figure 5.3: A single EMCAL tower of the FCS

A prototype of 4x4 EMCAL tower array was built in 2012 and taken to a test-beam experiment at Fermilab. The energy resolution for electrons and the scintillating light yield were measured. Figure 5.4 shows the measured energy resolution and the expected resolution from simulation as a function of incident electron energy.

The measured electron energy resolution is $\frac{\sigma_E}{E} = \frac{12.0\%}{\sqrt{E}} + 1.4\%$

The design of the HCAL is mainly driven by the compensation requirement and cost considerations. It adopts the same general configuration as the ZEUS prototype hadronic calorimeter [69]. The dimension of each HCAL tower is 10 cm x 10 cm x 91 cm, equivalent to 4 nuclear interaction length. It consists of 64 alternating layers of scintillator tiles and lead absorbers. The thickness of the lead absorber (1 cm) and scintillators (0.25 cm) are

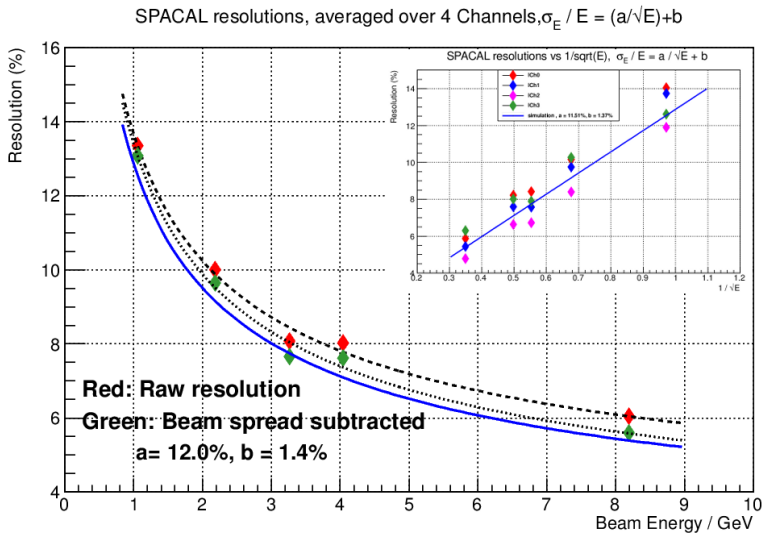

Figure 5.4: Energy resolution of a 4x4 EMCAL prototype measured in a test-beam experiment. Blue line: simulation.

carefully chosen to achieve compensation. A 4x4 tower array of HCAL was built in 2014 with silicon PMT readout. Figure 5.5 shows the detector response and energy resolution of the combined EMCAL and HCAL system to electron and π^- beams.

The measured π^- energy resolution is $\frac{\sigma_E}{E} = \frac{58.0\%}{\sqrt{E}} + 1.5\%$

5.2 EMCAL and HCAL calibrations

The method of calibrating the EMCAL and HCAL has been studied in simulation. The purpose is to examine to what extent the current detector configuration provides equalized responses to EM and hadronic showers, and how to combine signals from EMCAL and HCAL so that the total output is linear in energy and/or achieves the optimal resolution. This inter-calibration procedure is critical for hadron and jet reconstructions.

In general the calorimeter response is defined as the signal per unit incident energy, where the signal could be the charge integrated by a front-end readout system or by the photoelectron yield in the cathode of a photomultiplier tube. For simulation study the calorimeter

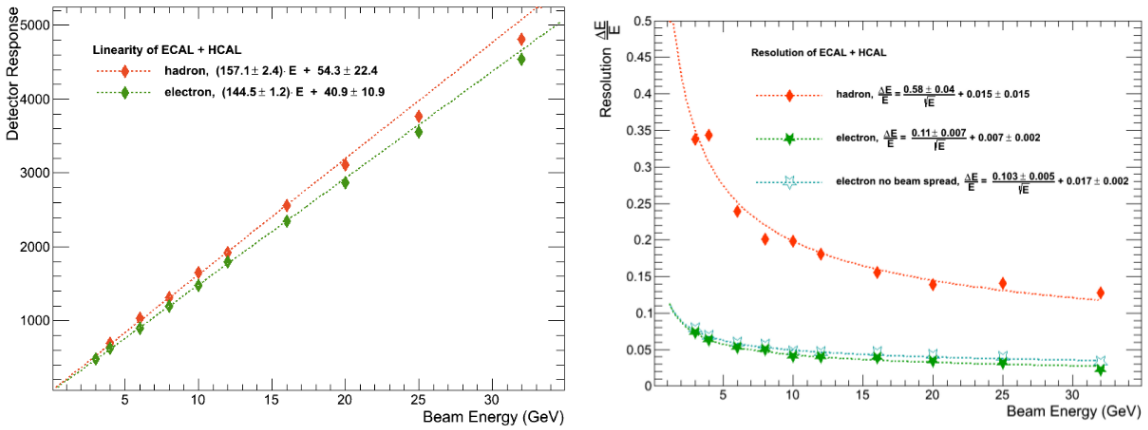

Figure 5.5: Left: Detector response to electron and π^- beams. Right: Energy resolutions for electron and $\pi-$ mesons. Data obtained from test-beam experiment at Fermilab

response is represented by the amount of energy (E_{vis}) deposited in the sensitive volumes (scintillators) of the detector per unit incident energy. In the ideal case, the electronic signal from the readout system will be a linear function of this visible energy E_{vis}. For simple detector configurations such as the HCAL by itself the visible energy is related to the total incident energy via

$$\begin{aligned} E^{e^-}_{vis} &= e_{HCAL} \cdot E^{e^-}_{gen} \\ E^{\pi^-}_{vis} &= h_{HCAL} \cdot E^{\pi^-}_{gen} \end{aligned} \tag{5.1}$$

where e_{HCAL} and h_{HCAL} are the effective sampling fractions of the HCAL for EM showers and hadronic showers respectively, they quantify the EM and hadronic response of the HCAL. Figure 5.6 shows the ratio $E^{e^-}_{vis}/E^{\pi^-}_{vis}$ for the HCAL vs the incident energies of e^- and π^-.

Figure 5.6 indicates that with the default setting of GSTAR hadronic physics routine the HCAL does not sample hadronic showers as efficiently as EM showers. However it should be pointed out that this particular behavior can be tuned in GEANT by changing the minimum energy of the track transport process. Comparisons with the test beam data have to be used to guide the optimization.

For a longitudinally segmented system such as the FCS, care must be taken when combining the calorimeter signals from both sections. The sampling fractions for even the same

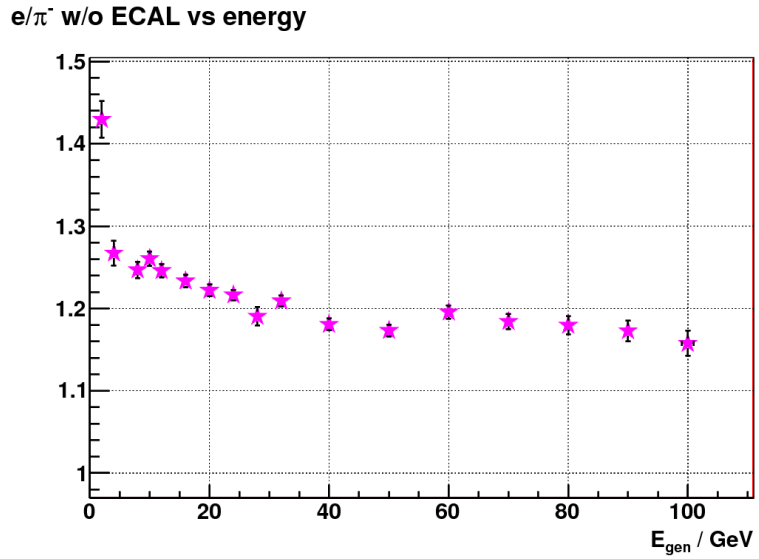

Figure 5.6: Ratio of visible energies of e^- and π^- for the HCAL *vs* incident energy

type of shower could be different between EMCAL and HCAL just because of the different proportions of active detector volumes and absorbers. For this reason the π^- and the e^- signal are defined as the following for FCS:

$$\begin{aligned} E^{e^-}_{gen} &= c_{EMC} \cdot E^{EMC}_{vis} \\ E^{\pi^-}_{gen} &= c_{HCAL} \cdot (E^{EMC}_{vis} + w \cdot E^{HCAL}_{vis}) \end{aligned} \tag{5.2}$$

For EM showers since they are contained in the EMCAL, the calibration constant c_{EMC} is simply the EM sampling fraction of the EMCAL e_{EMC}. The weighting factor w for the HCAL is usually determined by two criteria: 1) achieve optimal energy resolution for hadronic showers and 2) obtain equal responses to electrons and to hadrons, namely $c_{HCAL} = c_{EMC}$. A well designed compensated calorimeter can reach both goals at the same time with w being independent of the incident energy except for low energies ($E < 10GeV$). For the FCS simulation since it is demonstrated that the configuration is not perfectly compensating w is studied under both criteria separately. First of all the part of w that depends on the difference in proportions of the active volumes between EMCAL and HCAL is factored out

$$\pi^- signal = E^{EMC}_{vis} + w \cdot E^{HCAL}_{vis} = E^{EMC}_{vis} + r_0 \cdot \alpha \cdot E^{HCAL}_{vis} \tag{5.3}$$

Where $r_0 = e_{EMC}/e_{HCAL} = 0.96$ is calculated from the responses to electrons by EMCAL and HCAL separately. Responses to minimum ionizing particles such as low energy μ^- gives $r_0 = 0.92$. By definition r_0 indicates the differences in V_{active}/V_{total} where for EMCAL V_{active} is the volume of all the fibers and for HCAL it is the volume of all the scintillating tiles. α encodes the real information on the effectiveness of HCAL at sampling hadronic showers compared to that of EMCAL. α is calculated under the aforementioned two criteria for EMCAL/HCAL inter-calibrations. Figure 5.7 shows an example of minimizing the energy resolution of π^-, and in a different scenario equalizing the responses to e^- and π^-, both done by tuning α to different values.

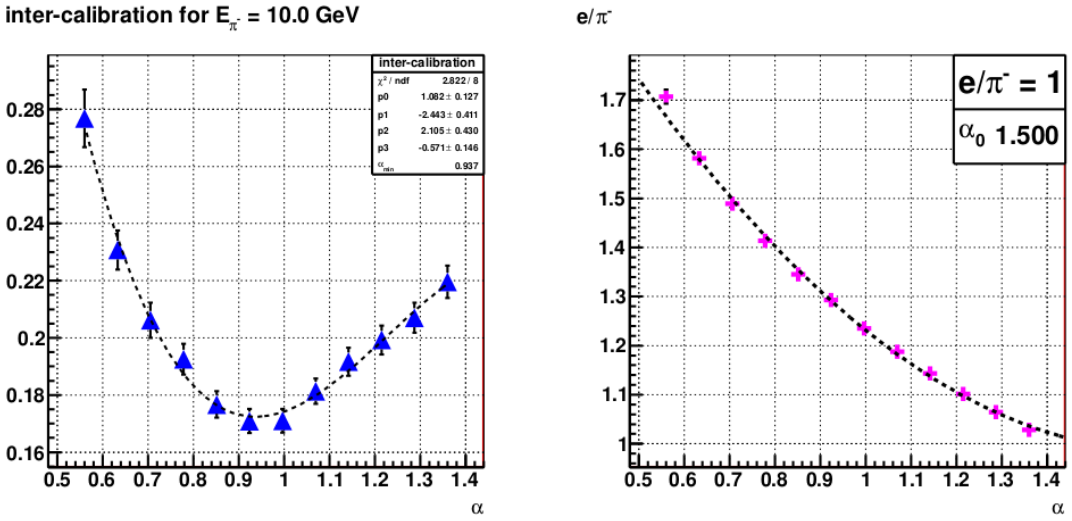

Figure 5.7: Tuning EMCAL/HCAL inter-calibration constants to achieve optimal energy resolutions or equal responses to e^- and π^-

In order to achieve optimal energy resolution or equal responses to e^- and π^- a different value of α is needed. The one that gives best energy resolutions is denoted by α_{min} and the one that provides equal responses is denoted by α_0. Figure 5.8 shows α_{min} and α_0 as a function of the incident energy of the π^-.

So with the default setting of GSTAR one cannot obtain optimal energy resolution and equal e/π responses at the same time. Figure 5.9 shows the energy resolutions of π^- with α_{min} and α_0 calibrations separately.

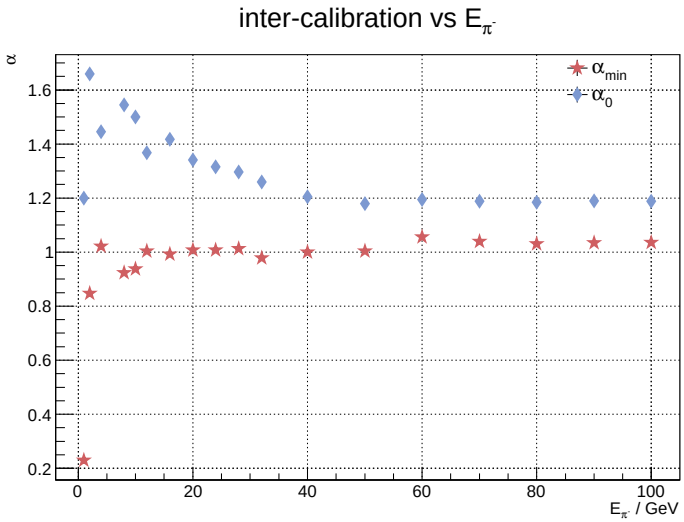

Figure 5.8: α_{min} and α_0 parameters of EMCAL/HCAL inter-calibration as a function of the incident energy of π^-

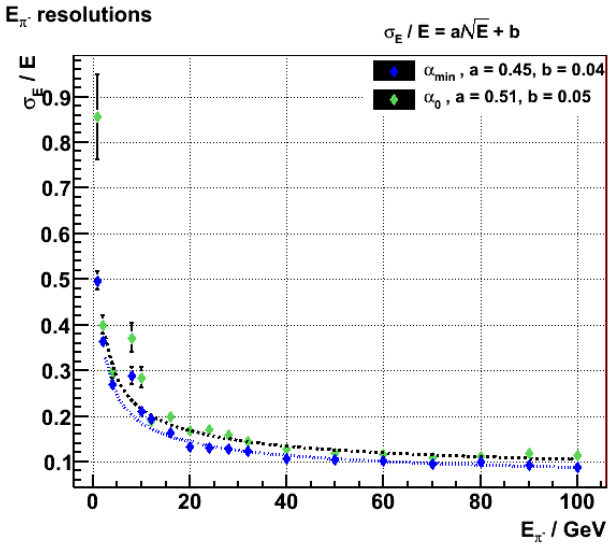

Figure 5.9: Energy resolution for π^- with α_{min} and α_0 calibrations

With the α_{min} inter-calibration the energy resolution is $\frac{\sigma_E}{E} = \frac{45.0\%}{\sqrt{E}} + 4\%$ but this calibration scheme is almost of no practical use since the EM and hadronic showers would need different overall calibration constants, as shown in the left panel of Figure 5.10. With the α_0 inter-calibration one does not have to identify the type of showers since the overall calibration constants are the same for EM and hadronic showers, but as indicated by Figure 5.8 the inter-calibration factor α_{min} might become energy dependent below 40 GeV. The energy resolution of π^- under α_0 calibration is $\frac{\sigma_E}{E} = \frac{51.0\%}{\sqrt{E}} + 5\%$. The α_0 scheme is more practical when calibrating the detector during data taking. The EMCAL can be calibrated by μ^- or electrons. The EMCAL/HCAL inter-calibration constant can be fixed by first looking at μ^- responses to obtain r_0 then making corrections to r_0 to obtain α_0, e.g. by reconstructing ρ^0 through its $\pi^+\pi^-$ decays. If possible, the product $r_0 \cdot \alpha_0$ can also be obtained by exposing EMCAL and HCAL separately to electron beams. For studies presented in the rest of this chapter the α_0 calibration is used.

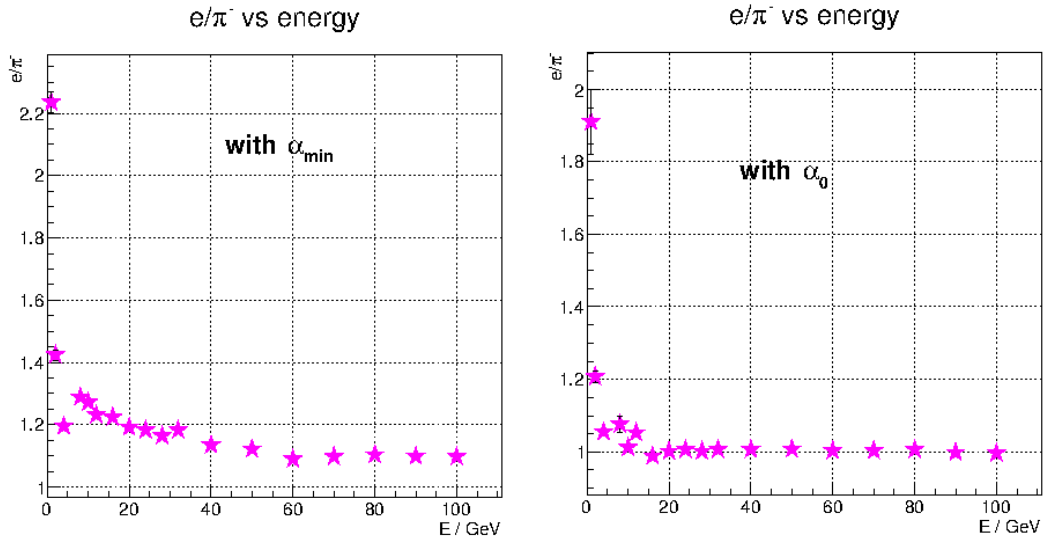

Figure 5.10: Ratio of e^- and π^- responses of FCS under α_{min} and α_0 inter-calibrations.

5.3 Jet resolution

The kinematic coverage and resolution of forward jets in FCS has been studied by PYTHIA + GSTAR simulations in $\sqrt{s} = 200$ GeV proton-proton collisions. One million filtered Monte Carlo events were generated in 4 partonic $\hat{p}_T$ bins ranging from 2 GeV to 32 GeV. All of these events passed a filtering process which requires that there was at least one particle-level jet with $p_T > 1.0$ GeV in the pseudorapidity range $2.0 < \eta < 5.0$. The jets in the filter are reconstructed by applying an anti-k_T algorithm, with the distance parameter $R = 0.7$, to the final-state particles produced in PYTHIA. Detector-level jets are reconstructed by the same jet algorithm on the energies deposited in FCS towers after calibration. Figure 5.11 shows the MC event cross section in these 4 partonic $\hat{p}_T$ bins after normalization. There is an additional requirement that each event has at least a pair of matched particle/detector-level jets. Figure 5.12 shows the cross-section of particle-level and detector-level jets *vs* jet p_T within pseudorapidity range $2.8 < \eta_{particlejet} < 4.0$. The yield of detector-level jets is significantly higher than that of particle-level jets at high p_T due to the bin-migration effect discussed in the previous chapter.

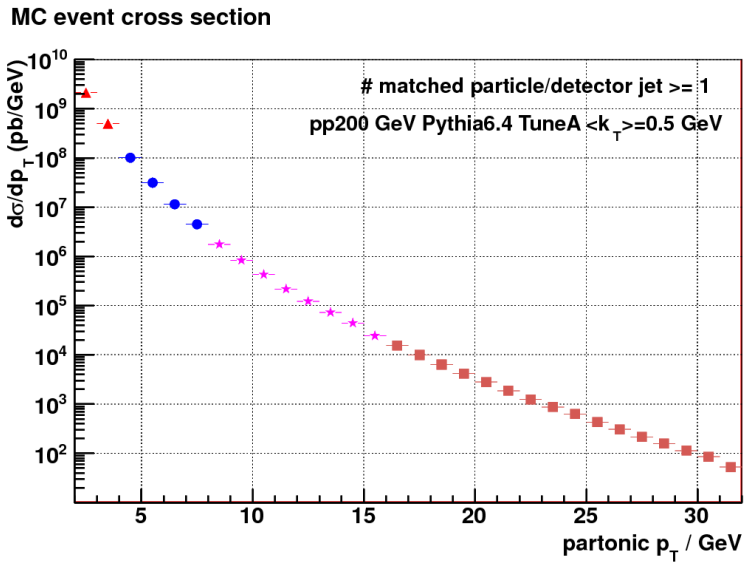

Figure 5.11: The cross-section of MC events containing at least one pair of matched particle-detector level jets *vs* partonic $\hat{p}_T$. Events in 4 partonic $\hat{p}_T$ bins were generated separately in PYTHIA before normalization and are color-coded differently.

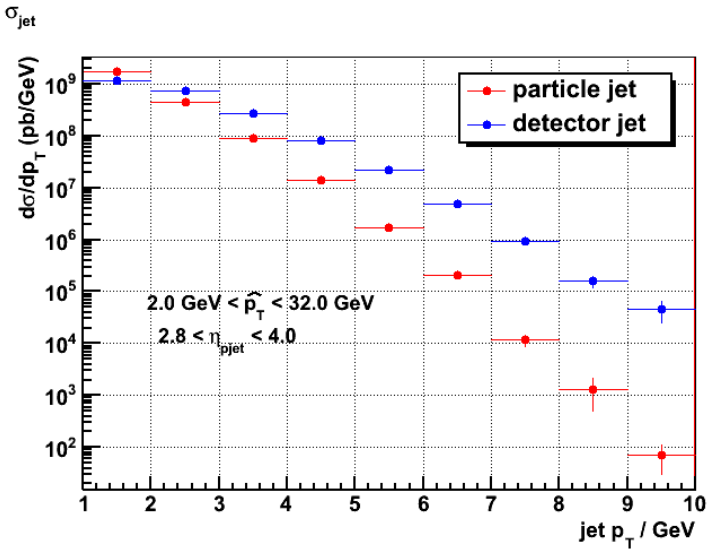

Figure 5.12: Cross-sections of particle-level and detector-level jets *vs* particle jet p_T

To calculate the jet energy and the p_T resolution, a detector jet is matched to the closest particle jet in pseudorapidity η and azimuthal angle ϕ within $R_{match} < 0.5$ ($R_{match} = \sqrt{\Delta\eta^2 + \Delta\phi^2}$). In order to reduce the probability of mismatched particle/detector jet pairs the p_T of any non-leading jet in the event is required to be less than 25% of the leading jet under study. Before computing the energy resolution one needs to make sure the energy scales of the reconstructed detector jets are correct, i.e. the same as its matched particle jet. However as shown in Figure 5.13 the constant overall calibration factor ($c_{EMC} = c_{HCAL}$) and the EMCAL/HCAL inter-calibrations derived from the previous section did not put the energy scale of the detector jet at the correct place. This is due to the energy dependence of α_0 shown in Figure 5.8. The inter-calibration was chosen to be a constant 1.18 which is correct for E > 40 GeV, but as typical jets contain many low energy hadrons α_0 needs to increase for E < 40 GeV in order to maintain the same detector responses to both EM showers and hadronic showers. Therefore $\alpha_0 = 1.18$ will under-estimate the overall energy scale of the detector jets.

A practical method of correcting the energy scale of the reconstructed detector jets was developed. The correction is derived from comparing a closely matched pair of particle jet and detector jet and is expressed in terms of reconstructed variables only, namely the energy

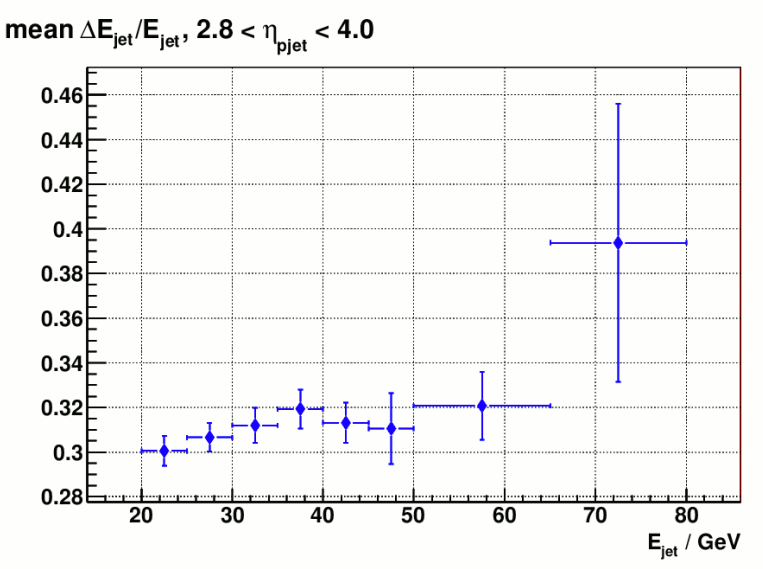

Figure 5.13: $(E_{particle\,jet} - E_{detector\,jet})/E_{particle\,jet}$ *vs* particle jet energy

and pseudorapidity of the detector jet. In this way the correction scheme can be directly applied to real data. The pair of particle and detector jets used in computing the corrections are selected with the following criteria

$$\begin{aligned} p_{T,\,non-leading\,jet} &< 0.25 \cdot p_{T,\,leading\,jet} \\ R_{match} &< 0.2 \\ 20GeV &< E_{particle\,jet} < 80GeV \\ 2.8 &< \eta_{particle\,jet} < 4.0 \end{aligned} \tag{5.4}$$

In order to reduce the resolution effect which generates bin-migrations the jet energy corrections are initially calculated in each particle jet energy and pesudorapidity (η) bin before being projected into the detector jet energy and η bins. The weighted average of the set of correction factors within the same detector jet bin is calculated and serves as the energy scale correction for that particular bin. Figure 5.14 shows an example of calculating the correction factor for a single particle jet (E, η) bin and the distribution of the matched detector jet (E, η). The count of detector jets in each ($E_{detector\,jet}$, $\eta_{detector\,jet}$) bin are used as weights when calculating the average correction factors. Figure 5.15 shows the correction

factors derived for each ($E_{detector\,jet}$, $\eta_{detector\,jet}$) bin.

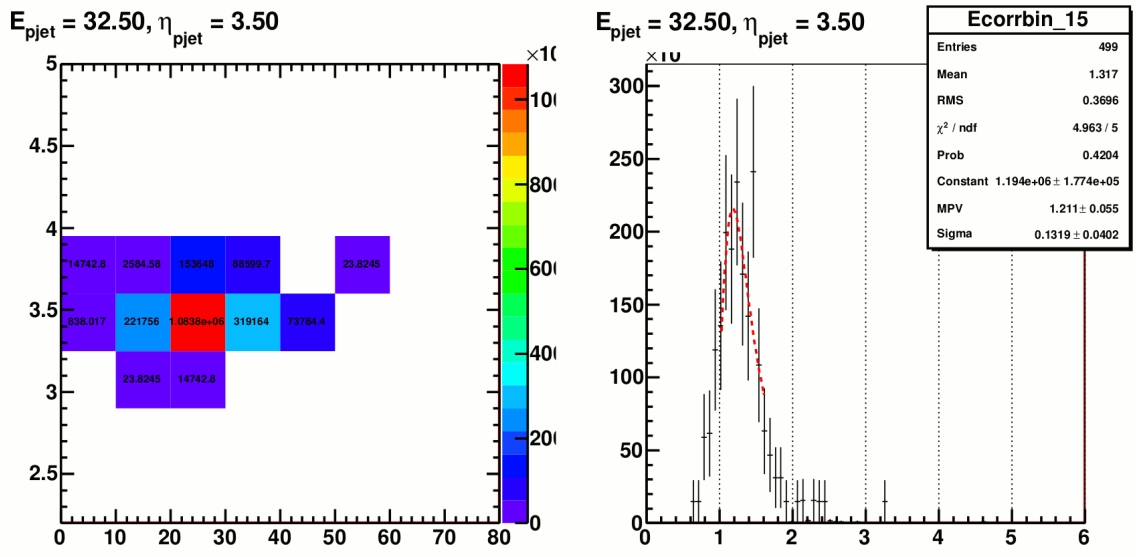

Figure 5.14: Right: Calculate jet energy scale correction for a single ($E_{particle\,jet}$, $\eta_{particle\,jet}$) bin. Left: the ($E_{detector\,jet}$, $\eta_{detector\,jet}$) distribution of the matched detector jet, the counts in each bin are used as weights when calculating the average correction factors for that bin.

With these corrections the energy scale of the detector jets is now consistent with the particle jets, as shown in Figure 5.16. Figure 5.17 shows the jet energy and p_T resolutions after the correction. The jet position resolutions are also calculated as the difference in η and ϕ between matched particle/detector-level jets. Figure 5.18 shows an example of $\Delta\eta$ and $\Delta\phi$ distributions. Note that the physical boundary of FCS is $\eta\sim2.6$ at top and bottom and $\eta\sim2.2$ at left/right sides, therefore without the $2.8 < \eta_{pjet} < 4.0$ cut on the pseudorapidity of the particle jets the $\Delta\eta$ distribution is skewed on the negative side. Figure 5.19 shows the the widths of the $\Delta\eta$ and $\Delta\phi$ distributions as a function of the particle jet p_T.

5.4 Hadron-jet correlation measurement with FCS

The Collins asymmetry measured via hadron-jet correlations in the forward rapidity could provide unique access to proton transversity in the kinematic regions not well constrained by previous SIDIS measurements. Figure 5.20 shows the theory predictions for π^0 and

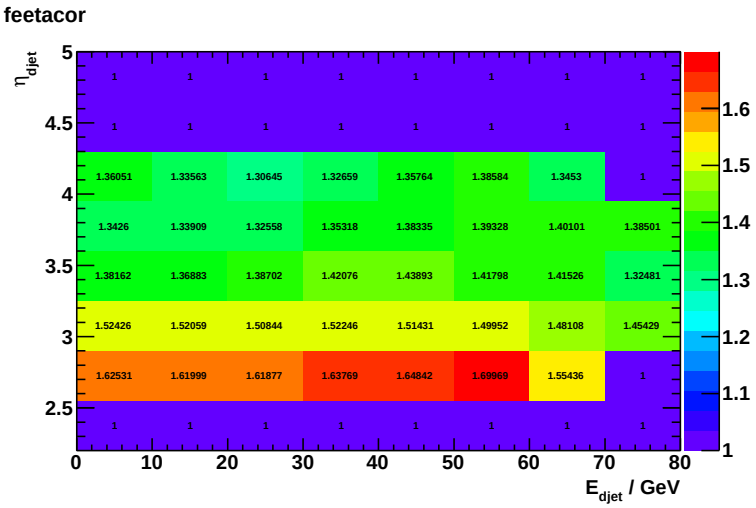

Figure 5.15: Jet energy scale correction *vs* ($E_{detector\,jet}$, $\eta_{detector\,jet}$)

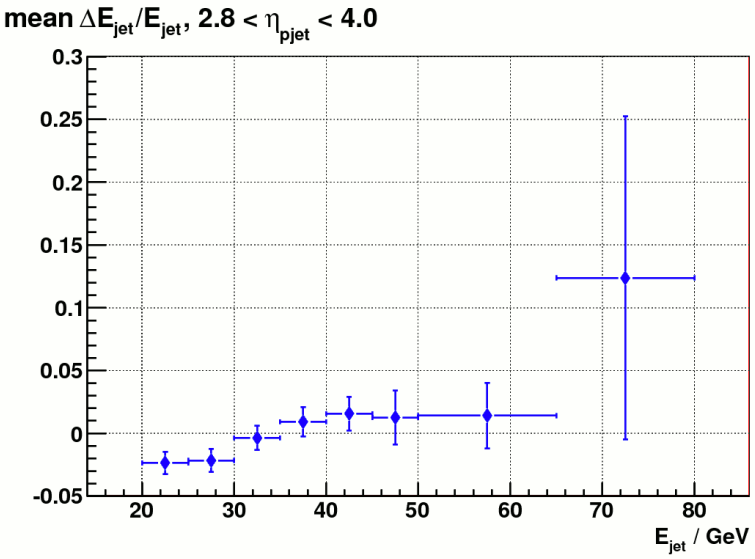

Figure 5.16: $(E_{particle\,jet} - E_{detector\,jet})/E_{particle\,jet}$ *vs* particle jet energy after jet energy scale corrections

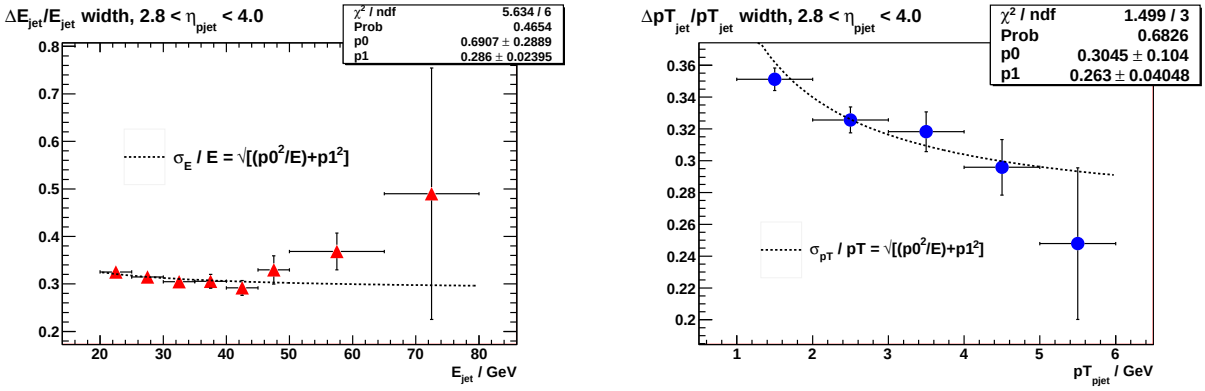

Figure 5.17: Jet energy and p_T resolutions. Left: energy resolution. Right: p_T resolution

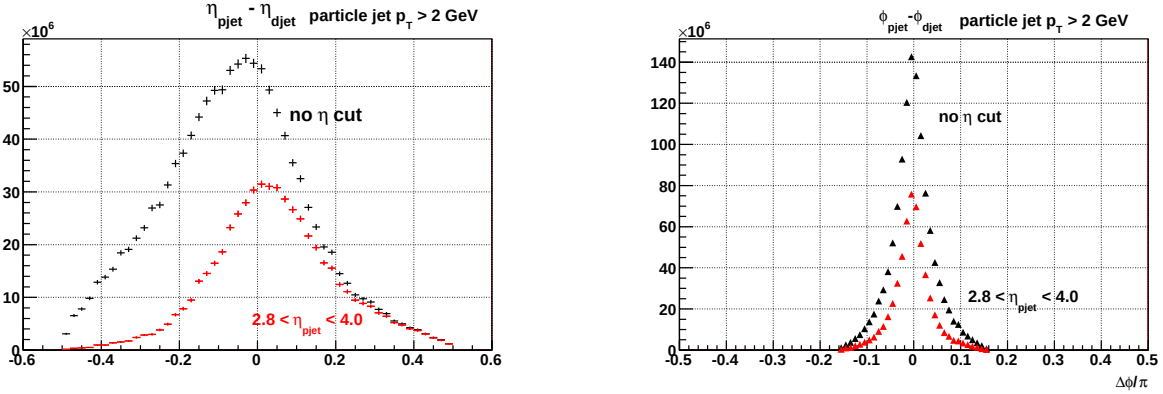

Figure 5.18: η and ϕ resolutions of FCS jets with $p_T > 2$ GeV

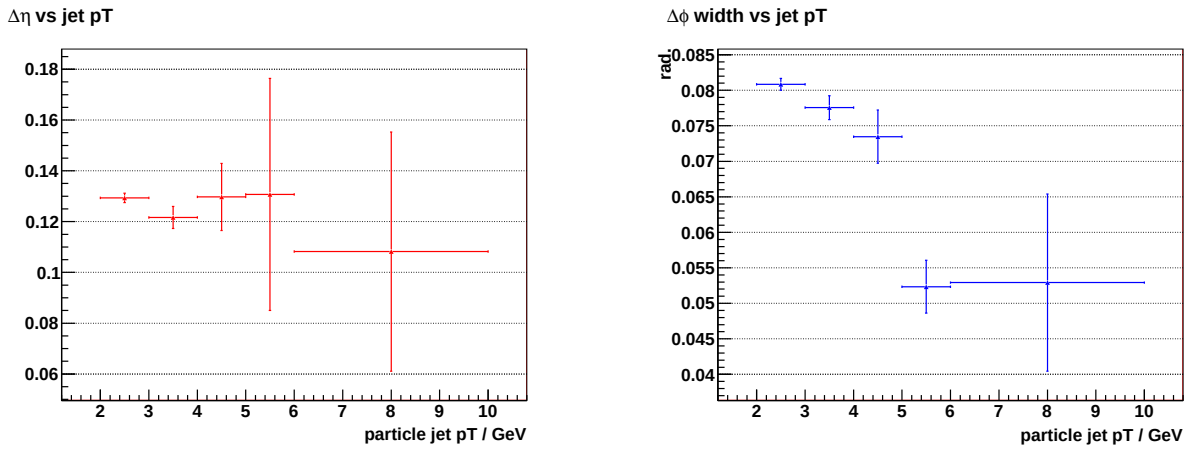

Figure 5.19: Width of $\Delta\eta$ and $\Delta\phi$ distributions *vs* particle jet p_T

$\pi^{\pm}$ Collins asymmetries in 200 GeV polarized proton proton collisions, where the proton transversity and the Collins fragmentation function are extracted from two different sets of SIDIS measurements [28]. The region to the left of the vertical dashed line are covered by the kinematic reach of the SIDIS data while the right side of the vertical dashed line with $p_{jT} > 2.5$ GeV is unconstrained. It is clear that different parameterizations of the two SIDIS data set presents very different behavior in the unconstrained region.

The Collins angle resolutions for π^0 and $\pi^{\pm}$ have been studied in simulation. For the case of $\pi^{\pm}$ perfect particle identification was assumed while in practice without a PID detector only the asymmetries for positvely and negatively charged hadrons can be measured. The charge sign separation will be provided by the Forward Tracking System. Charged hadrons are reconstructed by the same clustering algorithm as the FMS π^0 analysis. For each cluster in the HCAL the overlapping EMCAL clusters are found by searching in the circular area with a radius of four times the width of the EMCAL towers around the center of the HCAL cluster. Then the energies of the HCAL cluster and the overlapping EMCAL clusters are combined and the centroid re-calculated. In the simulation, the combined cluster is required to be matched to a generated $\pi^{\pm}$ in PYTHIA and is an integral component of a detector jet that has been associated to a particle-level jet as well. The Collins angles are then calculated from the generated $\pi^{\pm}$ inside the particle jet and the reconstructed cluster within

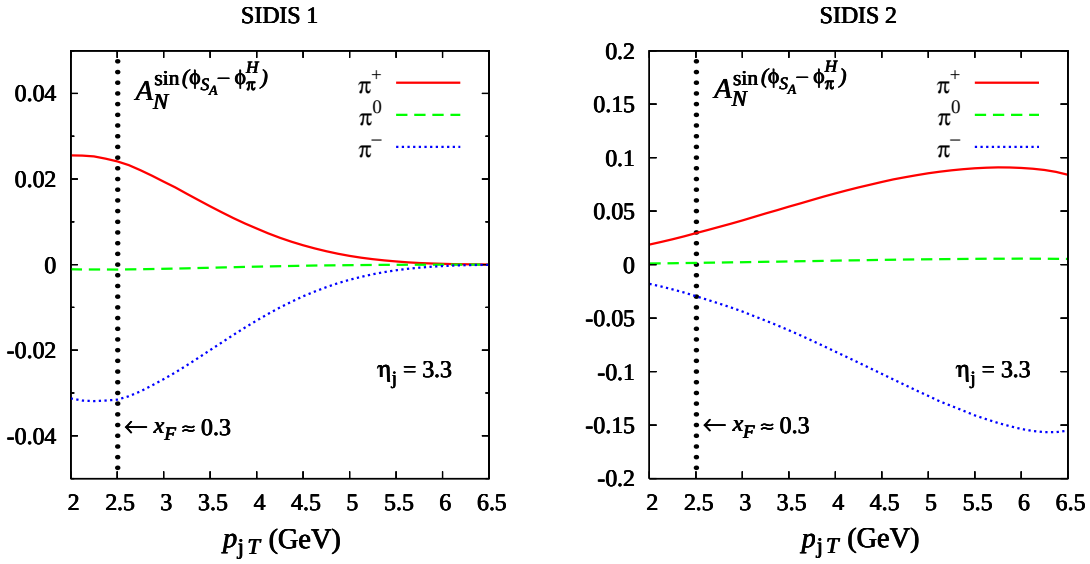

Figure 5.20: The estimated quark Collins asymmetry for the $p^\uparrow$ + p→jet + π + X process, obtained by adopting the parameterizations of SIDIS 1 (left panel) and SIDIS 2 (right panel) dataset respectively, at $\sqrt{s}$ = 200 GeV c.m. energy in the forward rapidity region and as a function of the jet transverse momentum p_{jT}, from p_{jT} = 2 GeV up to the maximum allowed value. Notice the difference in scale between the two panels. The dotted black vertical line delimits the region beyond which the SIDIS parameterizations for the quark transversity distribution are presently plagued by large uncertainties. Similar results are obtained when considering different c.m. energies. [28]

the detector jet respectively. The difference in generated and reconstructed Collins angle is shown in Figure 5.21

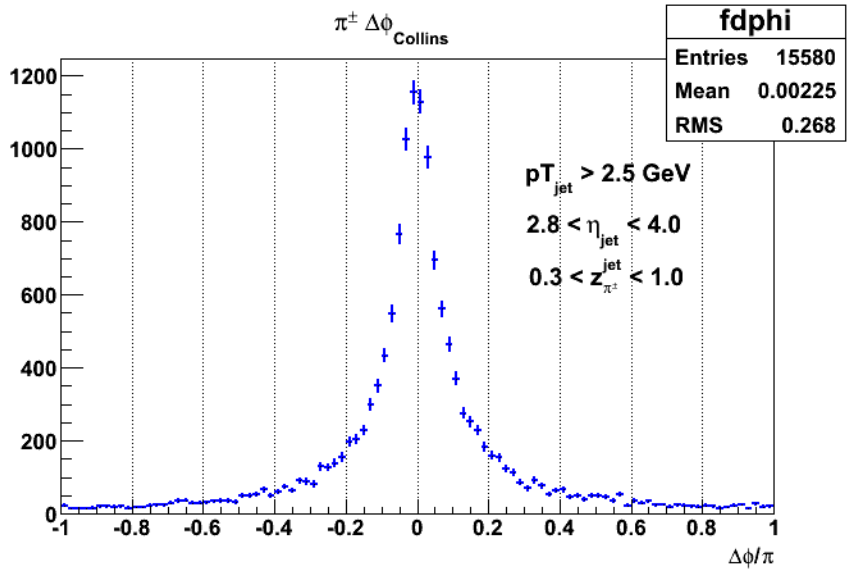

Figure 5.21: Difference between generated and reconstructed Collins angles from $\pi^{\pm}$ and jets in FCS. Simulation of $\sqrt{s} = 200$ GeV proton-proton collisions generated by PYTHIA + GSTAR

For the π^0 Collins angle resolution a pair of clusters found on the EMCAL are required to be matched to the daughter photons of a generated π^0 in PYTHIA. The generated π^0 must be in a particle jet to which there exists an associated detector jet. Figure 5.22 shows the mass distribution of a pair of clusters found in the EMCAL of FCS, and the mass of the pairs which are matched to generated π^0. Figure 5.23 shows the difference between the generated and reconstructed π^0 Collins angles. The accuracy of reconstructing the longitudinal momentum fraction (z) of the π^0 with respect to the jet is also studied, as shown in Figure 5.24. The z distribution of the generated π^0 and the reconstructed π^0 before and after jet energy scale correction are compared. It indicates again that correcting the jet energy scale is important for jet-related measurements.

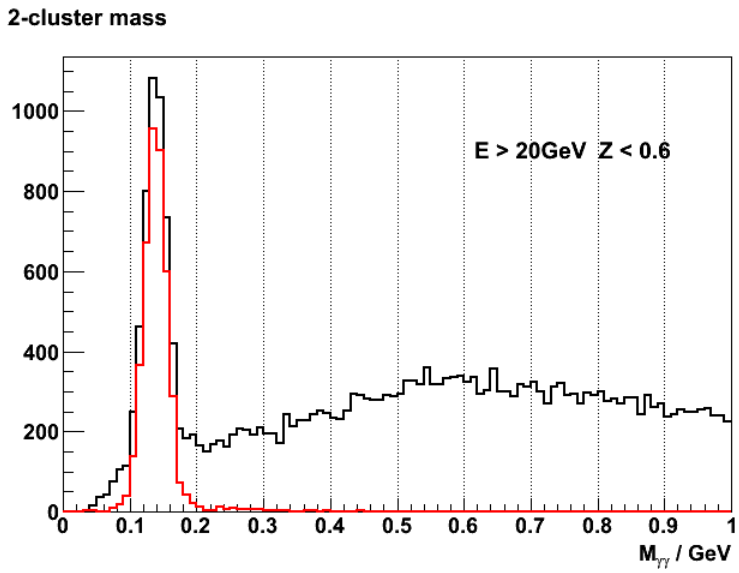

Figure 5.22: Black: The mass distribution of pair of clusters found in the EMCAL of FCS. Red: The masses of the pairs matched to a generated π^0

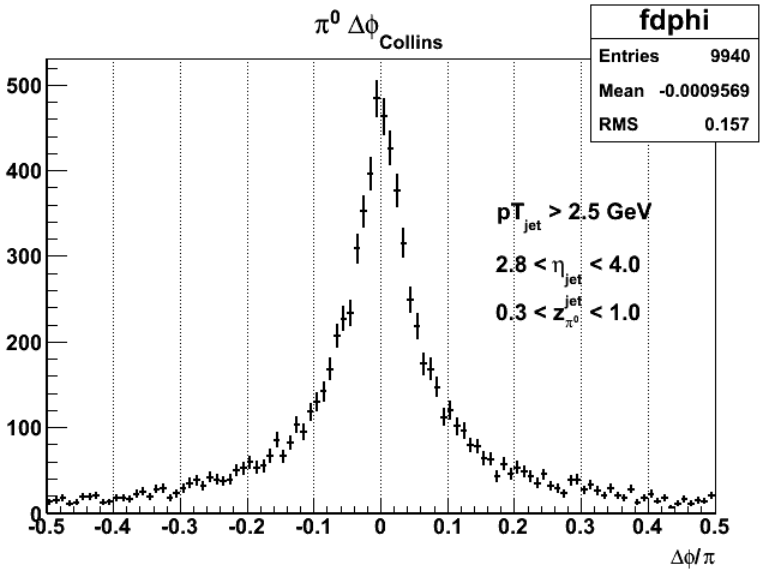

Figure 5.23: Difference between the generated and reconstructed Collins angles from π^0 and jets in FCS.

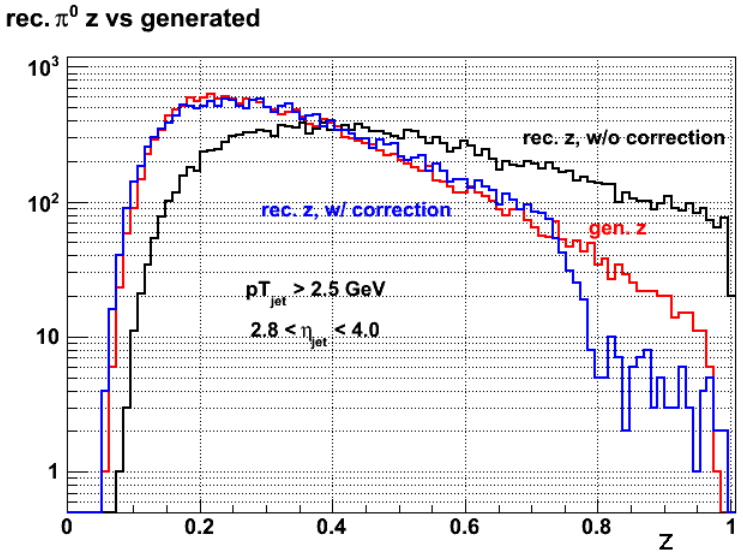

Figure 5.24: Distributions of π^0 longitudinal momentum fractions z. Red: generated π^0. Black: reconstructed π^0 without jet energy scale correction. Blue: reconstructed π^0 with jet energy scale correction.

5.5 Prompt photon measurement

Photons emerging from partonic hard-scatterings carry important information on the initial-state parton distributions in the proton or the heavy nucleus being probed. With the absence of final-state hadronic interactions prompt photon serves as a clean channel for studies such as proton's Sivers function [70] and the Color Dipole dipole gluon distributions of heavy nuclei at low-x [71]. At the Leading Order of QCD, prompt photons are generated through quark-antiquark annihilation $q\bar{q} \to \gamma$ and QCD Compton scattering $qg \to q\gamma$ with no fragmentation stage. At Next-to-Leading Order there are photons produced from the initial- and final-state radiations that need to be included to account for the experimentally measured photon cross sections.

The experimental signature of prompt photon production is an isolated photon with little or no activity in its neighborhood. The effectiveness of suppressing non-prompt photon background by placing isolation cuts in the FCS has been studied in simulation. An isolation cut of r_{iso} requires no extra clusters/photons found within the radius r_{iso} around the primary

photon. Different isolation cuts are investigated and the efficiencies of these cuts at retaining prompt photon signal and rejecting backgrounds are shown in Figure 5.25

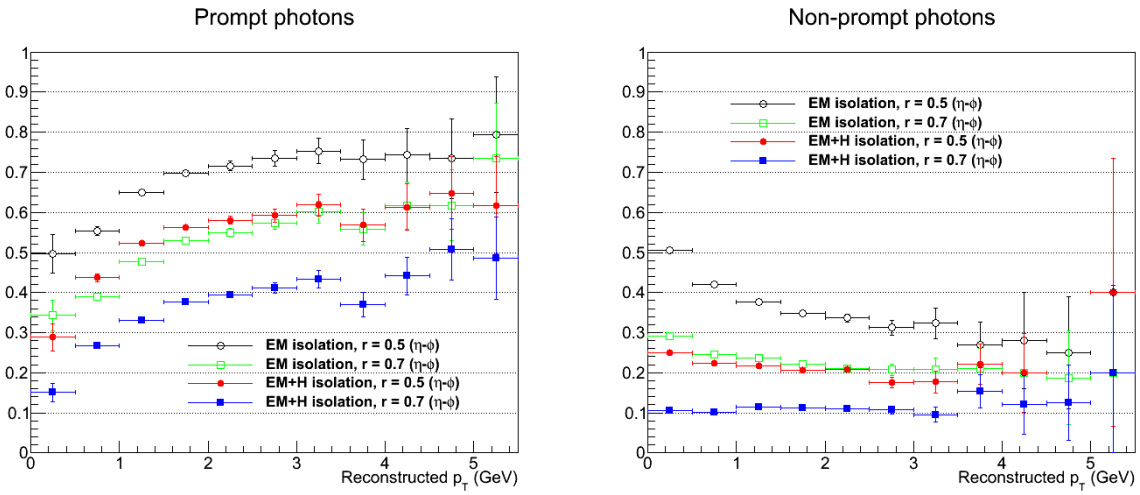

Figure 5.25: Fractions of prompt photon signal and background events passed the isolation cuts. EM isolation: isolation cuts applied to EMCAL only. EM+H isolation: cuts applied to both EMCAL and HCAL.

The signal-to-background ratio obtained with a particular isolation cut is given by

$$SB(r_{iso}) = \frac{N_{sig} \cdot R_{sig}(r_{iso})}{N_{bkg} \cdot R_{bkg}(r_{iso})} = SB(0) \cdot \frac{R_{sig}(r_{iso})}{R_{bkg}(r_{iso})} \tag{5.5}$$

where $SB(0)$ is the ratio of prompt photon events to background events without isolation cuts, i.e. as generated. $\frac{R_{sig}(r_{iso})}{R_{bkg}(r_{iso})}$ represents the discriminating power of the isolation cut r_{iso} and is calculated by taking the ratio of the signal and background efficiencies shown in Figure 5.25. The discriminating power against all types of background is shown in the left panel of Figure 5.26. In particular the discriminating power against the photon background from π^0 decays is shown in the right panel of Figure 5.26.

The improvement on the signal to background ratio by placing the isolation cut on FCS can be as large as a factor of 4 at $p_T \sim 3$ GeV. The effect is much greater for the case of π^0 background. The statistical uncertainties of prompt photon asymmetry measurement is calculated from the prompt photon yield and the signal to background ratios as shown above. The prompt cross section is taken from NLO pQCD calculations (by W.Vogelsang

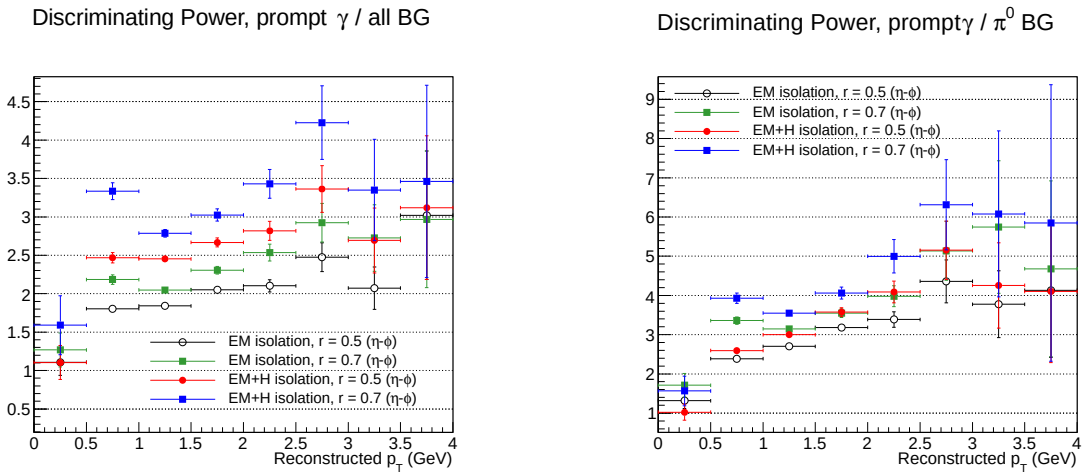

Figure 5.26: Left: Discriminating power of different isolation cuts against all types of backgrounds. Right: Discriminating power of the same cuts against π^0 background.

et.al. [61]) as shown in Figure 5.27

Figure 5.28 shows the projected statistical uncertainty of prompt photon single spin asymmetry measurement in $\sqrt{s} = 200$ GeV proton proton collisions with integrated luminosity $\mathcal{L}$ = 100 pb^{-1} and average beam polarization of 60%.

5.6 Drell-Yan measurement

Drell-Yan (DY) process refers to the production of virtual photons via $q\bar{q} \rightarrow \gamma^*$ and $qg \rightarrow q\gamma^*$ followed by the decay of the virtual photon to e^+e^- or $\mu^+\mu^-$. Compared to prompt photon production, the Drell-Yan process is better understood in theory, e.g. Drell-Yan cross section can be calculated up to NNLO [72] and the TMD factorization is proven for Drell-Yan production [73]. The isolation cuts needed for prompt photon detection bear significant complications for comparisons between experimental data and theoretical calculations. The definition of prompt and non-prompt components of photon production becomes ambiguous beyond leading order. On the contrary the Drell-Yan signal is clearly defined in theory. The difficulty associated with Drell-Yan measurement is its small production cross section and the requirement for particle identification. The detection capability for Drell-Yan signals via

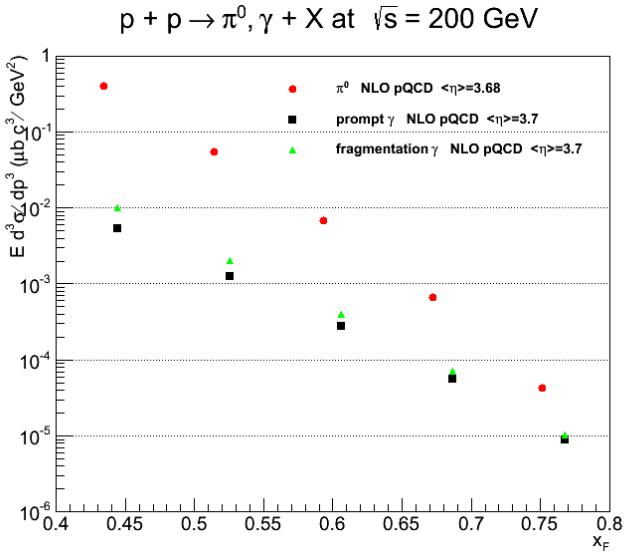

Figure 5.27: Prompt photon cross section calculated by NLO pQCD theory

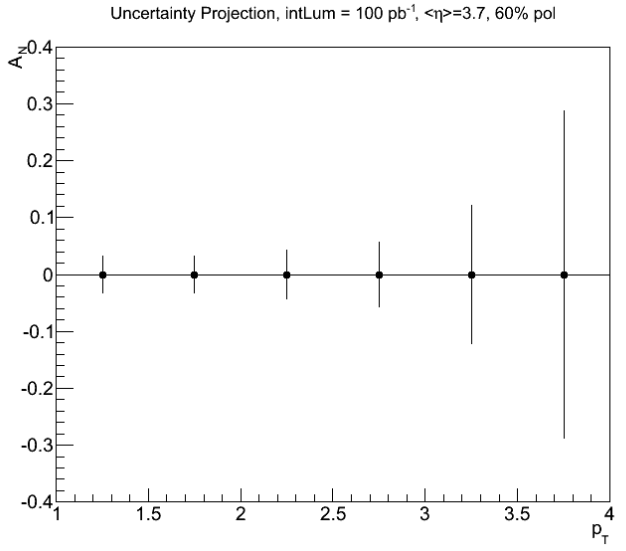

Figure 5.28: Statistical uncertainty of prompt photon A_N measurement with FCS. $\sqrt{s} =$ 200 GeV proton proton collisions with integrated luminosity $\mathcal{L} = 100\ pb^{-1}$ and average beam polarization of 60%.

the di-electron channel has been studied in simulation with the FCS + FTS setup.

The biggest challenge of DY measurements is to suppress the overwhelming hadronic background. The total DY production cross section is on the order of $10^{-5} \sim 10^{-6}$ of that for the hadron production. Therefore the probability of misidentifying a hadron track as a e^+ or e^- track has to be suppressed down to the order of 0.1% while maintaining reasonable electron detection efficiencies. To that end, the combined electron/hadron discriminating power of the proposed FCS and FTS has been studied. By applying multivariate analysis techniques to the features of EM and hadronic shower development and using the momentum measurements from the FTS, one can achieve hadron rejection power of 200 to 2000 for hadrons ranging from 15 GeV to 50 GeV with 80% electron detection efficiency. The hadron rejection power is parameterized as a function of the hadron energy and pseudorapidity and has been used in a fast simulation to estimate the DY signal to background ratios.

To discriminate an EM shower from a hadronic shower, three FCS-related observables are used. They are defined as follows:

1. Eratio: the ratio of a 5x5 (towers) EMCAL cluster energy to the sum of the energies of the same 5x5 EMCAL cluster and the associated 5x5 HCAL cluster.

2. Swidth: the effective EMCAL shower width $R_p = \sum_i r_i E_i^{0.4} / \sum_i E_i^{0.4}$ where r_i is the distance of the ith tower to the centroid of a 5x5 EMCAL cluster, E_i is the energy of that tower. The summation is over the 25 towers in the 5x5 EMCAL cluster around the highest tower.

3. NTratio: the number of EM towers with energies above 100 MeV divided by the total number of EMCAL and HCAL towers above the same threshold. All of the towers come from a pre-defined 5x5 EMCAL cluster around the highest tower and the corresponding 5x5 HCAL cluster.

Figure 5.29 shows the distribution of these three variables for 30 GeV electrons and π^- respectively.

The FTS helps rejecting hadrons by measuring the track momentum. The ratio of the energy deposit in EMCAL to track momentum (E/P ratio) provides additional information

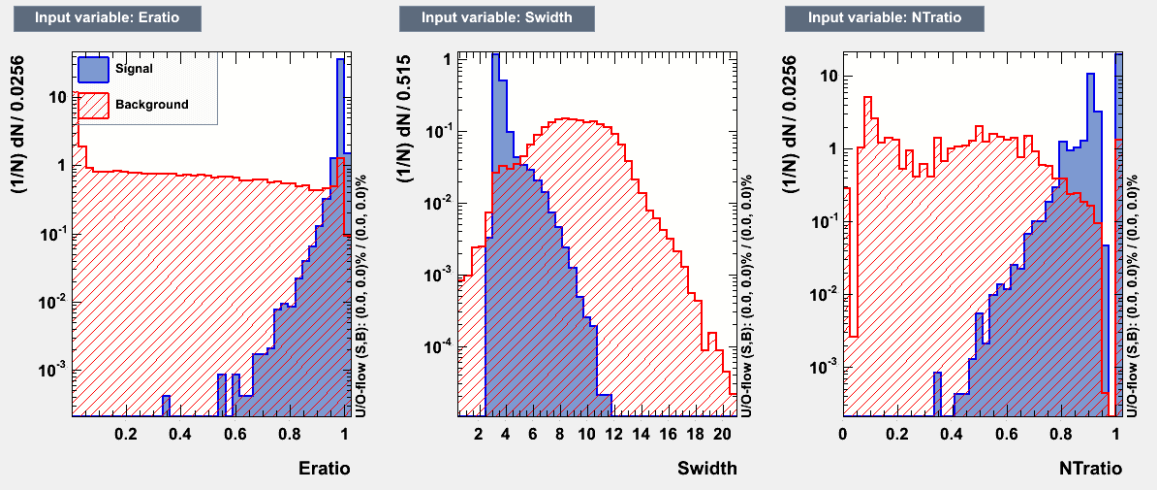

Figure 5.29: Eratio, Swidth and NTratio distribution for 30 GeV electrons (signal) and π^- (background).

in separating $e^{\pm}$ from charged hadrons. The momentum resolution is evaluated by a standalone parameterized simulation of the Forward Tracking System with typical expected hit resolution of a silicon detector. The momentum resolution is parameterized as a function of the track energy and pseudorapidity. Figure 5.30 shows the parameterized momentum resolution at $\eta = 2.5$ and 4.0. Figure 5.31 shows the ratio E/P for 30 GeV electrons and π^-.

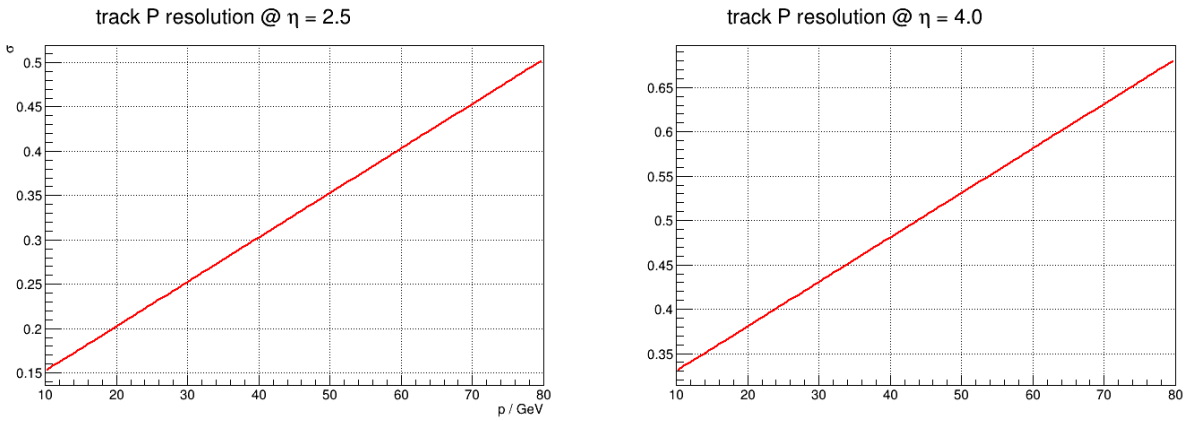

Figure 5.30: Expected track momentum resolution of the forward tracking system from simulations.

These observables from the FTS and FCS have been used as inputs to a Boosted Decision Trees (BDT) algorithm. The BDT contains 1000 binary decision trees each has a depth of 4

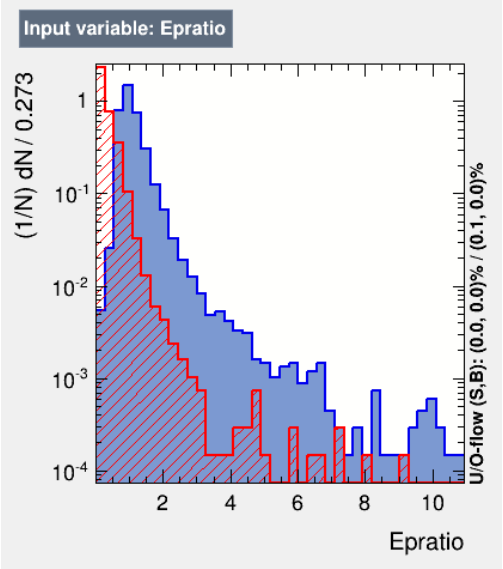

Figure 5.31: E/P ratio distribution for 30 GeV electrons (blue) and π^- (red).

and corresponds to a particular partition of the 4-dimensional feature space into signal-rich (electron) and background-rich (hadron) regions. They are trained sequentially using half of the e^- and π^- samples generated. Misidentified tracks from the previous decision trees are given a higher weight in training the subsequent trees. In the end each decision tree is given an index representing its performance during the training. In the validation stage the decision of each track's type is made based on the collective responses of all of the decision trees, with each of their responses weighted by the performance index. The boosting algorithm takes advantage of using not only the discriminating power of each single observable but also the correlations among them. Figure 5.32 shows electron/hadron (e/h) discriminating power as derived from the BDT algorithm, with 80% electron detection efficiency.

To estimate the DY signal to background ratio, the e/h discriminating power has been parameterized as a function of the track energy and pseudorapidity as shown in the right panel of Figure 5.32. 4 billion PYTHIA proton-proton collision (pp) events at $\sqrt{s} = 200$ GeV are generated with the minimum partonic $\hat{p_T} = 3$ GeV/c and a forward filter requiring a total $p_T > 3$ GeV in any of the four jet-patch-like regions within $2.5 < \eta < 4.0$. All basic QCD 2→2 scatterings as well as heavy flavor channels were enabled. As a reference, note that a luminosity of $\mathcal{L} = 2.5\ pb^{-1}$ for $p + Au$ collisions is equivalent to 500 pb^{-1} for $p + p$

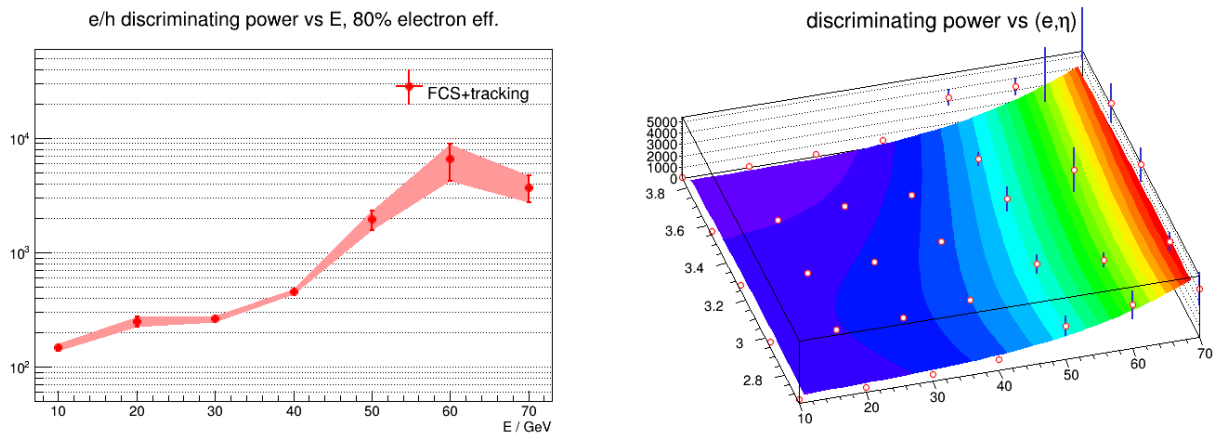

Figure 5.32: Electron/hadron discriminating power derived from FCS + FTS simulations. Left: e/h *vs* energy. Right: e/h *vs* energy and pseudorapidity. The parameterized 2-D function is also shown in the right panel.

, which corresponds to 240.5 billion pp events with the above setting. The DY productions through $q\bar{q}$ annihilation and qg scattering processes were separately generated and scaled to 500 pb^{-1}.

The left panel of Figure 5.33 shows the yield of the track pairs from the QCD background sample with the proposed cuts applied cumulatively to illustrate the background reduction process. The final background yield from the 4 billion sample after γ/neutron removal + track energy cuts + charge sign requirement and e/h discrimination are shown by the green points. The right panel of Figure 5.33 shows the accumulative background reduction factor after applying the cuts progressively.

The final background yield as a function of pair mass is then fitted by an exponential function and rescaled to a total luminosity of 500 pb^{-1}. The left panel of Figure 5.34 shows the normalized background yield along with the expected DY production. The green band represents the statistical uncertainties of the background yield and its shape. The right panel of Figure 5.34 shows the ratio of DY signal to the QCD background as a function of the virtual photon mass.

Finally it should be noted that only the QCD backgrounds are considered in the DY

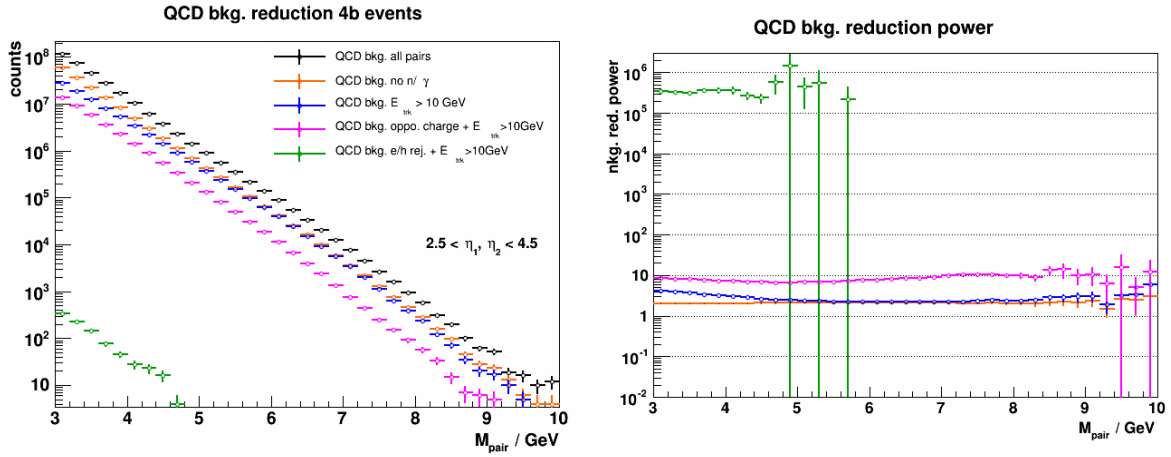

Figure 5.33: Reduction of the QCD background by applying cuts on track energy, charge sign and e/h discrimination. Neutral particles (γ/neutron) are removed by requiring the presence of a matched track in the FTS. Left: counts of background pairs. Right: background reduction power.

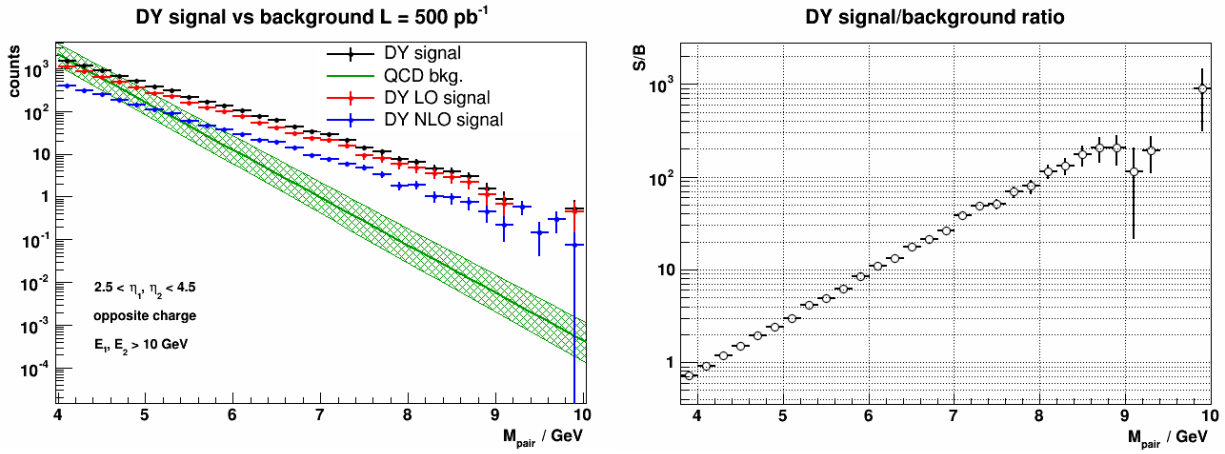

Figure 5.34: Left: DY signal and background yield *vs* virtual photon mass from 500 pb^{-1} $\sqrt{s}$ = 200 GeV proton proton collisions. Right: DY signal to background ratio *vs* virtual photon mass.

signal and background studies presented in this section. Additional background from photon conversions on detector materials are expected as well. Rough estimate indicates that these additional backgrounds are of the same order as the QCD background if care is taken to minimize the materials in the fiducial acceptance of the forward detectors. Thus the DY measurement for proton-nucleus collisions at 200 GeV with the STAR forward instrumentation upgrade is very promising and will be pursued vigorously.

CHAPTER 6

Summary and Outlook

Transverse single spin asymmetries (TSSA) of particle production at large x_F have been observed in various processes and center-of-mass energies from semi-inclusive deep inelastic scattering (SIDIS) to polarized proton-proton collisions. In order to understand its physical origins and connections to the transverse spin structure of the proton it is necessary to map out the behaviors of TSSA over a wide range of kinematics. For example the current SIDIS data set covers the high Q^2 but low p_T region where the Transverse Momentum Dependent factorization framework is believed to be valid. In order to involve color charges in the initial state and explore high p_T regions one needs to measure transverse single spin asymmetries in polarized proton proton collisions. The particle production mechanism in hadronic collisions is richer and more complicated than that in lepton scatterings so the measurements need to done for a broad range of processes. For example the Sivers functions extracted from Drell-Yan production in pp collisions can be compared with those from SIDIS experiments to test the fundamental property of modified universality predicted by QCD calculations. The p_T dependence of inclusive hadron productions in pp collisions can be used constrain initial-/final-state twist-3 models. In addition to following the guidance from theoretical developments, it is also of great interest for experimentalists to explore new phenomena which could potentially motivate fresh perspectives.

To that end we have measured the transverse single spin asymmetries of inclusive π^0 production in polarized proton-proton collisions at large x_F in $\sqrt{s} = 500$ GeV up to high p_T. The measurement was made with the Forward Meson Spectrometer (FMS) from the STAR experiment and can be compared to twist-3 predictions. There have been recent theoretical developments in the initial-state twist-3 calculations [74] as well as in the twist-3

fragmentation contributions [36] to the π^0 transverse single spin asymmetries in proton-proton collisions. For example Figure 6.1 shows a comparison between the combined twist-3 distribution and fragmentation contributions to the π^0 TSSA and the 2011 STAR data on isolated π^0 A_N [36]. Note that the STAR results shown in [36] and Figure 6.1 was analyzed with the same dataset as was used in this thesis, however the A_N was calculated only for isolated π^0 in order to skip the background subtraction procedure and speed up the process. The TSSA results presented in this thesis analysis is calculated with inclusive π^0 which makes it more suitable to be compared with the theory prediction shown in Figure 6.1, since no isolation criteria was considered in the theory calculations. Figure 6.2 shows the p_T dependence of the inclusive π^0 A_N compared to the same theory predictions.

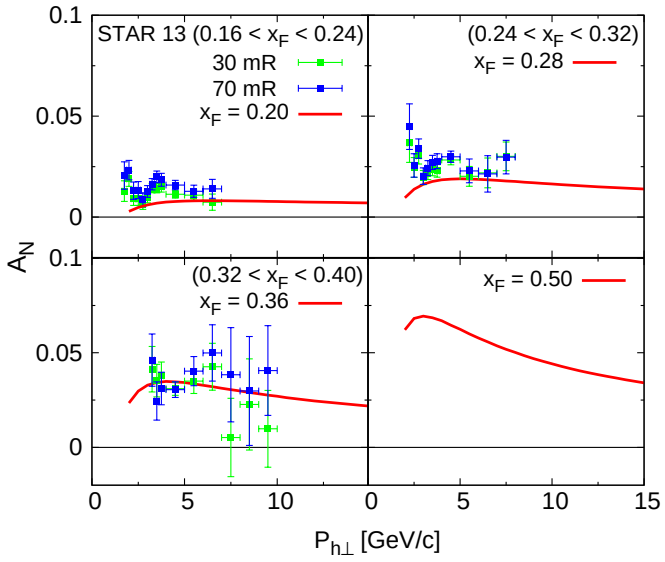

Figure 6.1: Combined twist-3 initial-/final-state contributions [36] compared with STAR data on isolated π^0 A_N.

Furthermore the dependence of the π^0 single spin asymmetries on event structure has also been studied. We found that the π^0 acquires large asymmetries when it is isolated from the rest of the event activities, and the asymmetries become much smaller when the π^0 is accompanied by other products from the collision. The radical behavior of the event topology dependence of π^0 A_N cannot be readily explained by the simple z-dependence of the

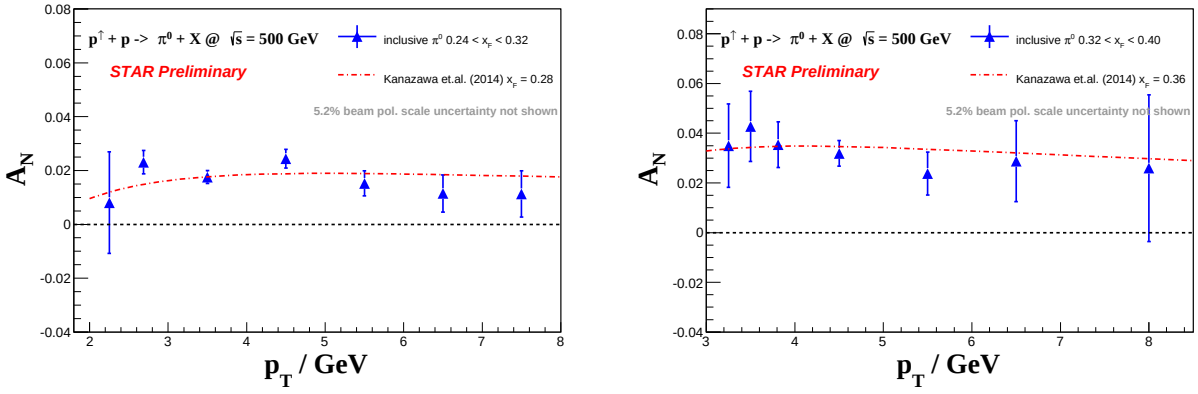

Figure 6.2: p_T dependence of inclusive π^0 A_N *vs* twist-3 predictions [36].

asymmetry as a result of the polarized fragmentation function. Further studies will continue in this direction with new data taken by upgraded detectors and trigger logics.

To expand the physics program beyond what has been covered by a single electromagnetic calorimeter, the FMS, the STAR collaboration has initiated an R&D project for a full instrumentation upgrade in the forward rapidity region, including a new compact electromagnetic calorimeter followed by an hadronic calorimeter and a forward tracking system. The forward upgrade program will open new opportunities to investigate the transverse and longitudinal spin asymmetries as well as low-x phenomena in proton and heavy nucleus. It also prepares STAR for possible transition to a multi-purpose detector system in the era of an Electron-Ion Collider. Much of the detector and physics simulation studies are performed in this thesis, e.g. capabilities for forward jet reconstruction, hadron-jet correlation measurements, prompt photon and Drell-Yan detection.

References

[1] D. J. Gross and F. Wilczek, "Ultraviolet Behavior of Non-Abelian Gauge Theories," *Phys. Rev. Lett.*, vol. 30, pp. 1343–1346, Jun 1973.

[2] F. Wilczek, "Asymptotic freedom: From paradox to paradigm," *Proceedings of the National Academy of Sciences of the United States of America*, vol. 102, no. 24, pp. 8403–8413, 2005.

[3] J. Currie, A.-D. Ridder, E. Glover, and J. Pires, "NNLO QCD corrections to jet production at hadron colliders from gluon scattering," *Journal of High Energy Physics*, vol. 2014, no. 1, 2014.

[4] A. Abulencia *et al.*, "Measurement of the inclusive jet cross section using the k_{t} algorithm in $p\overline{p}$ collisions at $\sqrt{s} = 1.96$ TeV with the CDF II detector," *Phys. Rev. D*, vol. 75, p. 092006, May 2007.

[5] B. I. Abelev *et al.*, "Longitudinal Double-Spin Asymmetry and Cross Section for Inclusive Jet Production in Polarized Proton Collisions at $\sqrt{s} = 200$ GeV," *Phys. Rev. Lett.*, vol. 97, p. 252001, Dec 2006.

[6] M. Gell-Mann, "A schematic model of baryons and mesons," *Physics Letters*, vol. 8, pp. 214–215, Feb. 1964.

[7] Y. Ne'eman, "Derivation of strong interactions from a gauge invariance," *Nuclear Physics*, vol. 26, no. 2, pp. 222 – 229, 1961.

[8] G. Zweig, "An SU(3) Model for Strong Interaction Symmetry and its Breaking," *CERN Report No.8419/TH.412.*, Jan. 1964.

[9] V. Barone and P. G. Ratcliffe, *Transverse Spin Physics*. World Scientific, 2003.

[10] M. Breidenbach, J. I. Friedman, H. W. Kendall, E. D. Bloom, D. H. Coward, H. DeStaebler, J. Drees, L. W. Mo, and R. E. Taylor, "Observed Behavior of Highly Inelastic Electron-Proton Scattering," *Phys. Rev. Lett.*, vol. 23, pp. 935–939, Oct 1969.

[11] S. Chekanov *et al.*, "ZEUS next-to-leading-order QCD analysis of data on deep inelastic scattering," *Phys. Rev. D*, vol. 67, p. 012007, Jan 2003.

[12] A. Accardi *et al.*, "Electron Ion Collider: The Next QCD Frontier-Understanding the glue that binds us all," *arXiv:hep-ph/1212.1701*, 2012.

[13] R. Jaffe and A. Manohar, "The g1 problem: Deep inelastic electron scattering and the spin of the proton," *Nuclear Physics B*, vol. 337, no. 3, pp. 509 – 546, 1990.

[14] X. Ji, "Gauge-Invariant Decomposition of Nucleon Spin," *Phys. Rev. Lett.*, vol. 78, pp. 610–613, Jan 1997.

[15] R. L. Jaffe, "The spin structure of the nucleon: Theoretical overview," *AIP Conference Proceedings*, vol. 588, no. 1, pp. 54–74, 2001.

[16] J. Ashman *et al.*, "A measurement of the spin asymmetry and determination of the structure function g1 in deep inelastic muon-proton scattering," *Physics Letters B*, vol. 206, no. 2, pp. 364 – 370, 1988.

[17] D. Adams *et al.*, "Measurement of the spin-dependent structure function g1(x) of the proton," *Physics Letters B*, vol. 329, no. 2-3, pp. 399 – 406, 1994.

[18] L. Adamczyk *et al.*, "Precision Measurement of the Longitudinal Double-spin Asymmetry for Inclusive Jet Production in Polarized Proton Collisions at $\sqrt{s}$=200 GeV," *arXiv:hep-ex/1405.5134*, 2014.

[19] J. Roche, "The DVCS program in Hall A at JLab," *PoS*, vol. QNP2012, p. 036, 2012.

[20] N. Collaboration, "Unbiased determination of polarized parton distributions and their uncertainties," *Nuclear Physics B*, vol. 874, no. 1, pp. 36 – 84, 2013.

[21] L. Adamczyk *et al.*, "Measurement of Longitudinal Spin Asymmetries for Weak Boson Production in Polarized Proton-Proton Collisions at RHIC," *Phys. Rev. Lett.*, vol. 113, p. 072301, Aug 2014.

[22] X. L. F. the STAR Collaboration, "Recent results of gluon and sea quark polarization measurements in polarized proton-proton collisions at STAR," *Journal of Physics: Conference Series*, vol. 535, no. 1, p. 012003, 2014.

[23] R. D. Klem, J. E. Bowers, H. W. Courant, H. Kagan, M. L. Marshak, E. A. Peterson, K. Ruddick, W. H. Dragoset, and J. B. Roberts, "Measurement of Asymmetries of Inclusive Pion Production in Proton-Proton Interactions at 6 and 11.8 GeV/c," *Phys. Rev. Lett.*, vol. 36, pp. 929–931, Apr 1976.

[24] D. Adams *et al.*, "Comparison of spin asymmetries and cross sections in π^0 production by 200 GeV polarized antiprotons and protons," *Physics Letters B*, vol. 261, no. 1-2, pp. 201 – 206, 1991.

[25] X. Ji, J.-W. Qiu, W. Vogelsang, and F. Yuan, "Unified Picture for Single Transverse-Spin Asymmetries in Hard-Scattering Processes," *Phys. Rev. Lett.*, vol. 97, p. 082002, Aug 2006.

[26] X. Ji, J.-P. Ma, and F. Yuan, "QCD factorization for semi-inclusive deep-inelastic scattering at low transverse momentum," *Phys. Rev. D*, vol. 71, p. 034005, Feb 2005.

[27] X. Ji, J.-P. Ma, and F. Yuan, "QCD factorization for spin-dependent cross sections in DIS and DrellYan processes at low transverse momentum," *Physics Letters B*, vol. 597, no. 3-4, pp. 299 – 308, 2004.

[28] U. D'Alesio, F. Murgia, and C. Pisano, "Azimuthal asymmetries for hadron distributions inside a jet in hadronic collisions," *Phys. Rev. D*, vol. 83, p. 034021, Feb 2011.

[29] M. Burkardt and D. S. Hwang, "Sivers effect and generalized parton distributions in impact parameter space," *Phys. Rev. D*, vol. 69, p. 074032, Apr 2004.

[30] Z.-B. Kang, J.-W. Qiu, W. Vogelsang, and F. Yuan, "Observation concerning the process dependence of the Sivers functions," *Phys. Rev. D*, vol. 83, p. 094001, May 2011.

[31] J. C. Collins, "Leading-twist single-transverse-spin asymmetries: DrellYan and deep-inelastic scattering," *Physics Letters B*, vol. 536, no. 1-2, pp. 43 – 48, 2002.

[32] J. Collins, "Fragmentation of transversely polarized quarks probed in transverse momentum distributions," *Nuclear Physics B*, vol. 396, no. 1, pp. 161 – 182, 1993.

[33] J. Qiu and G. Sterman, "Single transverse spin asymmetries," *Phys. Rev. Lett.*, vol. 67, pp. 2264–2267, Oct 1991.

[34] C. Kouvaris, J.-W. Qiu, W. Vogelsang, and F. Yuan, "Single transverse-spin asymmetry in high transverse momentum pion production in *pp* collisions," *Phys. Rev. D*, vol. 74, p. 114013, Dec 2006.

[35] A. Efremov and O. Teryaev, "QCD asymmetry and polarized hadron structure function measurement," *Physics Letters B*, vol. 150, no. 5, pp. 383 – 386, 1985.

[36] K. Kanazawa, Y. Koike, A. Metz, and D. Pitonyak, "Towards an explanation of transverse single-spin asymmetries in proton-proton collisions: The role of fragmentation in collinear factorization," *Phys. Rev. D*, vol. 89, p. 111501, Jun 2014.

[37] J. Adams *et al.*, "Experimental and theoretical challenges in the search for the quark gluon plasma: The STAR Collaboration's critical assessment of the evidence from RHIC collisions," *Nucl.Phys.*, vol. A757, pp. 102–183, 2005.

[38] Y. Akiba *et al.*, "The Hot QCD White Paper: Exploring the Phases of QCD at RHIC and the LHC," *arXiv:nucl-ex/1502.02730*, 2015.

[39] A. Zelensky *et al.*, "Optically pumped polarized H- ion source for RHIC spin physics," *Rev.Sci.Instrum.*, vol. 73, pp. 888–891, 2002.

[40] A. Zelenski *et al.*, "The rhic polarized source upgrade," *Journal of Physics: Conference Series*, vol. 295, no. 1, p. 012147, 2011.

[41] E. Courant and H. Snyder, "Theory of the Alternating-Gradient Synchrotron," *Annals of Physics*, vol. 281, no. 1-2, pp. 360 – 408, 2000.

[42] Y. Derbenev and A. Kondratenko *Part. Accel*, vol. 8, p. 115, 1978.

[43] I. G. Alekseev *et al.*, "Measurements of single and double spin asymmetry in *pp* elastic scattering in the CNI region with a polarized atomic hydrogen gas jet target," *Phys. Rev. D*, vol. 79, p. 094014, May 2009.

[44] O. Jinnouchi *et al.*, "Measurement of the analyzing power of proton-carbon elastic scattering in the CNI region at RHIC," *arXiv:nucl-ex/0412053*, 2004.

[45] I. Nakagawa *et al.*, "RHIC polarimetry," *The European Physical Journal Special Topics*, vol. 162, no. 1, pp. 259–265, 2008.

[46] Z. Tang, "J/psi production at high pT at STAR," *Nucl.Phys.*, vol. A855, pp. 396–399, 2011.

[47] L. Adamczyk, "Recent Results in Polarized Proton-Proton Elastic Scattering at STAR," *arXiv:nucl-ex/13113401*, 2013.

[48] M. Anderson *et al.*, "The STAR time projection chamber: a unique tool for studying high multiplicity events at RHIC," *Nuclear Instruments and Methods in Physics Research Section A: Accelerators, Spectrometers, Detectors and Associated Equipment*, vol. 499, no. 2-3, pp. 659 – 678, 2003.

[49] M. Beddo *et al.*, "The STAR Barrel Electromagnetic Calorimeter," *Nuclear Instruments and Methods in Physics Research Section A: Accelerators, Spectrometers, Detectors and Associated Equipment*, vol. 499, no. 2-3, pp. 725 – 739, 2003.

[50] J. Bouchet, "Heavy Flavor Tracker (HFT): A new inner tracking device at STAR," *Nuclear Physics A*, vol. 830, no. 1-4, pp. 636c – 637c, 2009.

[51] S. Agostinelli *et al.*, "Geant4-a simulation toolkit," *Nuclear Instruments and Methods in Physics Research Section A: Accelerators, Spectrometers, Detectors and Associated Equipment*, vol. 506, no. 3, pp. 250 – 303, 2003.

[52] L. C. Bland *et al.*, "An Electromagnetic Shower Profile in the Lead-Glass Calorimeter in the Energy Range of 3-23 GeV," *Nuclear Experimental Technique*, vol. 51, no. 3, pp. 342–350, 2008.

[53] R. Wigmans, *Calorimetry: Energy measurements in particle physics*. Oxford University Press, 2000.

[54] G. Aad *et al.*, "Measurement of the Inelastic Proton-Proton Cross-Section at $\sqrt{s} = 7$ TeV with the ATLAS Detector," *Nature Commun.*, vol. 2, p. 463, 2011.

[55] F. S. Bieser *et al.*, "The STAR trigger," *Nuclear Instruments and Methods in Physics Research Section A: Accelerators, Spectrometers, Detectors and Associated Equipment*, vol. 499, no. 2-3, pp. 766 – 777, 2003.

[56] Y. Wang, *Measurement of Inclusive Forward Neutral Pion Production in 200 GeV Polarized Proton-Proton Collisions at RHIC*. PhD thesis, The University of Texas at Austin, 2004.

[57] L. K. Eun, *Transverse Single Spin Asymmetries and Cross-Sections for Forward π^0 and η Mesons at Large x_F in $\sqrt{s} = 200$ GeV $p^{\uparrow} + p$ Collisions at STAR*. PhD thesis, The Pennsylvania State University, 2011.

[58] S. Adhikari, "More on Shower Shapes: Fitting High Towers data to get the Shower Shape parameters." `https://drupal.star.bnl.gov/STAR/blog/adhikari/2011/jul/31/more-shower-shapes-fitting-high-towers-data-get-shower-shape-parameters`.

[59] T. Sjöstrand, S. Mrenna, and P. Skands, "Pythia 6.4 physics and manual," *Journal of High Energy Physics*, vol. 2006, no. 05, p. 026, 2006.

[60] R. Field, "PYTHIA Tune Set A." `http://www.phys.ufl.edu/~rfield/cdf/tunes/py_tuneA.html`.

[61] L. Adamczyk *et al.*, "Transverse single-spin asymmetry and cross section for π^0 and η mesons at large Feynman x in $p^{\uparrow}+p$ collisions at $\sqrt{s}$=200GeV," *Phys. Rev. D*, vol. 86, p. 051101, Sep 2012.

[62] L. Eun, "Pythia setup for FCS simulation." `https://drupal.star.bnl.gov/STAR/blog/leun/2012/dec/18/fcs-simulation-setup-2`.

[63] M. Anselmino, M. Boglione, U. D'Alesio, S. Melis, F. Murgia, and A. Prokudin, "Simultaneous extraction of transversity and Collins functions from new semi-inclusive deep inelastic scattering and e^+e^- data," *Phys. Rev. D*, vol. 87, p. 094019, May 2013.

[64] M. Cacciari, G. P. Salam, and G. Soyez, "The anti-k_T jet clustering algorithm," *Journal of High Energy Physics*, vol. 2008, no. 04, p. 063, 2008.

[65] Drachenberg, J.L. and STAR Collaboration, "Transverse single-spin asymmetries from $p^{\uparrow}+p \to jet+X$ and $p^{\uparrow}+p \to jet+\pi^{\pm}+X$ at $\sqrt{s}=500\ GeV$ at RHIC," *EPJ Web of Conferences*, vol. 73, p. 02009, 2014.

[66] T. S. Collaboration, "Forward Upgrade Project." `https://drupal.star.bnl.gov/STAR/future/proposals/forward-upgrade-project`.

[67] D. Acosta *et al.*, "Electron, pion and multiparticle detection with a lead/scintillating-fiber calorimeter," *Nuclear Instruments and Methods in Physics Research Section A: Accelerators, Spectrometers, Detectors and Associated Equipment*, vol. 308, no. 3, pp. 481 – 508, 1991.

[68] R. Wigmans, "On the energy resolution of uranium and other hadron calorimeters," *Nuclear Instruments and Methods in Physics Research Section A: Accelerators, Spectrometers, Detectors and Associated Equipment*, vol. 259, no. 3, pp. 389 – 429, 1987.

[69] R. Klanner, "Test program for the ZEUS calorimeter," *Nuclear Instruments and Methods in Physics Research Section A: Accelerators, Spectrometers, Detectors and Associated Equipment*, vol. 265, no. 1-2, pp. 200 – 209, 1988.

[70] L. Gamberg and Z.-B. Kang, "Single transverse spin asymmetry of prompt photon production," *Physics Letters B*, vol. 718, no. 1, pp. 181 – 188, 2012.

[71] J. Jalilian-Marian and A. H. Rezaeian, "Prompt photon production and photon-hadron correlations at RHIC and the LHC from the color glass condensate," *Phys. Rev. D*, vol. 86, p. 034016, Aug 2012.

[72] R. Hamberg, W. van Neerven, and T. Matsuura, "A complete calculation of the order α_s^2 correction to the Drell-Yan K-factor," *Nuclear Physics B*, vol. 359, no. 2-3, pp. 343 – 405, 1991.

[73] J. Collins, D. E. Soper, and G. Sterman, "Transverse momentum distribution in drell-yan pair and w and z boson production," *Nuclear Physics B*, vol. 250, no. 1-4, pp. 199 – 224, 1985.

[74] K. Kanazawa and Y. Koike, "A phenomenological study of single transverse-spin asymmetry for inclusive light-hadron productions at RHIC," *Phys. Rev. D*, vol. 83, p. 114024, Jun 2011.